The Dissertation Committee for Xinyuan Dou Certifies that this is the approved version of the following dissertation:

Polymer based Nano- and Micro-photonic devices for Three-dimensional Optical Interconnects

Committee:

Ray T. Chen, Supervisor

Sanjay K. Banerjee

Jack C. Lee

Seth R. Bank

Chanro Park

Alan Xiaolong Wang

Polymer based Nano- and Micro-photonic devices for Three-dimensional Optical Interconnects

by

Xinyuan Dou, B.S., M.S.

Dissertation

Presented to the Faculty of the Graduate School of
The University of Texas at Austin
in Partial Fulfillment
of the Requirements
for the Degree of

Doctor of Philosophy

The University of Texas at Austin
December 2010

Dedicated to my family

Acknowledgements

I would like to thank my advisor, Dr. Ray T. Chen, for his continuous support and guidance in my doctoral study. Dr. Chen is a highly esteemed scholar with an affable personality. Dr. Chen's group-meetings are especially enjoyable. The group-meetings improve our organization and communication abilities. I would also like to thank the Microelectronics Research Center at The University of Texas at Austin for providing me with such an excellent research and development environment to conduct my research and pursue my graduate education. I also thank my committee members, Dr. Sanjay K. Banerjee, Dr. Jack C. Lee, Dr. Seth R. Bank, Dr. Chanro Park and Dr. Alan Xiaolong Wang for their serve on the committee and advices on my dissertation.

I appreciate the help from members of Optical Interconnect Group at University of Texas at Austin, particularly the former group students: Dr. Wei Jiang, Dr. Yihong Chen, Dr. Lanlan Gu, Dr. Li Wang, Dr. Xiaonan Chen, Mr. Jiaqi Chen. I also thank all the other current group members and the members at Omega Optics Inc.. Special thanks to Ms. Jackie L Srnensky, who is the assistant to Dr. Ray Chen.

Finally, I would like to express my gratitude to my family for love and support during my doctoral study.

Xinyuan Dou
University of Texas at Austin
Austin, TX

Polymer based Nano- and Micro-photonic devices for Three-dimensional Optical Interconnects

Publication No._____________

Xinyuan Dou, Ph.D

The University of Texas at Austin, 2010

Supervisor: Ray T. Chen

The demand for higher bandwidth and higher speed driven by semiconductor technology development draws a great deal of research efforts devoted to the development of high speed data communication. Challenges on electrical copper interconnects at high frequency make optical interconnect technologies become a promising alternative to conventional electrical interconnects at different levels. This doctoral dissertation describes polymer based nano- and micro-photonic devices for three-dimensional optical interconnects. Two areas are focused, (1) polymer based two-dimensional (2D) and three-dimensional (3D) photonic crystal fabrication and simulation for laser beam steering applications, (2) polymer based optical waveguide array and shared bus waveguide with embedded 45° micro-mirrors for board level optical interconnects.

A three-dimensional (3D) face-centered cubic (FCC) type polymer based photonic crystal using the polymer material SU-8 was simulated and successfully fabricated using a polygonal prism based holographic fabrication method. The theoretical study of polymer based photonic crystals was carried out for laser beam steering, which is based on the superprism effect. Horizontally stacked two-dimensional (2D) photonic crystal was fabricated by a double exposure holographic interference method. The k-vector superprism effect, the principle for beam steering, was studied in detail through EFC (Equi-frequency Contour) analysis.

A polymer based optical waveguide array with embedded 45° micro-mirrors for board level optical interconnects was prepared using a Ni metal hard mold by a UV imprint technique. A nickel based metal mold with 45º tilted surfaces on both ends of the channel waveguide was prepared through the electroplating process. To obtain a precise 45º tilted angle, a 50µm thick SU-8 layer was exposed under de-ionized water. High speed optical testing (10Gb/s) was carried out on the polymeric optical waveguide array with embedded 45º micro-mirrors on flexible substrate for out-of-plane optical interconnects. A polymer based 3-to-3 shared optical bus waveguide with opposite 45º micro-mirrors was designed and fabricated using the metallic hard mold method. The Ni metal hard mold was successfully prepared using the Ni electroplating method. This metallic hard mold provides a convenient way to fabricate the polymeric optical bus waveguide devices through the imprint technique.

Table of Contents

List of Tables

List of Figures

Chapter 1 *Introduction*

1.1 OVERVIEW OF PHOTONIC CRYSTALS

Photonic crystals, (also called photonic band-gap (PBG) materials or PhCs), are a novel class of artificial optical materials composed of periodic dielectric structures with different permittivity and feature sizes on the order of optical wavelengths[1-4]. These artificial structures are characterized by one-dimensional (1D), two-dimensional (2D) or three-dimensional (3D) periodic arrangements of dielectric materials which lead to the formation of an energy band structure of electromagnetic wave propagating in them. The schematic view of 1D, 2D and 3D photonic crystals are shown in Figure 1.1. Due to the dielectric micro-structures with periodicity of roughly half the wavelength of light, photonic crystal materials usually scatter photons similar to the scattering of electrons by the atom crystalline array within a semiconductor. Also photonic crystals have unusual optical properties and promise to provide revolutionary solutions to shrink the dimensions of photonic devices. Compared to electrons, photons have many advantages as carriers of information. They are much faster and able to convey large amounts of data with low power loss. Photonic crystals have the potential to steer light in the same way that electrons are manipulated and routed in semiconductor chips.

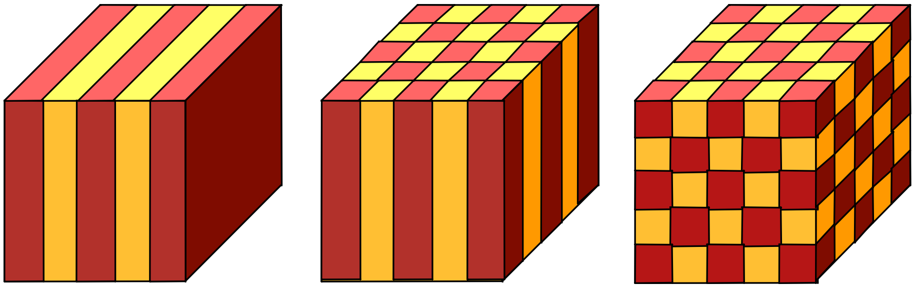

Figure 1.1: Schematic of 1-dimensional (1D), 2-dimensional (2D)and 3-dimensional (3D) photonic crystals [5]

Photonic crystals can create a photonic band gap which is analogous to the electronic band gap in semiconductors. This photonic band gap makes photonic crystals possess the property of preventing light from propagating in certain directions with specified energies. Depending on their energy, the photons are either allowed or non-allowed states of the lattice. In a photonic-crystal material, the allowed states supported by the periodic lattice are usually known as “Bloch modes,” whereas ranges of non-allowed states are designated as “photonic bandgaps.” In a broad generalization, a given wavelength of light incident shinning on the lattice is thus either transmitted through the lattice or reflected, respectively [6].

Applications for photonic crystals fall into two generic categories based on either the reflective or transmissive attributes of a photonic crystal. The first includes spectral filtering, micron-scale optical interconnects, and high-efficiency microcavity laser devices. All of these applications predominantly make use of the reflective properties of a photonic bandgap to either confine light within a microcavity or line-defect waveguide or to provide back-reflection over a certain stop band. For example, in a microcavity laser device, light is generated within the gain material, radiating in all directions simultaneously. For this category of application, it is desirable to ensure that the properties of the bandgap are as isotropic as possible, thus helping to reduce the linewidth of the laser emission and improve the spatial mode profile.

The second set of generic applications includes spatial beam steering, polarization control, and optical time delay. These require the transmission of light directly across the lattice, in which light must couple from the external environment (usually via an input waveguide) into guided Bloch modes that propagate within the PC. Because properties of guided modes in photonic crystals are described by dispersion relations, the greater the curvature, the stronger these effects become [7, 8], as shown in Figure 1.2.

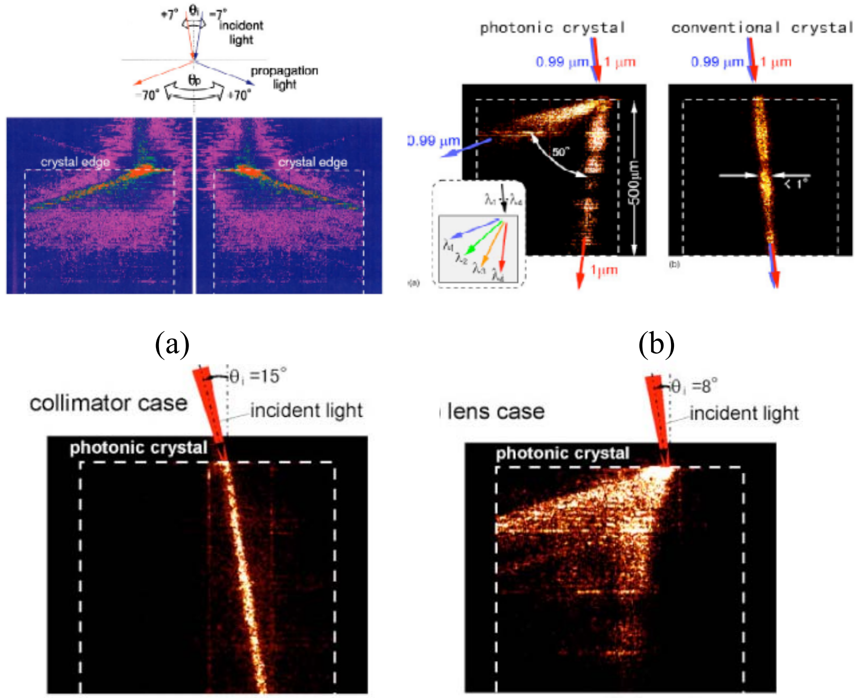

(a) (b)

(c) (d)

Figure 1.2: Hot topics observed in photonic crystals [9]. (a) Superprism phenomena with wavelength sensitivity. (b)Superprism phenomena with angular sensitivity. (c) Supercollimator phenomena. (d) Superlens phenomena

1.2 SOLID-STATE THEORETICAL DESCRIPTION OF PHOTONIC CRYSTALS

In the photonic crystals, the light propagation obeys Maxwell's equations. Hence, we can calculate from the original Maxwell's equations to find the band structure of the photonic crystals. Although it is convenient to use some commercial software to calculate the band structure, such as R-Soft, it is still very necessary to understand the basic concept in the calculations. From any electromagnetic textbook, we can find the original Maxwell's equations: [10,11]

$$\begin{aligned}
&\nabla \bullet \vec{\mathrm{H}}(\vec{\mathrm{r}},\mathrm{t}) = 0 \\
&\nabla \times \vec{\mathrm{H}}(\vec{\mathrm{r}},\mathrm{t}) - \varepsilon(\vec{\mathrm{r}})\frac{\partial(\varepsilon_0\vec{\mathrm{E}}(\vec{\mathrm{r}},\mathrm{t}))}{\partial \mathrm{t}} = 0 \\
&\nabla \bullet \varepsilon\vec{\mathrm{E}}(\vec{\mathrm{r}},\mathrm{t}) = 0 \\
&\nabla \times \vec{\mathrm{E}}(\vec{\mathrm{r}},\mathrm{t}) - \frac{\partial(\mu_0\vec{\mathrm{H}}(\vec{\mathrm{r}},\mathrm{t}))}{\partial \mathrm{t}} = 0
\end{aligned} \tag{1.1}$$

Where *E* and *H* are the electrical and magnetic fields, ε is the permittivity, *μ* is the permeability, *t* is the time, and *r* is the displacement from the origin.

The time harmonic mode at the steady state is

$$\begin{aligned}
\vec{H}(\vec{r},t) &= \vec{H}(\vec{r})e^{-i\omega t} \\
\vec{E}(\vec{r},t) &= \vec{E}(\vec{r})e^{-i\omega t}
\end{aligned} \tag{1.2}$$

By substituting Eq. 1.2 to Eq. 1.1, we can obtain Maxwell's equations for steady state

$$\begin{aligned}
\nabla \times \vec{H}(\vec{r}) + i\omega(\varepsilon(\vec{r})\varepsilon_0\vec{E}(\vec{r})) &= 0 \\
\nabla \times \vec{E}(\vec{r}) - i\omega(\mu_0\vec{H}(\vec{r})) &= 0
\end{aligned} \tag{1.3}$$

By expressing the equation in magnetic field H only, we can get the full-vector wave equation [39,40]

$$\vec{\nabla} \times (\frac{1}{\varepsilon}\vec{\nabla} \times \vec{H}) = -\frac{\omega^2}{c^2}\vec{H} \tag{1.4}$$

Thus, the Maxwell's equations for steady state can be expressed in terms of an eigenvalue equation, with the eigenvalue $(\omega/c)^2$.

Photonic crystals correspond to a periodic function

$$\varepsilon(\vec{r}) = \varepsilon(\vec{r} + \vec{a}) \tag{1.5}$$

for some primitive lattice vector *a*. By employing Bloch's theorem

$$\vec{\mathrm{H}}(\vec{\mathrm{r}}) = \exp(\mathrm{i}\vec{\mathrm{k}} \cdot \vec{\mathrm{r}})\vec{\mathrm{H}}_{\mathrm{n},\vec{\mathrm{k}}}(\vec{\mathrm{r}}) \tag{1.6}$$

$$\vec{H}_{n,\vec{k}}(\vec{r} + \vec{R}) = \vec{H}_{n,\vec{k}}(\vec{r})$$

where $\vec{H}_{n,\vec{k}}$ is the periodic envelope function, to Eq. 1.4, we can obtain a full-vector wave equation of Bloch's envelope function $\vec{H}_{n,\vec{k}}$ [10,11]

$$(\vec{\nabla}+i\vec{k})\times\frac{1}{\varepsilon}(\vec{\nabla}+i\vec{k})\times\vec{H}_{n,\vec{k}}=-\frac{\omega_n(\vec{k})^2}{c^2}\vec{H}_{n,\vec{k}} \quad (1.7)$$

The eigensolutions are periodic functions of the Bloch wavevector *k*. The solution at *k* is the same as the solution at *k+G*, where *G* is a *primitive reciprocal lattice vector* defined by $R_i \cdot G_j = 2\pi\delta_{i,j}$. Owing to this periodicity, we only need to calculate the eigensolutions for *k* within the primitive cell of this reciprocal lattice. Generally we choose the first Brillouin zone, an inequivalent wavevector closest to *k=0*. The master eigenvalue equation of electromagnetic waves in Photonic crystals is analogous to the *Schrödinger* equation of an electron in a periodic potential. The periodic dielectric material ε is analogous to the periodic potential *V*. The magnetic field H is analogous to the wave function ψ. The photonic bandgap $\Delta\omega_g$ is analogous to the electronic bandgap E_g. Also, both have the concept of a Brillouin zone. Thus some simulation methods in solid state physics or semiconductor physics such as plane wave expansion method can be directly implemented into photonic crystals with some modifications.

1.3 PREPARATION OF PHOTONIC CRYSTALS

In addition to the theoretical study on the photonic crystals, much research literature has reported on the preparation and characterization of photonic crystals, including 2D and 3D photonic crystals. From the beginning of research on photonic crystals, 2D photonic crystals are more investigated than 3D because 3D photonic crystals are more difficult to fabricate than 2D photonic crystals. Also, the calculation of 2D photonic crystals is less time consuming and many interesting phenomena can be studied. For 2D photonic crystals, H. Masuda reported using a highly ordered anodic porous alumina method. Anodic porous alumina is formed by anodization of Al in acidic solutions, consisting of an ordered triangular array of holes with a high aspect ratio in the alumina matrix [12]. Modern e-beam lithography and dry etching is also another very popular fabrication method, only with the limit of possible aspect ratios up to 10-30. Ideal 2D photonic crystals consist of periodic arrays of infinitely long pores or rods.

Most significant research work based on photonic crystals concerns 2D photonic crystals. Fabrication of 3D photonic crystals is also investigated and many methods are proposed in recent years. One approach is to modulate the pore diameter with the pore depth [13]. The pore diameter of the macropores can be controlled during the fabrication process by intensity of back side illumination of wafer. Strong illumination leads to high etching currents and wide pores, while the opposite is valid for low illumination. Among those fabrication methods, layer-by-layer stacking using soft lithography or nanoimprint, microassembly of planar semiconductor layers, and multiphoton absorption has been investigated to create certain microstructures.

Campbell and coworkers successfully demonstrated the fabrication of a 3D photonic crystal utilizing the holographic interference method [14]. Since then, holographic lithography has gained more attention in fabricating of 3D polymer photonic crystals. By controlling the propagation directions, phases and polarizations of the multiple laser beams, one can generate a desired 3D laser interference pattern to expose photo-sensitive materials such as photoresist and render the exposed area soluble or insoluble depending on the material type in use. This process allows flexible design and a control of the unit cell geometry and therefore of the desired optical properties. It has been proven theoretically that all fourteen Bravais lattice structures can be achieved using the holographic method. [15]

1.4 OVERVIEW OF EMBEDDED BOARD LEVEL OPTICAL INTERCONNECTS

In reality, optical communication dominates over electronics in the backbone, metro, and even some local communication networks. Electrical interconnects still dominate in short distance fields, such as chip to chip, board to board, and computer to computer. Miller and Oazkatas have shown that the maximum number of bits per second that can be carried by an electrical interconnection is [16]:

$$B \approx B_0 A / L^2,$$

in which A is the cross-sectional area of the conductor, L is the interconnection length, and B_0 is dependent on geometry with a value of about 10^{16} bit/s for wires on a chip. The ratio of $\sqrt{A} / L$ determines the bit rate which can be supported by a wire. For instance, beyond 10GHz, copper interconnects on PCB made of FR4 material become bandwidth limited due to losses such as the skin effect in the conductors and the dielectric loss from the substrate material. The optical waveguides are not subject to the resistive loss physics that gives rise to the equation above [17].

There are two main categories of optical systems used in optical interconnects which were identified: the free-space category and the guided-wave category [18-21]. In free-space optical interconnects, the optical field travels through a physically unconfined region between the optical source and detector planes (Figure 1.3). The optical field propagation is only determined by the propagation characteristics of free space. The free space optical interconnects offer high density, high speed and powerful fanout capability. It is also intrinsically low in optical loss. The main challenges for implementing high-density, high-speed, free-space optical interconnects are the device packaging due to stringent alignment requirements and device reliability in a harsh environment. There are some other disadvantages of the free space interconnects, for example, the system is vulnerable to external environments such as dust and vibration.

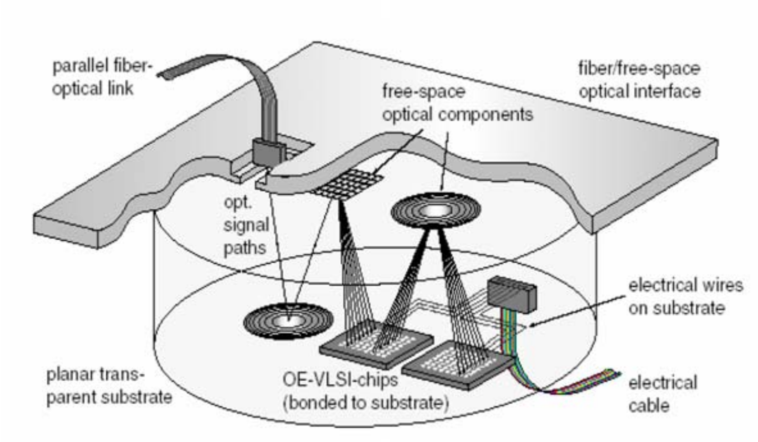

Figure 1.3: Schematic view of free space optical interconnect [22]

In guided-wave optical interconnection structures, waveguides or optical fibers are used to form the optical path. This provides ease of packaging, flexibility of route design, and system reliability. Optical fibers are also commercially available for telecommunications consisting of a low-loss light propagation medium with very good quality and reliability. Fibers are also widely used in long-range communications, such as in fiber-to-the-home (FTTH). As far as the board level interconnection is concerned, this requires very accurate placing of the fiber onto the board and precise alignment with the other components, such as VCSELs and photodiodes (Figure 1.4). Furthermore, planarized and compact structures are desirable for system integration. Optical waveguides will be a better approach over fiber for these concerns. Ongoing research in material science is continuously developing new materials suitable for optical waveguide applications. Materials science research is intended to develop new materials with low propagation loss and ease of fabrication while reducing the manufacturing cost. Optical waveguides based on these low-loss materials as well as the desirable properties for board-level interconnects are being developed.

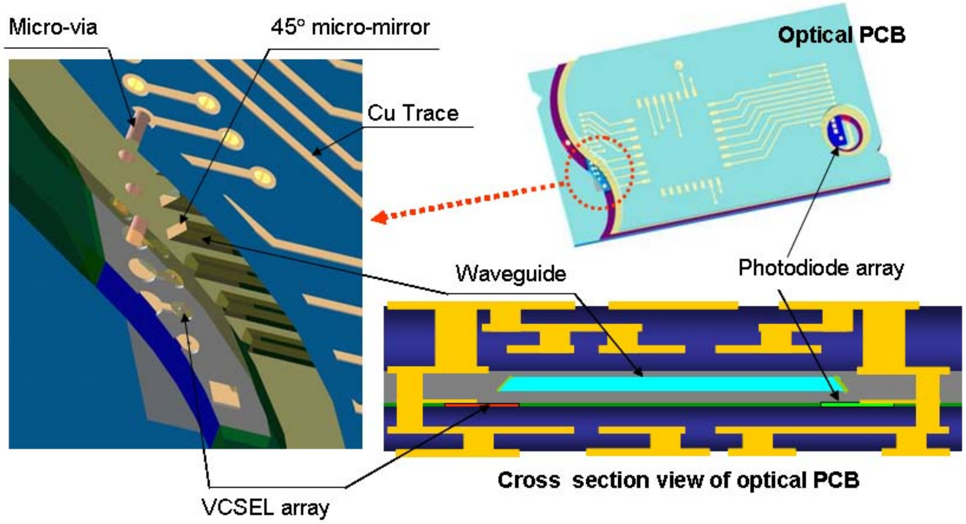

Figure 1.4: Fully Embedded Board Level Optical Interconnection [23]

1.5 OPTICAL BUS WAVEGUIDE FOR BOARD LEVEL OPTICAL INTERCONNECT

In electrical interconnects, the point-to-point topology replaced the shared-bus topology because of its superior bandwidth. However, wiring congestion is the adverse consequence of this transition, because in order to route all memory modules to the central switch, the boards in a high performance computing system currently tend to use more than 50 wiring layers, and more than 700 signal pins are required for one board edge connector, which needs as much as 100 pounds of insertion force to seat [24]. Optical bus architecture greatly mitigates wiring congestion, while still allowing multiple daughter boards to share a common data channel to transfer information at a high speed simultaneously [25-26]. There is no loading effect of optics analogous to driving capacitance in electronic circuit, which means the signal propagation speed is a constant value of 0.6c in polymer waveguides regardless of the presence of the receiver boards. For an electrical bus, an unloaded PC board trace has a typical signal propagation speed of 0.6c down to a fully loaded bus line signal speed of 0.2c. Higher speed as well as a much more stable signal round-trip time can be obtained by replacing the electrical bus with the proposed optical bus. Comparing with point to point interconnects, bus based interconnects represent the most complicated interconnect structure with a full interconnectivity and broadcasting nature [27-29]. Fiber based optical interconnects, which are intrinsically for point-to-point interconnection, fails to provide the desired optical bus architecture. Here we designed the optical bus based interconnected system with 3-to-3 nodes, which have the advantage of enhancing the bandwidth, increasing the reliability, providing package compatibility, and reducing fabrication cost.

1.6 DISSERTATION ORGANIZATION

My research topic is: Polymer based Nano- and Micro-photonic devices for Three-dimensional Optical Interconnects. We carried out comprehensive investigation on polymer based photonic crystals, polymer based point-to-point optical waveguide array, high speed testing on a waveguide array, and a polymer based shared bus waveguide for board level optical interconnect.

In Chapter 1, we investigated the basic concepts and principles of photonic crystals, the fabrication technique of photonic crystals, an overview of board level optical interconnect, point to point optical waveguides, and a shared optical bus waveguide for board level optical interconnects.

In Chapter 2, polymer based photonic crystals are discussed. Holographic fabrication of 2D and 3D photonic crystals on glass substrate, and V-groove substrate were developed successfully. Simulations of laser beam steering based on 2D square lattice photonic crystals were simulated using R-soft equi-frequency contour analysis and FDTD (finite difference time domain) simulations.

In Chapter 3, polymer based point-to-point waveguides with embedded 45° micro-mirrors for board level optical interconnect are successfully fabricated utilizing a Ni metal hard mold. The metal Ni hard molds are achieved by an electroplating method, which uses negative photopolymer SU-8 as a pre-electroplating mold. The 45° coupling surfaces within the SU-8 pre-mold are achieved by a tilted exposure under DI water method. Insertion losses as well as propagation losses are measured and calculated.

In Chapter 4, high speed (10Gb/s) optical testing at 850nm on the point-to-point waveguide with embedded 45° micro-mirrors are presented. The device performance under flat condition and different bending conditions is carefully measured. The degradations of quality factors (Q factor) and bit error rate (BER) of the waveguide are studied under different bending conditions.

In Chapter 5, the fabrication, and characterization results of a 3x3 shared bus waveguide are presented. An SU-8 based pre-electroplating mold is achieved by tilted exposure under DI-water. Ni plating is carried out on the SU-8 pre-mold, and the Ni metal mold is achieved after stripping the SU-8 layer. Shared bus waveguide devices are achieved by a UV imprint method. Performance of the bus waveguide was studied at 850nm.

In Chapter 6, the dissertation is summarized and recommendations for future work are given.

1.7 REFERENCES

[1] E.Yablonovitch, “Inhibited Spontaneous Emission in Solid-State Physics and Electronics”, Phys. Rev. Lett., 58, 2059 (1987).

[2] S. John, “Strong localization of photons in certain disordered dielectric superlattices”,

Phys. Rev. Lett. 58, 2486 (1987).

[3] K. M. Ho, C. T. Chan, and C. M. Soukoulis, “Existence of a photonic gap in periodic dielectric structures”, Phys. Rev. Lett. 65, 3152 (1990).

[4] C. T. Chan, K. M. Ho and C. M. Soukoulis, “Photonic band gaps in experimentally realizable periodic dielectric structures”, Europhys. Lett. 16, 563 (1991).

[5] S. G. Johnson, J. D. Joannopoulos, Photonic crystals: road from theory to practice, Kluwer Academic Publishers, (2002).

[6] L. Wang, “Polymer-based Micro- and Nano-imprint Structures for Manipulation of Laser Beam Propagation,” Dissertation, University of Texas at Austin, 2007.

[7] R. B. Wehrspohn, “Applications of silicon-based photonic crystals”, 2nd IEEE International Conference on Group IV Photonics, 39 (2005).

[8] H. Benisty, J. M. Lourtioz, A. Chelnokov, S. Combrie, X. Checoury, “Recent advances toward optical devices in semiconductor-based photonic crystals”, Proceedings of the IEEE, 94, 5, 997 (2006).

[9] H. Kosaka, T. Kawashima, A. Tomita, M. Notomi, T. Tamamura, T. Sato, and S. Kawakami, “Superprism phenomena in photonic crystals:”, Phys. Rev. B 58, 16, R10096 (1998).

[10] J. D. Joannopoulos, R.D. Meade, J.N. Winn, Photonic Crystals, Princeton University Press, (1995).

[11] S. G. Johnson, J. D. Joannopoulos, Photonic crystals: road from theory to practice, Kluwer Academic Publishers, (2002).

[12] H. Masuda, M. Ohya, H. Ahoh, M. Nakano, M, Nakano and T. Tamamura, Jpn, J. Appl. Phys. 38,L1403, (1999).

[13] J. Schilling, F.Muller, S.Matthias, R.B.Wehrspohn, U.Gosele, Appl.Phys.Lett. 78, 1180, (2001).

[14] M. Campbell, D. N. Sharp, M. T. Harrison, R. G. Denning and A. J. Turberfield, Nature (London) 404, 53 (2000).

[15] L. Z. Cai, X. L. Yang and Y. R. Wang. Opt. Lett. 27, 900, (2002).

[16] D. A. B. Miller, H. M. Ozaktas, "Limit to the bit-rate capacity of electrical interconnects from aspect ratio of system architecture," J. Parallel Distri Computing, 41, 42, (1997).

[17] T. N. Theis, "The future of interconnection technology," IBM J. Res.Develop. 44, 3, 379-389, (2000).

[18] M. Gruber, S. Sinzinger, and J. Jahns, "Optoelectronic multichip module based on planar-integrated free-space optics," Proc. SPIE, Optics in Computing2000, 4089, (2000).

[19] Elmar Griese, "Parallel Optical Interconnects for High Performance Printed Circuit Board," Proc. The 6th Int. Conf., 173, (1999).

[20] Yuzo Ishii, Shinji Koike, Yoshimitsu aria, and Yasuhiro Ando, "SMT-Compatible Optical I/O Chip Packaging for Chip-Level Optical Interconnects," Elec. Components and Technology Conf. 2001.

[21] R. T. Chen, L. Lin, C. Choi, Y. Liu, B. Bihari, L. Wu, S. Tang, R. Wickman, B. Picor, M. K. Hibbs-Brenner, J. Bristow, and Y. S. Liu, "Fully Embedded Board-level Guided-Wave Optoelectronic Interconnects", Proceddings of the IEEE, 88, 6, 780 (2000).

[22] M. Gruber, S. Sinzinger, and J. Jahns, "Optoelectronic multichip module based on planar-integrated free-space optics," Proc. SPIE, Optics in Computing, 4089, (2000).

[23] Alan Wang, "Highly Integrated Polymer Photonic Switching and Interconnects," Dissertation, University of Texas at Austin, 2007, Dissertation, (2006).

[24] D. Huang, T. Sze, A. Landin, R. Lytel, and H. L. Davidson, "Optical interconnects:

out of the box forever?" IEEE Journal of Selected Topics in Quantum Electronics 9, 614-624 (2003).

[25] X. Han, G. Kim, G. J. Lipovski, and R. T. Chen, "An optical centralized shared-bus architecture demonstrator for microprocessor-to-memory interconnects," IEEE J. Sel. Topics Quantum Electron. 9, 512–512 (2003).

[26] H. Bi, X. Han, X. Chen, W. iang, J. Choi, and R. T. Chen, "15Gbps Bit-Interleaved Optical Backplane Bus using Volume Photo-polymer Holograms," IEEE Photonics Technology Letters 18, 2165-2167 (2006).

[27] R. T. Chen, L. Lin, C. Choi, Y. Liu, B. Bihari, L. Wu, S. Tang, R. Wickman, B. Picor, M. K. Hibbs-brenner, J. Bristow, and Y. S. Liu, "Fully Embedded Board-Level Guided Wave Optoelectronic Interconnects," Proc. Of the IEEE 8, 780-794 (2000).

[28] R. T. Chen, "VME Optical Backplane Bus for High Performance Computer," Optoelectronics-Devices and Technologies 9, 81-94 (1994).

[29] A. X. Wang, W. Jiang, L. Wang and R. T. Chen, "Fully Embedded Board Level Optical Interconnects-From Waveguide Fabrication to Device Integration," IEEE J. Lightwave Technol. 26, 243-250 (2008).

Chapter 2 *Polymer-based photonic crystals fabrication and laser beam steering*

2.1 INTRODUCTION

Photonic crystals are artificial periodic dielectric structures to control light propagation. Since Yablonovitch and John firstly demonstrated the concept of photonic bandgap (PBG) materials in 1987 [1, 2], there has been a great deal of interest in this field. Due to their photonic bandgap and anomalous dispersion characteristics, they have great potentials for various novel optoelectronic devices. Photonic crystal based structures are anticipated to play a significant role in next generation photonic devices. The investigations of photonic crystals (PhC) at earlier times mainly focused on complete photonic bandgap and the propagation of light at the photonic bandgap edges. Such investigations calculate the band structures, the band gap sizes, and the resonant modes of photonic crystals. Another very important property of a PhC is that an unconventional dispersion exists in the photonic crystals. In 1998 Kosaka's group firstly demonstrated the superprism effect in a highly dispersive photonic structures [3,4]. These unusual properties provide an exciting possibility to steer light in photonic crystals [5].

A method has been demonstrated for controlling the propagation of light inside a photonic crystal that involves the manipulation of the anisotropy of the bands [6]. Due to this anisotropy, the propagation direction of light inside a photonic crystal can be extremely sensitive to parameters such as the wavelength or the incident angle of the light beam. This effect, known as the superprism phenomenon, is observed where anisotropy in the photonic band structure is strongest and behaves like negative refraction. Superprism effect is one of the unusual properties of photonic crystals, which could lead to a large change of propagation direction of the light beam within the photonic crystals due to a small change of the incident beam, such as its direction or the wavelength. A prism made up of a photonic crystal would have a dispersion capability 500 times stronger than a prism made of a conventional crystal [6]. Various theoretical predictions and experimental studies have been reported regarding anomalous angular deviation at high frequencies near the photonic band gap [7].

2.2 HOLOGRAPHIC FABRICATION OF 3D PHOTONIC CRYSTAL

Within all the available fabrication methods for 3D photonic crystals, we chose the holographic approach. Compared to other fabrication methods, such as e-beam lithography or the wood-pile layer by layer method, holographic approach has the advantage of large scale fabrication (mm to cm scale) capability by a single exposure in a very short time. It is based on multiple beam interference. When two or more optical waves are present simultaneously in the same region of space, the waves interfere and generate a periodic spatial modulation of light. Interference among any N (>=4) collimated, coherent laser beams produces an intensity grating with (N-1) dimensional periodicity if the difference between the wave vectors is non-coplanar as indicated in Figure 2.1(a). The intensity distribution of the interference field can be described by a Fourier superposition [8]:

$$I(\vec{r}) = \sum_{i=0}^{N-1} E_i^2 + 2\sum_{i=1}^{N-1} E_0 * E_i * \vec{e}_0 \bullet \vec{e}_i * \cos(\vec{K}_i \bullet \vec{r} + \theta_i) + 2\sum_{i>j=1}^{N-1} E_i * E_j * \vec{e}_i \bullet \vec{e}_j * \cos(\vec{K}_{ij} \bullet \vec{r} + \theta_{ij})$$

One way of producing four coherent laser beams is to use a novel prism as drawn in Figure 2.1(b). A collimated laser beam shines on the prism from the top. The top surface and the three side surfaces produce four coherent laser beams simultaneously. These four beams pass through the prism, exit from the bottom surface, and reach a region where they interfere with each other to produce a three-dimensional holographic pattern.

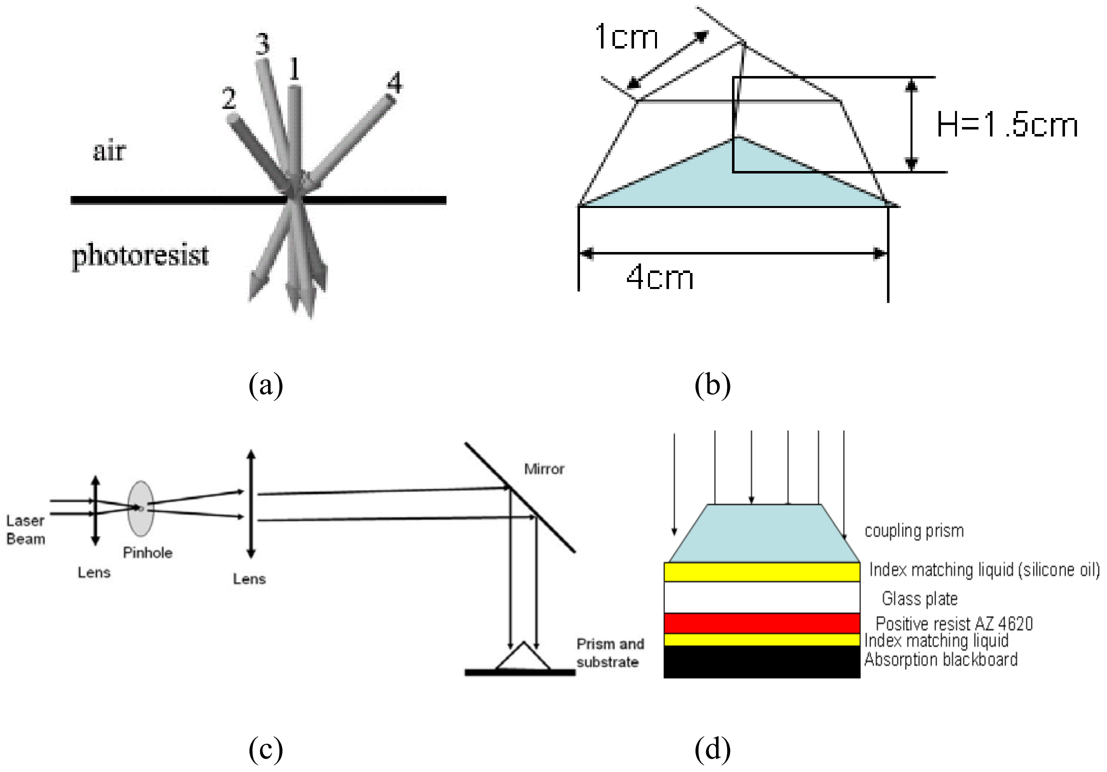

(a) (b)

(c) (d)

Figure 2.1: Holographic technique for fabrication of 3D photonic crystals. (a) Sketch of fabrication concept, (b) Prism used for holography in our approach, (c) A schematic of the holographic lithography setup, (d) Schematic of the experimental setup

The UV (325nm) laser beam coming from the He-Cd laser was expanded using a UV objective lens, as shown in Figure 2.1(c). The spatial filter afterward cleaned up the unwanted scattering in the optical path to ensure good beam quality. After the laser beam was collimated by a large lens, it hit normally on the special designed top-cut prism. Figure 2.1(d) gives the experimental setup for the exposure. Index matching liquid was used at the prism-sample interface and the sample-absorption marble blackboard interface. The prism was made from JGS1 material (n=1.482 @320nm) to achieve a larger than 95% UV transmission. The surfaces of the polygonal prism had been polished to make the transmission intensity as large as possible. The three sidewalls of the top-cut prism created three side beams by beam refraction. The center beam of this umbrella interference configuration was formed from the central part of the collimated laser beam going through the top and bottom surfaces of the prism. The four beams created by the prism overlapped at the bottom of the prism. By controlling the height of the prism one could control the depth of overlap to ensure the photoresist is within the overlap volume.

In our design shown in Figure 2.1(b) L_1=1cm, L_2=4cm and H=1.5cm. Therefore, we achieved a cutting angle of 60° for the prism. The resulting wave vectors were:

$$G_0 = \frac{2\pi}{\lambda}(0,0,-1), G_1 = \frac{2\pi}{\lambda}(-0.3314,-0.1914,-0.9239), G_2 = \frac{2\pi}{\lambda}(0.3314,\text{-}0.1914,\text{-}0.9239) \quad ,$$

$$G_3 = \frac{2\pi}{\lambda}(0,0.3827,-0.9239)$$

, where λ= 325nm in our case. With the polarization of the incident laser beam aligned with the x-axis in the system, the resulting polarizations for the four beams are:

$$e_0 = (1,0,0), e_1 = (0.9409,0.0055,-0.3387), e_2 = (0.9409,-0.0055,0.3387), e_3 = (1,0,0)$$

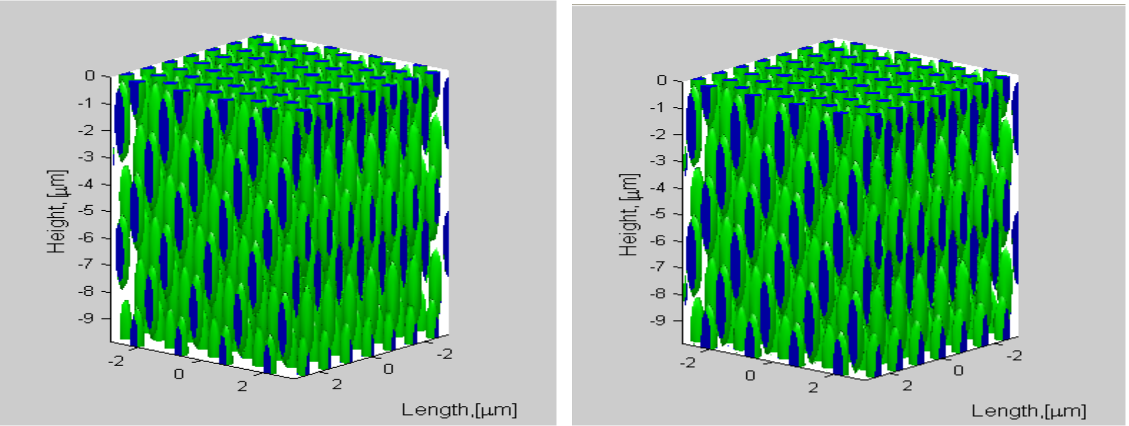

(a) (b)

Figure 2.2: (a) Simulation of intensity distribution in the photoresist without considering the absorption. (b) Simulation of intensity distribution in the photoresist considering the absorption

In order to model the fabrication of the 3D holographic lithography process more accurately we need to consider the absorption of the laser beam inside the photoresist. As such optical absorption during the exposure process caused the geometry of the fabricated photonic crystal to change with the depth. Figure 2.2 shows the computer simulations of FCC type photonic crystal obtained from four-beam interference with and without absorption using the k vectors obtained before and after an SU-8 absorption 10%/µm @ 330 nm.

Prisms were utilized to fabricate 3D photonic crystals using SU-8 and AZ 4620 or AZ P4620 photoresist. In the processing of SU-8 we deviated from the standard approach to avoid the structural damage resulting from the capillary drainage of the rinsing liquid during drying. Isopropanol, which is the standard SU-8 rinsing agent, has surface tension of γ=21.8mJ/m^2 and a contact angle of θ= 20°. It strongly wets the SU-8 surface. Water has a higher surface tension γ= 72mJ/m^2, but since SU-8 surface is hydrophobic with a contact angle of θ= 81°, the capillary force exerted by water is about half that of isopropanol [9], which is water soluble. Therefore, a final rinse in water was used for all fabricated samples and greatly improved their survival rate[8].

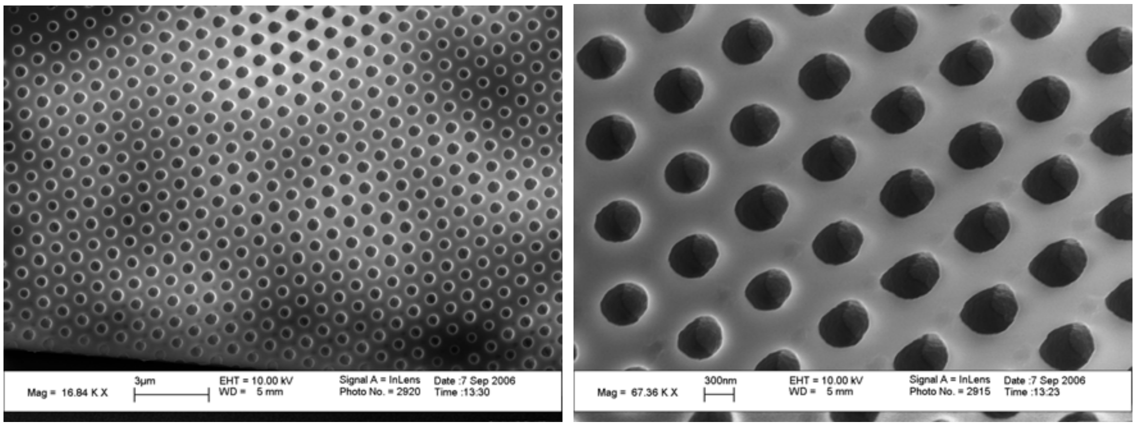

(a) (b)

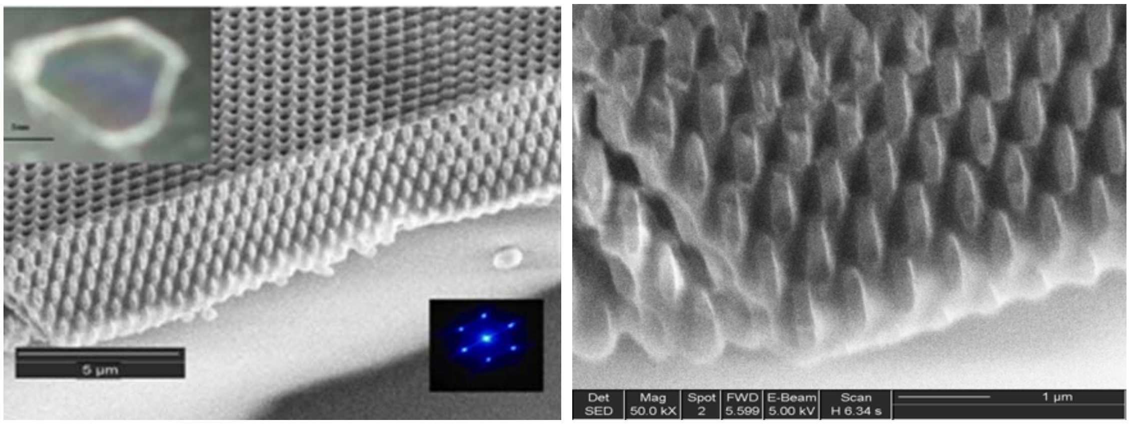

(c) (d)

Figure 2.3: SEM images of AZ 4620 based 3D polymeric photonic crystal structure. (a) Large area view (in-plane a=830nm), (b) close-up view, (c) Cleaved 3D photonic crystal on SU-8. The upper-left corner inset shows the cm^2 size photonic crystal. The lower-right corner inset shows the fcc-type (111) diffraction pattern. (d) close-up view of the 3D photonic crystal on SU-8

SEM images and the diffraction pattern of the fabricated 3D polymer photonic crystal structures are shown in Figure 2.3. The total area is decided by the size of the prism, and it is an equilateral triangle with an edge of 1cm. Figures 2.3(a) and (b) show the large area view and closer view of the top surface of the 3D FCC-type structure using SU-8, respectively. The side view of the cleaved SU-8 sample with 6 layers is shown in Figure2.3(c). A much closer view is shown in Figure 2.3(d). For the structures fabricated in the SU-8 resist under the SEM observation, the (111) in-plane and perpendicular lattice spacings were measured to be 0.61 and 2.02μm respectively. The simulation results showed (111) in-plane and perpendicular lattice spacing to be 0.63 and 2.10μm, which are slightly larger than the fabrication results. Such differences can be attributed to the size error of the prism and the shrinkage of the photoresist after the bake process. In addition, we used the 325nm laser normally incident on the (111) plane of the 3D photonic crystal to observe the diffraction patterns which are equivalent to x-ray diffraction normal to the (111) plane of an FCC single crystal. The diffraction result is shown in inset of Figure 2.3(c). The 1st order diffraction angle of the SU-8 3D structure was measured to be 35°. The period in the (111) plane calculated from the diffraction angle is in good agreement with the SEM measurements, and such a diffraction pattern further assures us the formation of good 3D periodic microstructures [8].

2.3 FABRICATION 3D PHOTONIC CRYSTALS IN V GROOVE SUBSTRATE

In addition to the fabrication of 3D photonic crystals on the flat substrate, experiments were also performed to make the photonic crystals inside V-groove structures. This is to create two unparallel interfaces. A series of experiments have been conducted to optimize the fabrication process. With the refined processing parameters, significant quality improvement of the polymer V-groove structures was achieved. The fabrication sequence, processing conditions and structure characterization for each step are presented as shown in Figure 2.4:

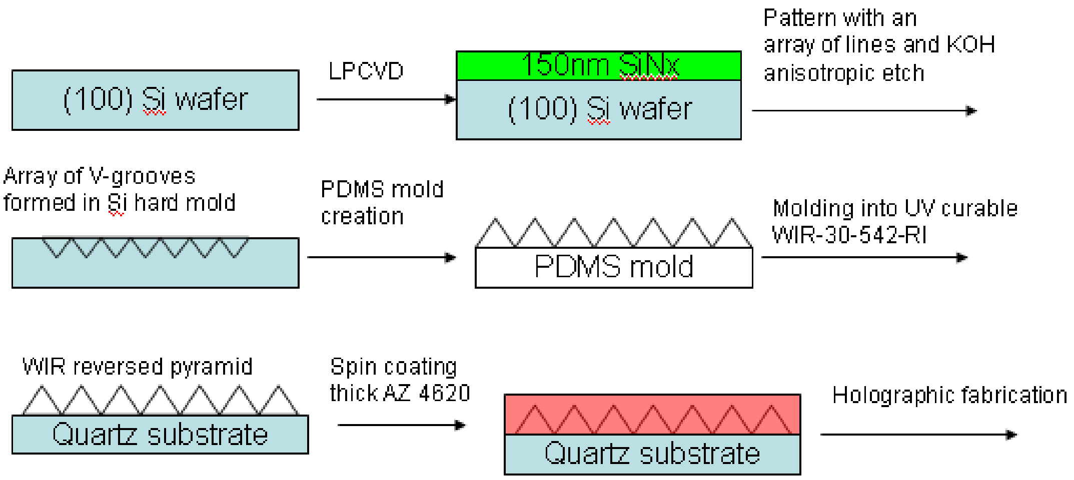

Figure 2.4: Fabrication process for the photonic crystals in V groove substrate

Step1: A 300nm thick SiO_2 layer was grown on a (100) silicon wafer using plasma enhanced chemical vapor deposition (PECVD) in N_2O+SiH_4 (with a ratio of 180:36) at 300°C for 20 minutes. An RF power of 30 W and a pressure of 30 mTorr were maintained in the growth chamber for the whole growth period.

Step2: An array of SiO_2 stripes were formed on the silicon substrate using photolithography and reactive ion etching (RIE), which served as a hard mask for the KOH wet etching process of the silicon substrate. The RIE process was optimized by varying a number of process parameters such as base pressure, gas pressures, RF power, DC power, etc. The refined process conditions in our RIE system are a base pressure of 30 mTorr, an RF power of 200 W, and a gas ratio of 20:4.2 between CHF_3 and O_2. The etching rate was measured as 22 nm/min.

Step3: The V-grooves in the silicon hard mold were formed by the self-limiting anisotropic KOH wet etching. The etchant used consisted of 100 g KOH, 200 ml DI water and 40 ml isopropanol. The 10 μm deep V-grooves were obtained through an initial etching for 15 minutes and a subsequent etching for 2 minutes 20 seconds with the removal of a SiO2 mask added in between. The silicon etching rate was around 1 μm /min under 80°C. Top- and side-view Scanning Electron Microcopy (SEM) images of the resulting silicon V-grooves are shown in Figure 2.5.

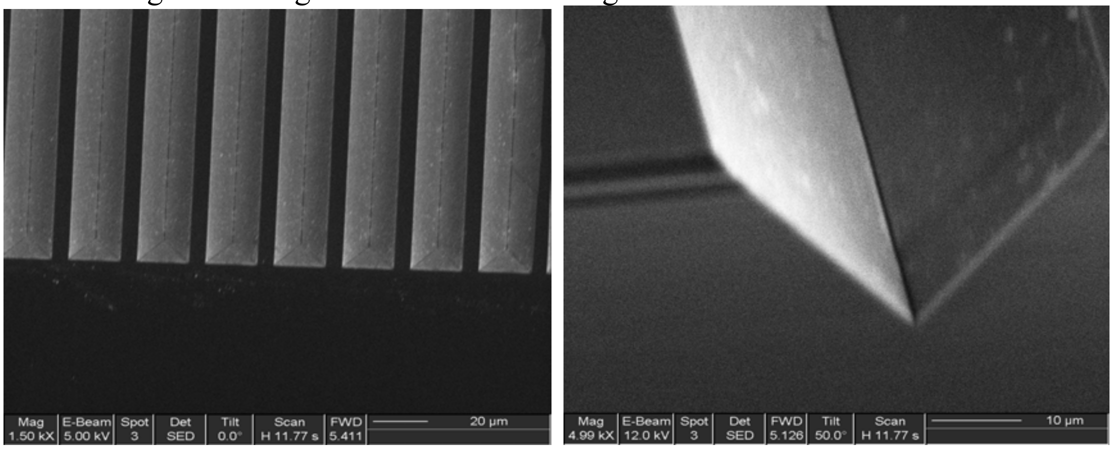

(a) (b)

Figure 2.5: Top-view(a) and 50°-view(b) SEM image of silicon V-grooves

Step 4: PDMS liquid polymer was cast onto the silicon substrate and filled up the V-grooves. After the PDMS thermally cross linked, it was peeled off from the silicon substrate and readily served as a negative soft mold.

Step 5: V-grooves on the UV curable WIR30-450 polymer were formed through a few molding procedures using previously obtained PDMS V-grooves as the soft mold. The microscope image of the WIR V-grooves on a quartz substrate is shown in Figure 2.6.

Step 6: Photoresist (AZ4620) was spun onto the WIR surface and filled up the V-grooves. The resulting grooved photoresist film was then ready for the subsequent holographic recordings to form 3-D photonic crystal structures. The top-view microscope image of the photoresist layer on top of the WIR V-grooves is shown in Figure 2.6.

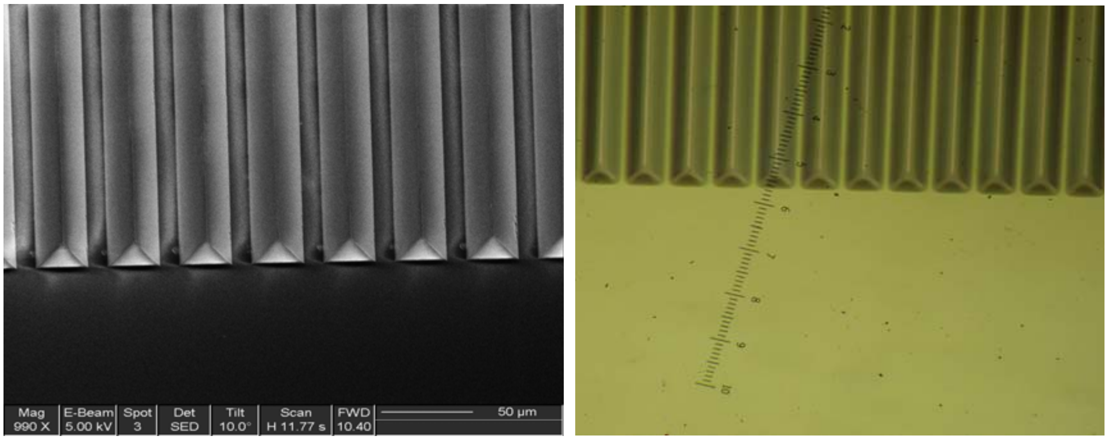

(a) (b)

Figure 2.6: (a)Top-view SEM of the PDMS soft mold. (b) Microscopic image of the WIR V-grooves on a quartz substrate

Filling photosensitive polymer (AZ4620) into pre-molded WIR polymer V-grooves is an essential step towards the success of developing arrayed holographic photonic crystals. A complete filling of WIR V-grooves is required to avoid the buildup of scattering noise during the holographic recording on the AZ4620 V-grooves. To obtain high-quality holographic photonic crystals, attention is necessary ensure acceptable flatness of the surface coating. This is not trivial considering the underlying WIR polymer V-grooves are more than 20 μm deep. The schematic of the stacked polymer structure AZ4620 V-grooves/WIR V-grooves is shown in Figure 2.7. Extensive experiments have been carried out to optimize the processing parameters of the filling procedure. The best result has been obtained by applying the following set of parameters:

(1) Spin-coat AZ4620 adhesive promoter at 4000 rpm for 20 seconds.

(2) Spin-coat AZ4620 photoresist at 2500 rpm for 60 seconds.

(3) Pre-bake on a hotplate under 100℃ for 90 seconds.

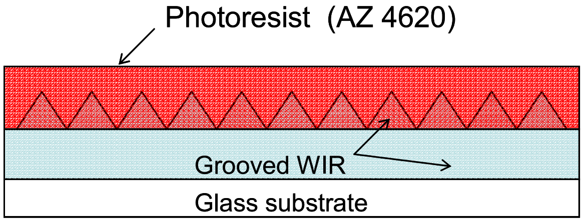

Figure 2.7: Schematic view of the polymer stacks for holographic recording

By controlling the multiple laser beams one can generate a desired 3D interference pattern to expose the photoresist and render the exposed area soluble or insoluble depending on the material type in use. Multiple beams can be obtained using a single refracting prism to split and combine the desired beams. With the use of a single optical element, a sophisticated anti-vibration system and alignment procedure are avoided.

AZ4620 or AZ P4620 is a positive photoresist, which means the exposed volume will be removed during development. With the absorption there is a decrease of dissolution volume fraction with the increased depth of the photoresist. Moreover, the effective development time for the upper resist is longer than the lower part. Combining these two effects, we would have overdeveloped and damaged the top structures before the desired 3D structure is formed at the lower part of the resist. Flip the recording glass plate prevents this, as shown in Figure 2.8. By letting the laser beams impinge on the glass substrate at first then enter the resist. In this way, the intensity distribution in the resist is reversed. Thus the lower dosage of the surface part would compensate the longer etch time and maintain the surface structures. Although a similar procedure have been employed for a single uniform layer of the AZ4620 resist in our earlier work, the double-layer configuration shown in Figure 2.8 presents a new challenge in that the top surface is not perfectly planarized during spin-coating. Initial recording experiments showed some bewildering results.

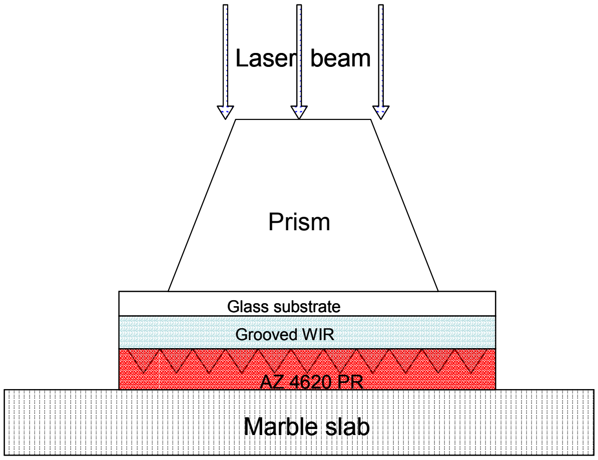

Figure 2.8: Schematic of recording on a flipped polymer stack

We have successfully fabricated high-quality 3-D photonic crystals in a single uniform layer of AZ4620 previously using this procedure. For the V-grooves substrate, we found that the top layer of the photoresist remained underexposed if using the similar exposure dose used to record the single layer structure with the same thickness. The top surface of the underexposed resist would not readily dissolve in developer even after increasing the developing time by a significant amount. The undeveloped top layer of the photoresist blocks the entrance of the developer into the well-exposed region that is underneath it. Thus, it prevents the formation of the photonic crystal structures inside the V-groove. The underexposure of the photoresist at the device surface is most likely caused by the light absorption in the grooved WIR region. We have also tried to increase the exposure dose to compensate this extra energy loss. A double-exposure procedure was explored to overcome this fabrication difficulty. We chose a moderate exposure dose to image the 3-D structure from the back of the device. Following that, we added a quick flood exposure from the top surface of the photoresist. This second exposure helps to remove the previously underexposed surface layer during development, which makes it possible for the developer to enter the underlying well-exposed region and develop the recorded pattern. The advantage of using this double-exposure procedure for fabricating arrayed photonic crystal structures has been confirmed experimentally. In Figure 2.9 are the some SEM images of the 3-D photonic crystals in a V-groove configuration.

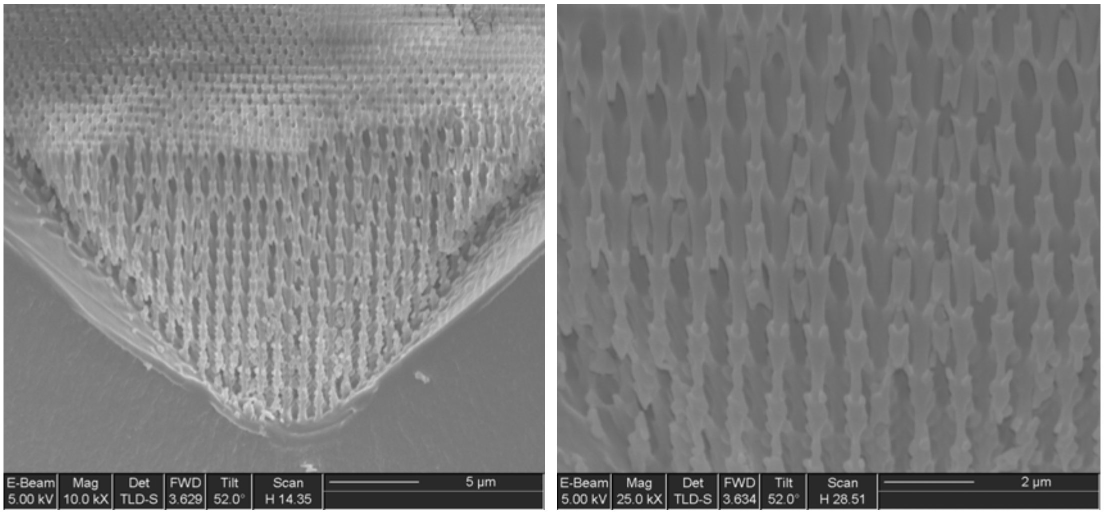

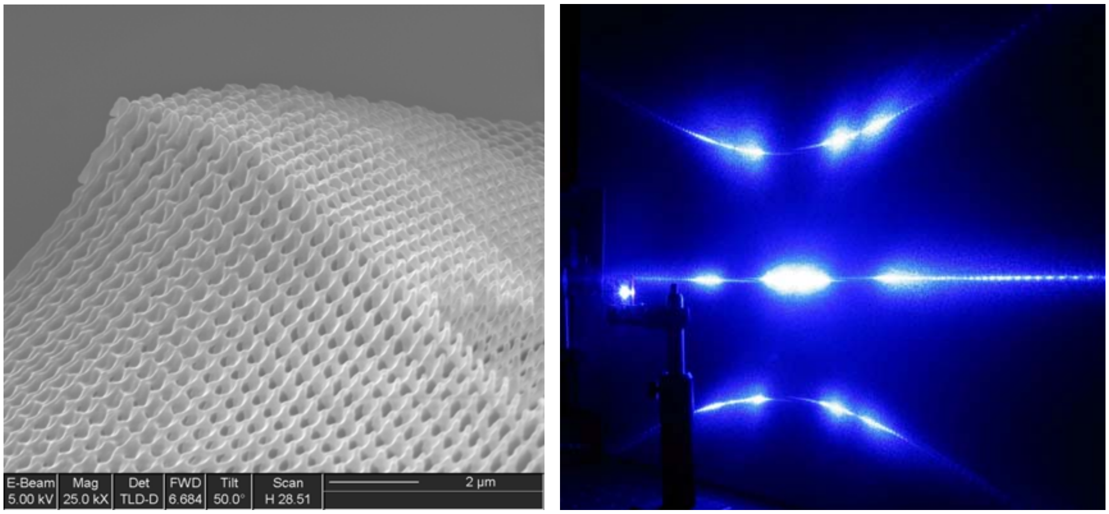

(a) (b)

(c) (d)

Figure 2.9: SEM images of 3-D photonic crystals showing: (a) low and (b) high magnification view of photonic crystal structures inside a V groove, and (c) one of the nature cleavage surfaces of the 3-D photonic crystals. (d) Laser diffraction pattern at 442nm

2.4 SUPERPRISM EFFECT SIMULATION OF 2D SQUARE LATTICE PHOTONIC CRYSTAL

When parallel beams are injected from one medium of refractive index n_1, to a dielectric medium of refractive index n_2, the relation between the incident angle and the propagating angle are described by Snell's law as [10] $n_1 \sin\theta_1 = n_2 \sin\theta_2$. At the interface of the two mediums, Snell's law is presented by a wave number conservation law of light waves, shown in Figure 2.10.

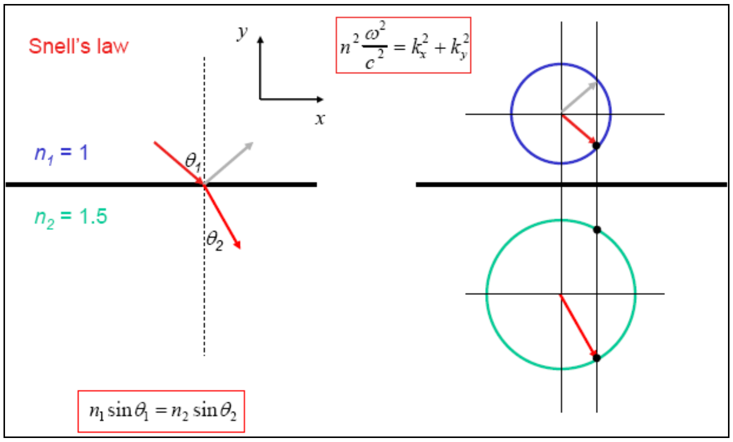

Figure 2.10: Beam incidence from medium 1 to medium 2 with ordinary dielectrics

In photonic crystals, the light propagation characteristics are completely different from normal dielectrics, such as air and water. Due to this difference, Snell's law becomes invalid. Photon propagation in photonic crystals is analogous to electron propagation in semiconductor materials. The photonic band structure determines the nature of photons in a photonic crystal. In the case of photonic crystals, this could be called dispersion surface engineering or photonic band engineering, whereby materials are artificially fabricated with the required optical performance inherently present and with the ability to manipulate photons as required.

Dispersion surfaces are equi-frequency contours along which the energy of the photon is conserved. The gradient direction of the dispersion surface is the direction of group velocity, which is the direction of propagation in a material. This relation is written as follows [10],

$$\mathrm{v}_g = \nabla_k \omega(k), \qquad (3.2)$$

where v_g is group velocity, ω is frequency and k is wavevector. Another condition is momentum conservation in the direction parallel to the incident surface. These two conservation conditions define the wavevector in a crystal, and the direction normal to the dispersion surface at the wavevector point gives the direction of propagation.

In the experiment, we found it was difficult to observe the superprism effect in the 3D photonic crystals because is that 3D PCs can have a large superprism effect inside that is also the s-vector superprism effect (group velocity). However, after coming out of PC, the superprism effect is limited due to the k-vector superprism effect principle. The s-vector superprism effect took place at the first interface only. The beam steering was tested in free space, which is outside of the photonic crystal or after at least two interfaces. After passing the second interface, based on the simulations, we found the 2D square lattice photonic crystals can have much larger beam steering angles compared to 3D photonic crystals. In order to obtain confirmation of the beam steering effect, we carried out the exploration on polymer based 2D photonic crystals.

Here we will consider a superprism configuration where the input and output surfaces are perpendicular to each other. Here we give a detailed theoretical study of this effect through EFC (Equi-frequency Contour) analysis for the polymer based photonic crystals. The layout of the square lattice photonic crystals with an area of 200 a*200a is shown in Figure 2.11, where *a* is the lattice constant of the PC structures. In our simulation, the input beam wavelength λ is 1.55um, the lattice constant *a* is 1.085um(a/λ=0.7), and the material index n is assumed 1.6, which corresponds to the index of SU-8 polymer at the wavelength of interest. The launch field is a Gaussian beam with a width of 120*a. The red rectangles (index=1.0) are used to make the two interface rods into a semi-circle. A large width input beam is used because the wavevector *k* of the input beam has a dispersion(Δk) due to a finite beam width *w*. The relation between Δk and w is given by [11-12]: $\Delta k = \frac{\sqrt{8}}{w}$. If we only use a 6*a wide input beam, the wave vector dispersion Δk is about 0.4. Figure 2.12 shows the calculated dispersion diagram of the 1st band for all in-plane wave vectors in the x-y plane for a wavelength λ of 1.55um. One may find that the maximum steering angle $\Delta\theta_{out}$ can be obtained only if the k vector inside the photonic crystal changes from the Γ-M direction to the Γ-X direction, or vice versa, upon the perturbation of incidence. Therefore the region on the equi-frequency contour (EFC) that we are interested is between k_x=0.6 and k_x=0.8.

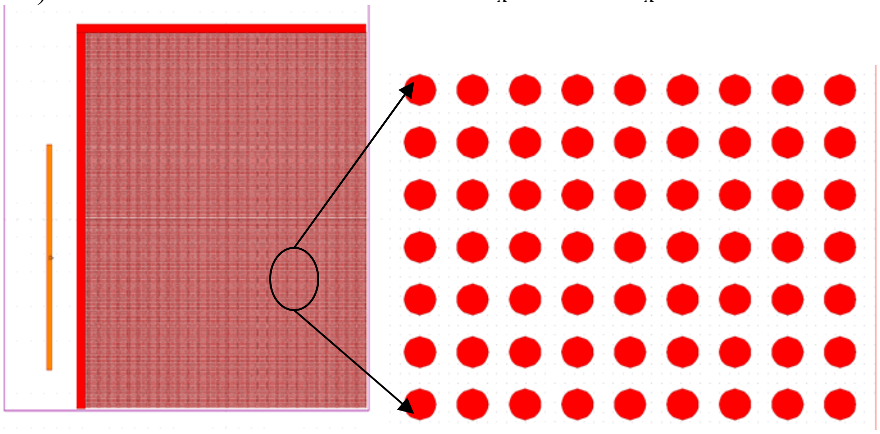

Figure 2.11: The layout of the square lattice photonic crystals with the area of 200 a*200a

However, a 6*a wide input beam gives a large value of Δk, which can't resolve the simulation points in the region of interest. For example, if we take k_x=0.7 and Δk=0.4, then the beam covers k_x from 0.5 to 0.9. The center wave vector mode would be merged inside the other wave vector modes. This is why we need to increase the beam width to minimize the k dispersion. A beam width of 120*a gives Δk of 0.0217, which provides a sufficiently small dispersion of k to reach good simulation accuracy. The larger the beam width, the more accurate the simulation is, but more time is also needed to finish the simulation. Accordingly, we need to increase the size of the simulation area to accommodate the large input beam width.

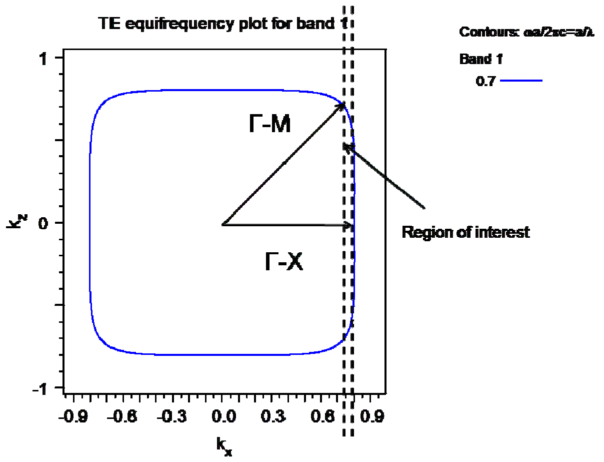

Figure 2.12: The equi-frequency contour (EFC) showing the 1st band for all in-plane wave vectors in the x-y plane

In an FDTD simulation, the grid size is an important parameter to determine the simulation accuracy. Smaller grid sizes give better accuracy at the expense of longer simulation time. In our simulation, a grid size of 0.05 was chosen to reach a good balance between these two issues. The drawing of dispersion surfaces for the refraction process is shown in Figure 2.13. Figure 2.13(a) and (b) correspond to the input angle change and input wavelength change. Figure 2.14 shows the result of the EFC analysis results based on the input angle and input wavelength change. Figure 2.15 shows the FDTD simulation results for incident angles of 10.5° and 11.3°. We can see that a change of incident angle of 0.8° results in a steering range of around 3°, which is attributed to the PC superprism effect.

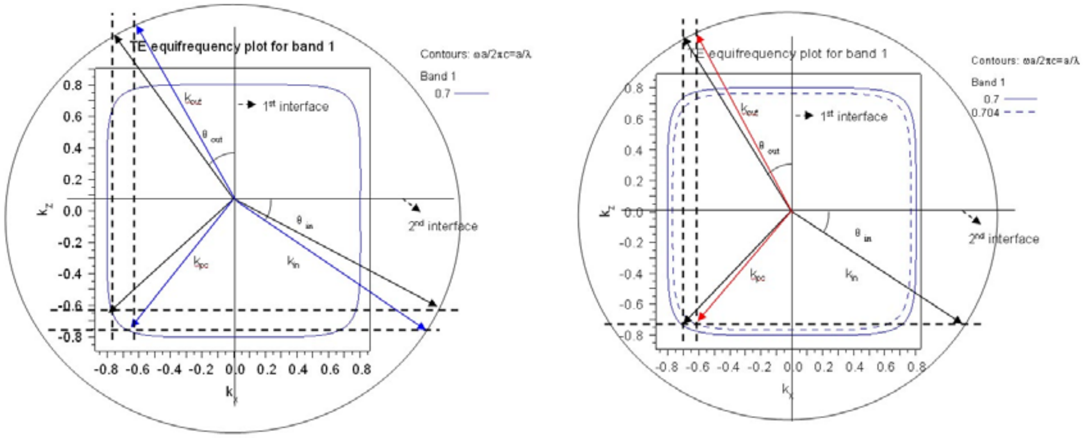

(a) (b)

Figure 2.13: The equi-frequency contour (EFC) analysis of the superprism effect with (a) input angle change and (b) input wavelength change

From the theoretical results, we can find the final output direction in FDTD through analyzing the wave front (the parallel lines in the FDTD simulation), where the k vector is perpendicular to the wave front in the homogenous medium. Outside of the PC, the k and s vector are in the same direction. We calculated the output beam direction via EFC (equi-frequency contour) analysis by obtaining $k_x=k*\sin\theta_{in}$. We then found the corresponding ky in the EFC contour. Because the k_y is conserved at the second interface, the output beam direction is: $\theta_{out}=\sin^{-1}(k_y/k_0)$. The results are plotted in Figure 2.16 as well. For EFC analysis, it assumes that the beam width is infinite. However, we can only use the finite size of photonic crystals and beam width for FDTD simulations. This difference may explain the discrepancy between the simulation results of FDTD and EFC analysis.

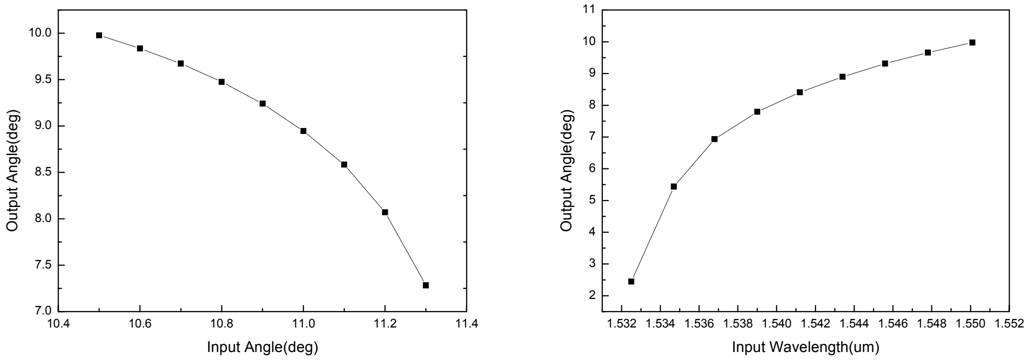

(a) (b)

Figure 2.14 Simulated output angle versus (a) the input angle and (b)input wavelength for EFC analysis

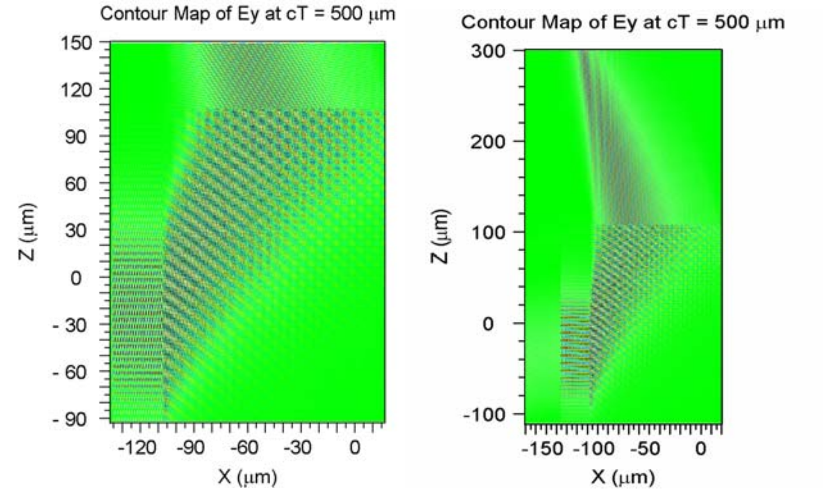

(a) (b)

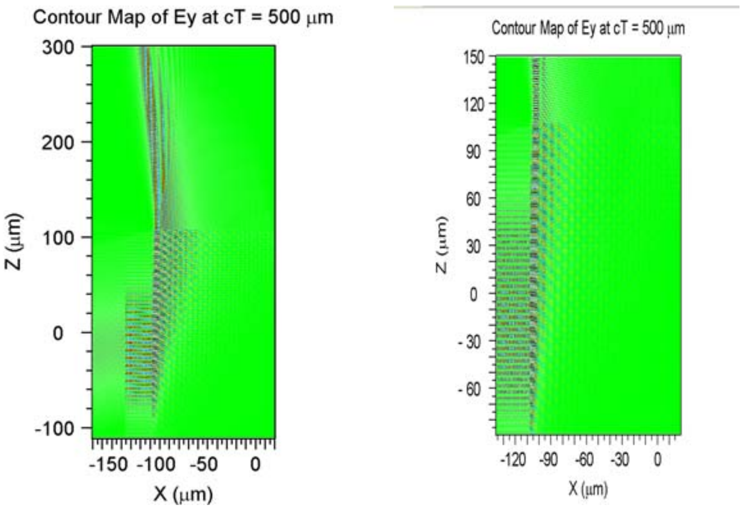

(c) (d)

Figure 2.15: FDTD simulations at input angle of (a) 10.5° (b) 10.7° (c) 11.0° and (b) 11.3°

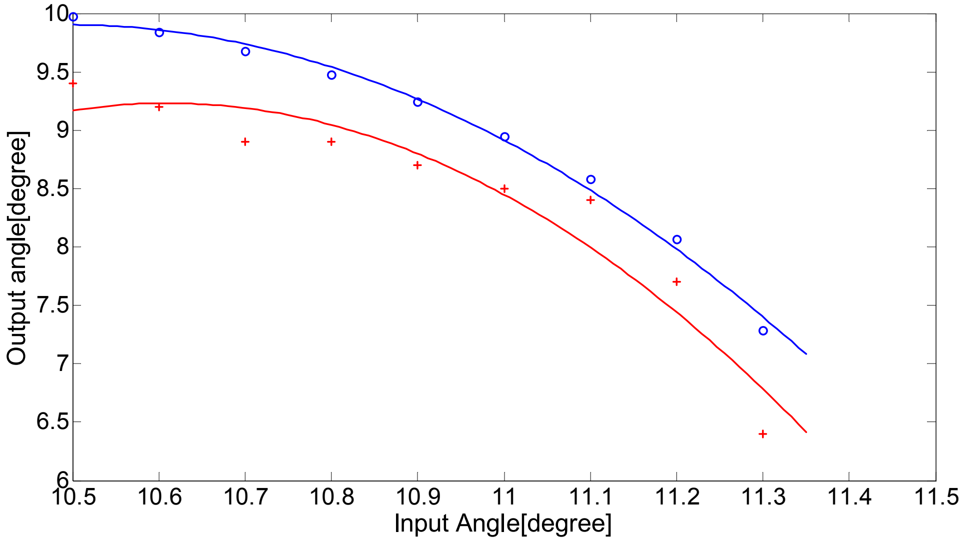

Figure 2.16: The fitting curve of the output angle *vs* input angle in the previous table

From the curve we can see the output angle decreases much faster than the input angle increases. The blue line is for the EFC contour analysis, and the red line is for the FDTD simulations. The input angle was changed from 10.5º to 11.3º, the output angle at the second interface was changed from 9.4º to 6.4º. The output angle change is approximately 4 times the input angle change.

2.5 2D PHOTONIC CRYSTAL FABRICATION

In order to demonstrate the laser beam steering, we fabricated the two dimensional polymer based photonic crystals by a double-exposure holographic interference method [13]. SU-8 photoresist was used for fabrication, and the laser beam was a He-Cd laser emitting at 325nm. A mirror was used to create the interference pattern. In order to carry out the beam steering test using a large collimated beam (1-2mm diameter), we made the photonic crystals parallel stacked with respect to the glass substrate. The scheme in Figure 2.17 shows the complete fabrication process for the horizontally stacked photonic crystals. A pattern of Cr was deposited to block UV light to open trenches for the developing process. First, a Cr-patterned glass substrate was prepared using photolithography and a lift-off technique. After coating the adhesion promoter, a film of 10μm thick SU-8 2007 was spin-coated on the glass substrate. After baking the sample by ramping the hotplate from 65ºC to 95ºC, the double exposure was carried out with the 325nm laser beam. The post exposure baking step was performed at the same condition as the pre-bake. Lastly, the sample was developed at room temperature. Figure 2.18 gives the schematic and actual recording setup.

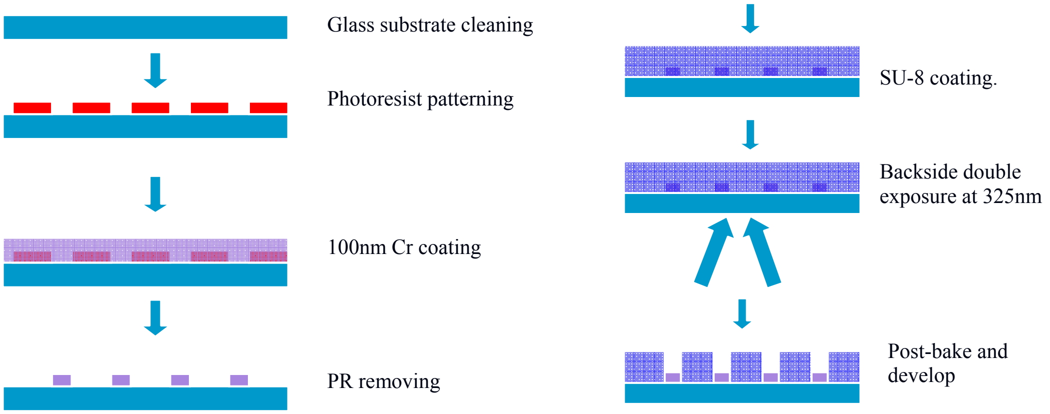

Figure 2.17: The scheme of fabricating horizontally stacked photonic crystal on the glass substrate

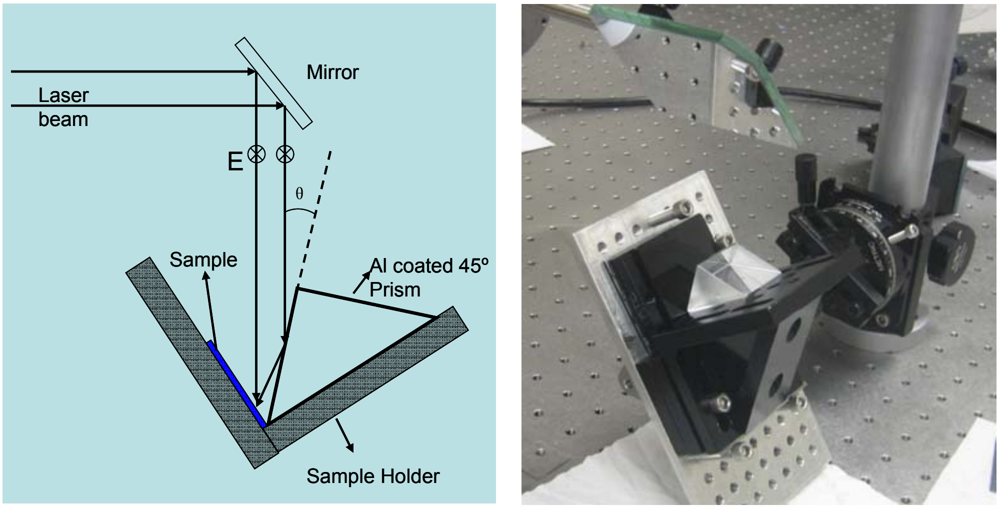

(a) (b)

Figure 2.18: Double exposure of 2-beam holographic fabrication of horizontally stacked 2D photonic crystal

Figure 2.19 (a) and (b) shows the SEM pictures of the developed photonic crystal structures, where the period has a feather size of around 1.0µm. Figure 2.19(c) shows the schematic view of the laser diffraction setup. Figure 2.19(d) shows the 442nm laser diffraction pattern. From the diffraction pattern, we can clearly see the center spots, which corresponds with the zeroth order (0,0) beam diffraction and the two first orders [(0,1) and (0,-1) order]. The first order diffraction angle at 27.2º indicates the period of the photonic crystals to be 0.97μm, which is consistent with the simulation. The periodic photo polymer belts with a period of 30um also have a grating effect, which produces the discrete spots horizontally in the *z* direction. The photonic crystal diffraction effect is in the vertical *y* direction, which appears in a line of weaker spots on the top (0,1) and bottom(0.-1) of the screen. Beams (0,1) and (0,-1) are symmetric around the input beam and have the same intensity.

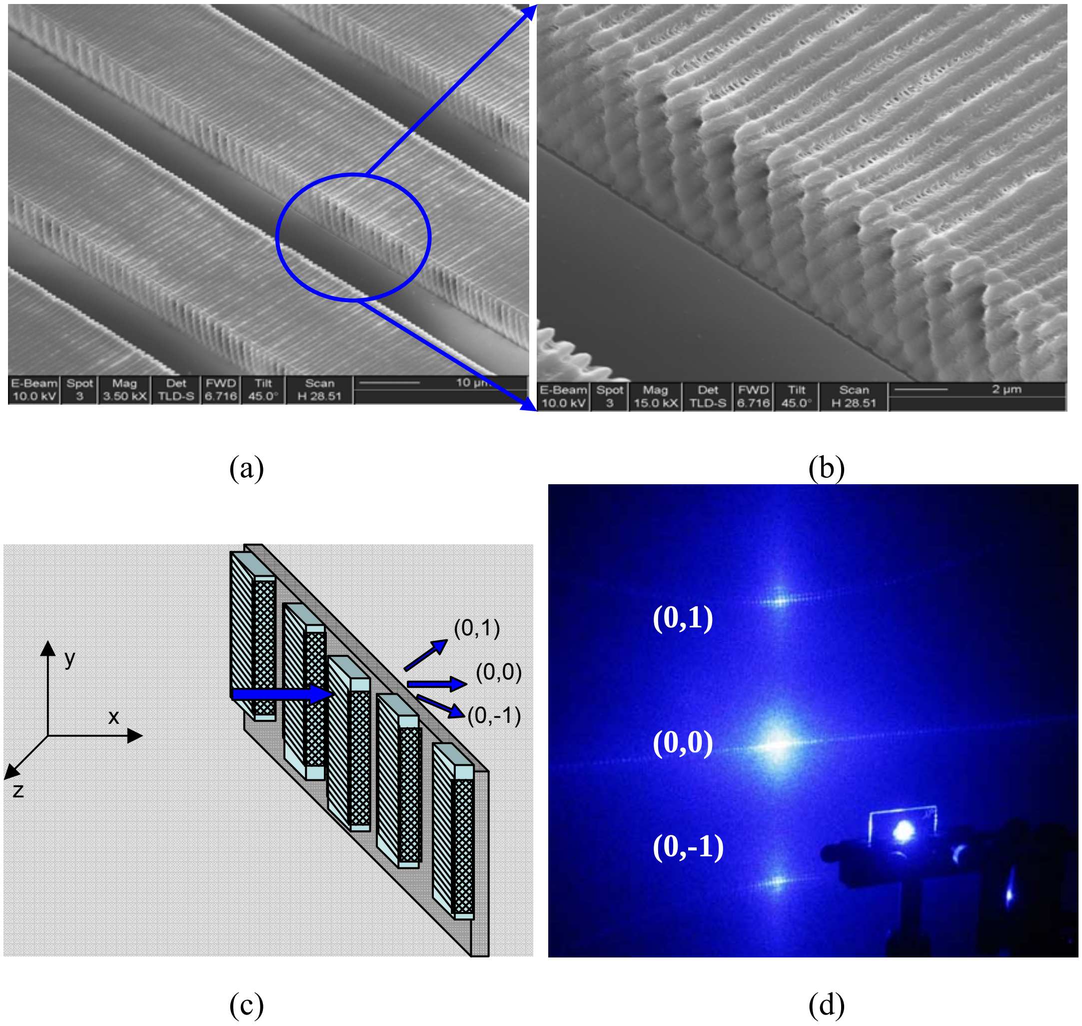

Figure 2.19: (a) low and (b) high magnification view SEM pictures of the horizontally stacked photonic crystal structures fabricated using SU-8. (c) The schematic laser diffraction setup. (d) The 442nm laser diffraction pattern of the fabricated photonic crystals

In this way, we have successfully achieved the horizontally stacked 2D polymer based photonic crystal structures through double-exposure holographic interference. Note that this diffraction experiment with input and output surfaces parallel to each other was solely intended for the confirmation of a photonic crystal lattice structure. The superprism effect must be investigated with perpendicular input and output surfaces and the details will be presented in the next section.

The corresponding layout of the polymer based 2D photonic crystals with an area of $100a\times100a$ is shown in Figure 2.20, where a is the lattice constant of the PC structures. In our simulation, the input beam wavelength λ is 1.55μm and the lattice constant a is 1.0μm ($a/\lambda=0.6452$) the material index n is assumed to be 1.6, which corresponds to the index of the SU-8 polymer at the wavelength of interest. The 50° angle corresponds to the recorded result during the experiment.

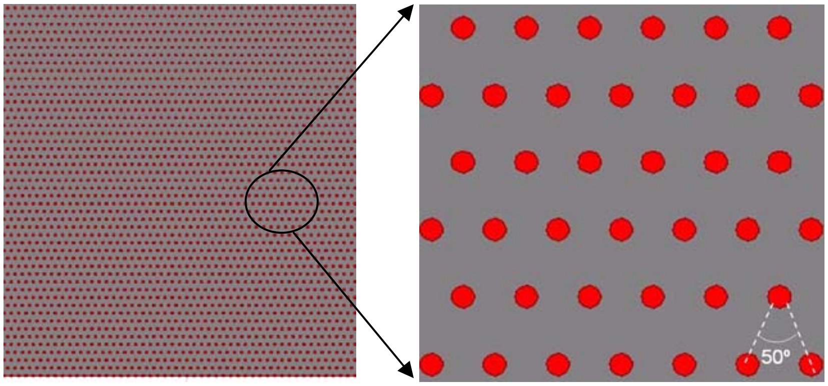

(a) (b)

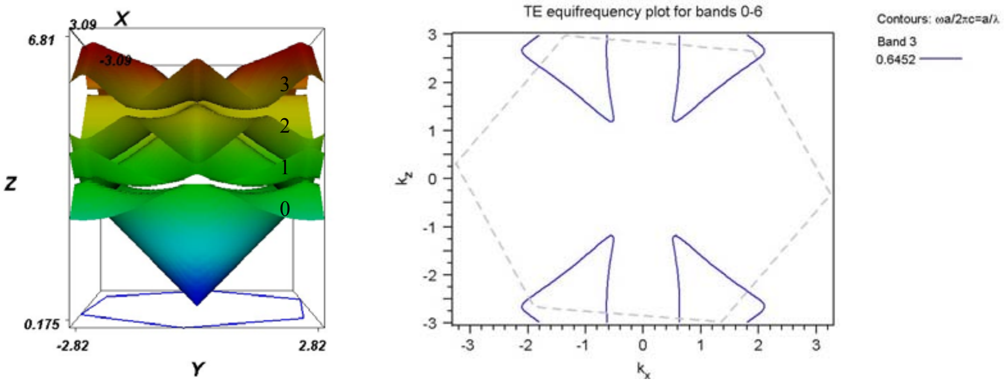

(c) (d)

Figure 2.20: (a) (b) Layout of the photonic crystals in x-z plane. (c) 3D band structure of the polymer based photonic crystals. The x,y axis represents k_x and k_z, respectively. z represents the frequency. (d) The EFC (Equi-frequency Contour) at certain freqeuency (ωa/2πc=a/λ=0.6452) for band 3

Figure 2.20 (c) shows the 3D view of the first four bands of the two dimensional polymer based photonic crystals. The lowest band is band 0, then band 1, band 2 and so on, indicated by numbers. The EFC (Equi-frequency Contour) can be achieved by intercepting the 3D band structure by a certain frequency plane which is perpendicular to the Z-axis. In the EFC analysis (Figure 2.20 (d)) we are interested in band 3, because it corresponds to the beam wavelength at 1.55μm, and it has the highest possibility of manifesting the superprism effect.

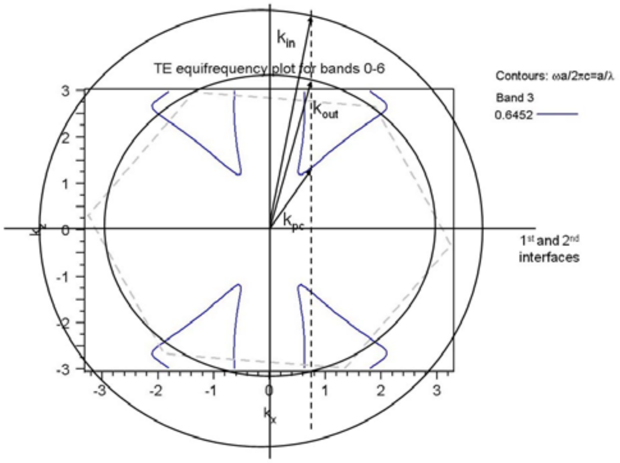

Figure 2.21: Analysis of the refraction process when the input and output surfaces are parallel

In Figure 2.21, we show the EFC analysis for the two parallel interfaces. k_{in} is the input wave vector, k_{pc} is the wave vector inside the photonic crystal and k_{out} is the output wave vector. The small and big circles are the air contour and medium contour, respectively. If the medium is also air, then the two circles are the same. The output wave vector is given by the conservation law of the tangential wavevector component at the interfaces [11]. Therefore the final results of the input and output wave vectors satisfy Snell's Law. In this way, the photonic crystal superprism effect is cancelled by the two parallel interfaces. To avoid this effect, we have to use the photonic crystal effect using two nonparallel interfaces of the photonic crystal.

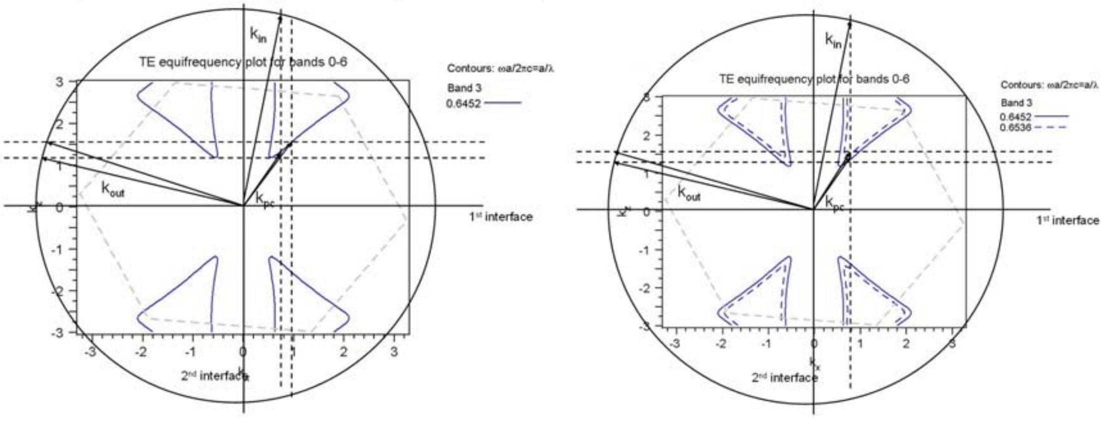

(a)

(b)

Figure 2.22: EFC analysis for (a) the input angle change and (b) input wavelength change

In Figure 2.22, we show the EFC analysis of the refraction process with two perpendicular interfaces. The laser beam first enters the photonic crystal area from the air or medium. After two refractions, the laser beam enters the air or medium again. The input (or 1st) and the output (or 2nd) interfaces are perpendicular to each other. k_{in} is the input wave vector, k_{pc} is the wave vector inside the photonic crystal. k_{out} is the output wave vector after the 2nd interface. k_{in} and k_{pc} have equal k_x component due to the momentum conservation at the 1st interface. k_{pc} and k_{out} have an equal k_z component due to the momentum conservation at the 2nd interface. Momentum conservation is indicated by the dashed line in the figure. When the input angle or wavelength is changed, the corresponding wave vector k_{in} will be changed, as well as k_{pc}. k_{out} will also be changed according to the momentum conservation. In this analysis, we can find the exact cross point of the EFC contour with the conservation dashed lines, so we can find the output angle change. This is also the beam steering principle. In Figure 2.23, we gave the simulated beam steering angle curves with respect to the input angle and input wavelength. The cross point is achieved at around 1.55μm wavelength with a 10° input angle. From these two curves, we can see when the input angle changes 2°, the output angle can change around 2.5°. As the input wavelength changes by approximately 30nm, the output angle changes by approximately 4°.

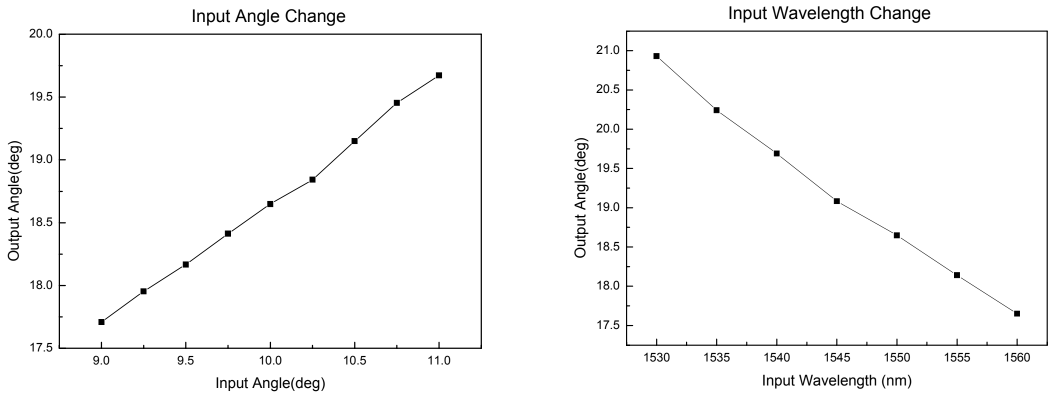

(a) (b)

Figure 2.23: The output angle change *vs* (a) input angle change and (b) input wavelength change

2.6 BEAM STEERING TEST RESULTS

The beam steering experiment was carried out at 1.55μm. Figure 2.24(a) is the schematic view of the optical beam steering setup. First, the input beam enters the glass substrate and then the photonic crystal region. Some part of the beam will be reflected at the glass/air interface, and some part will directly pass through the photonic crystal. The beam which has refractions at the glass/PC interface and the PC/air interface at the edge can be captured by the IR camera. Figure 2.24(b) is the actual experimental setup. We observed three output beams, the transmitted beam, the reflected beam and the superprism steering beam. The steering beam was observed by an IR camera.

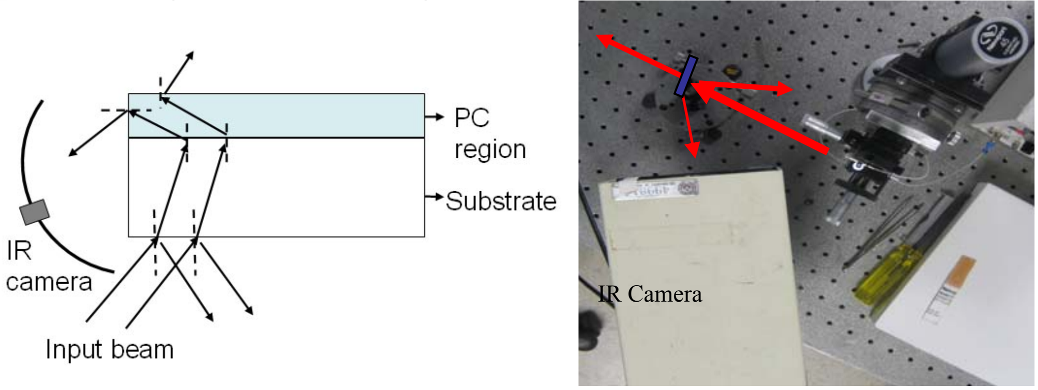

(a) (b)

Figure 2.24: (a) Schematic view and (b) experimental setup of the beam steering test

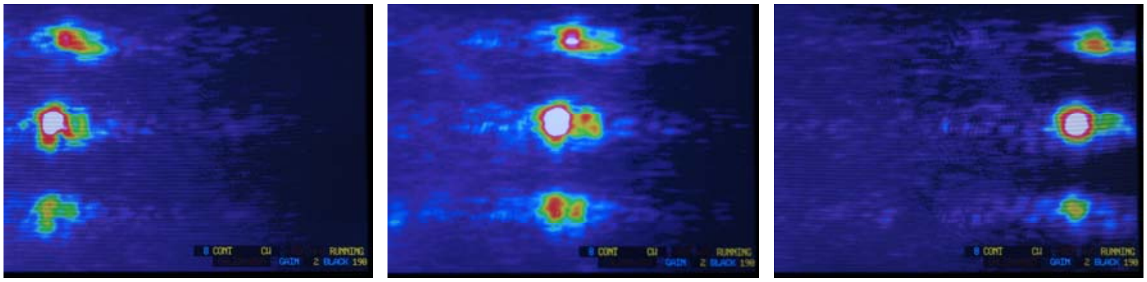

Figure 2.25: Typical IR camera view of the steering output beams for three different input angles at 1.55μm wavelength

In Figure 2.25, we show the typical output steering beam image capture by the IR camera at three different input angles. The vertical discrete spots are due to the polymer belts or bars grating effect. As the input angle or input wavelength changes, the steering discrete beam spots move simultaneously in the horizontal direction, which corresponds to the output angle change. Figure 2.26 gives the measured optical beam steering experiment results for the input wavelength change and the input angle change. The steering angle is around 10º for a 30nm input wavelength change and 6º for a 1.5º input angle change. Compared with the simulations, the experiment results differ because the photonic crystals in the simulation are for ideal configurations and shapes.

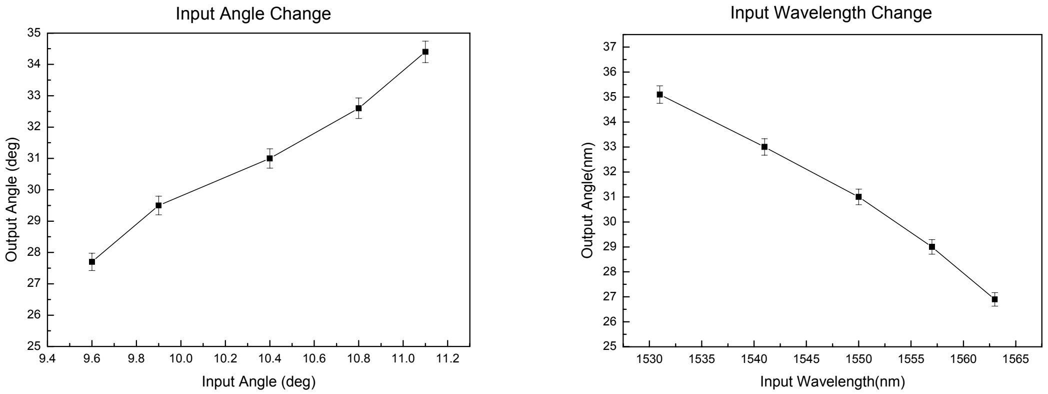

(a) (b)

Figure 2.26: The beam steering experiment result based on the (a) input angle change and (b) input wavelength change

In summary, we carried out the polymer-based photonic crystal beam steering simulation and the fabrication of horizontally stacked photonic crystal structures through holographic interference method using photo polymer SU-8. The beam steering was studied in detail using the EFC (Equi-frequency Contour) method. SEM pictures and a laser diffraction pattern of the fabricated photonic crystal were also shown. Optical beam steering at 1.55μm was carried out for the input angle change and the input wavelength change.

2.7 REFERENCES

[1] E. Yablonovitch, "Inhibited spontaneous emission in solid-state physics and electronics," Phys. Rev. Lett. 58, 2059-2062, (1987).

[2] S. John, "Strong localization of photons in certain disordered dielectric superlattices," Phys. Rev. Lett. 58, 2486-2489 (1987).

[3] H. Kosaka, T. Kawashima, A. Tomita, M. Notomi, T. Tamamura, T. Sato and S. Kawakami, "Superprism phenomena in photonic crystals," Phys. Rev. B 58, R10096 (1998).

[4] H. Kosaka, T. Kawashima, A. Tomita, M. Notomi, T. Tamamura, T. Sato, S. Kawakami, "Superprism phenomena in photonic crystals: toward microscale lightwave circuits," J. Lightwave Technol. Vol. 17, 2032 (1999).

[5] M. S. Li, S. T. Wu and Andy Ying-Guey Fuh, "Superprism phenomenon based on holographic polymer dispersed liquid crystal films", Appl. Phys. Lett. 88, 091109 (2006).

[6] H. Kosaka, T. Kawashima, A. Tomita, M. Notomi, T. Tamamura, T. Sato and S. Kawakami, "Photonic crystals for micro lightwave circuits using wavelength-dependent angular beam steering," Appl. Phys. Lett. 74, 1370, (1999).

[7] S.Y. Lin, V. M. Hietala, Li Wang, and E. D. Jones, "Highly dispersive photonic band-gap prism," Opt. Lett. 21, 1771, (1996).

[8] J. Chen, W. Jiang, X. Chen, L. Wang, S. Zhang, and R. T. Chen, "Holographic three-dimensional polymeric photonic crystals operating in the 1550 nm window," Appl.

Phys. Lett. vol. 90, 093102 (2007).

[9] T. Kondo, S. Juodkazis, and H. Misawa, “Reduction of capillary force for high aspect-ratio nanofabrication,” Appl. Phys. A 81, 1583–1586 (2005).

[10] S. Noda, T. Baba, “Roadmap on photonic crystals”, Springer (2003).

[11] W. Jiang, R. T. Chen, and X. Lu, “Theory of light refraction at the surface of a photonic crystal,” Phys. Rev. B 71, 245115 (2005).

[12] W. Jiang and R. T. Chen, “Symmetry-induced singularities of the dispersion surface curvature and high sensitivities of a photonic crystal,” Phys. Rev. B 77, 075104 (2008).

[13] T. Kondo, S. Juodkazis, V. Mizeikis and H. Misawa, “Holographic lithography of periodic two- and three-dimensional microstructures in photoresist SU-8,” Optics Express, 14, 7943 (2006).

Chapter 3 *Polymeric point-to-point waveguide array with embedded 45° micro-mirrors*

3.1 INTRODUCTION

In past years, optical interconnects were extensively investigated to provide high-density and high speed data transmission [1-10]. Traditional electrical circuits have the disadvantage of bandwidth limitations, electromagnetic interference, and the skin effect [2]. Polymer based fully embedded board level optical interconnects attract more and more attention because of its low transmission loss, compatibility with printed circuit board (PCB), and high speed data transmission [3]. On the board level of optical interconnects, 45° total internal reflection (TIR) micro-mirrors play a significant role in vertical-horizontal optical coupling [4-12]. Many techniques can be used to fabricate the 45° micro-mirrors, such as polishing and soft molding [4,5], sawing [6,7], direct cutting [8], tilted exposure [9], ultra-precision machining (UPM) [10], and Deep Proton Writing(DPW) [11-12]. The cutting or sawing method fabricated 45° surfaces separately, which has a disadvantage of low repeatability. In the paper of Wang *et al* [9], they also used the tilted exposure under D.I. water to fabricate the waveguide devices with 45° angle structures using the LightLink^{TM} photopolymer. They used the air/polymer interface instead of metals as the coupling mirror, which has a low coupling efficiency. The UPM method used a very expensive, ultra-precision machining system to form the metal hard mold, which is not suitable for every user from the cost point of view. In this report, we present a very economic method with combining a tilted exposure and metal electroplating process to achieve the metallic optical waveguide hard mold and the 45° total internal reflection (TIR) micro-mirror surfaces simultaneously. Once a high quality metallic mold was successfully fabricated, it can be used for waveguide fabrication many times, which can reduce the cost of each device further and also guarantee the quality of the embedded 45º Au-coated mirrors.

In the process of optical waveguide metal mold fabrication, the waveguide pre-mold(50um×50um cross section) with reverse 45º surfaces on both ends was first prepared using SU-8 (from MicroChem) through tilted exposure under D.I. water. The SU-8 layer acted as a sacrificial layer which was removed after the electroplating process. After achieving the waveguide pre-mold, metal Ni was electroplated onto the SU-8 defined waveguide trenches. As the electroplating process finished, SU-8 was removed completely using remover PG (from MicroChem). In this way, the metal mold with 45º surfaces on both ends was successfully fabricated. A polymeric optical waveguide array with fully embedded 45º total internal reflection (TIR) micro-mirrors was formed by UV imprinting using the fabricated hard mold. The metal Ni mold fabrication and polymeric waveguide imprint process is schematically shown in Figure 3.1 (a) and (b), respectively.

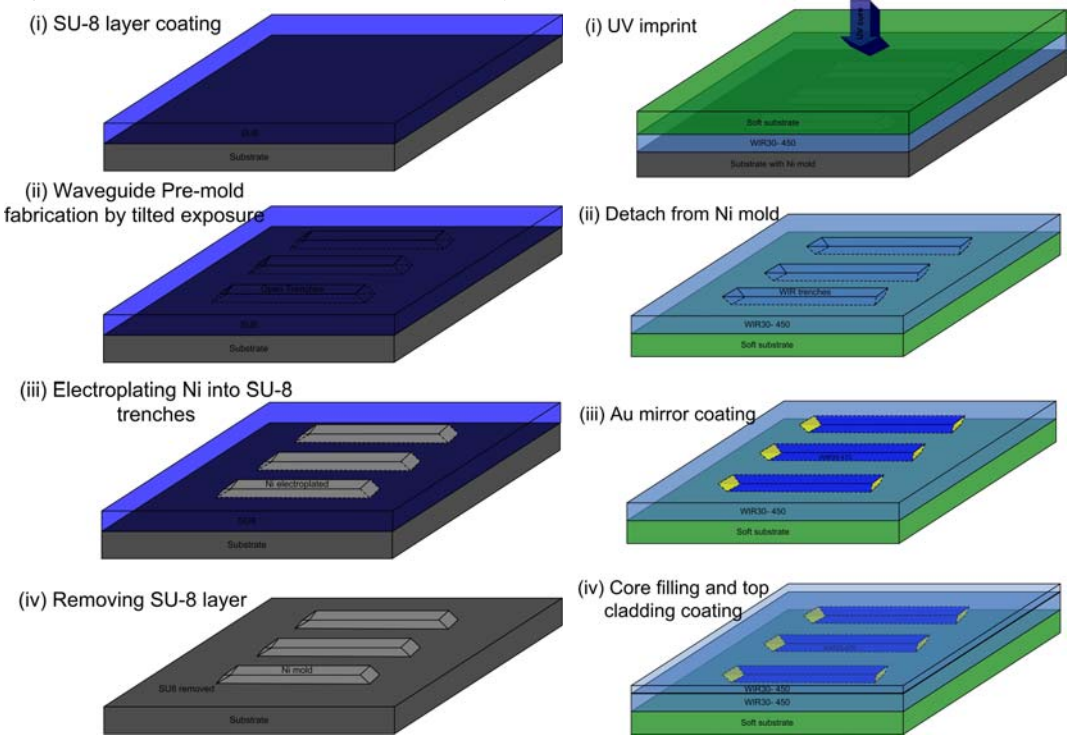

(a) (b)

Figure 3.1: Schematic view of whole process of (a) Ni mold fabrication and (b) polymeric waveguide imprint

3.2 PREPARATION OF SU-8 PRE-MOLD WITH 45º SURFACES

In order to fabricate a Ni metal mold through electroplating method, we first prepared the pre-electroplating mold (called pre-mold) for the waveguide, which defines the shape and structure of the waveguide metal mold. A negative photoresist SU-8 2025 was used to prepare the pre-mold, which was spin-coated with a thickness of 50um. The refractive index of SU-8 is about 1.62 at 365nm. If directly exposed in air, the maximum refraction angle within SU-8 is only 34.2º. This process is simply governed by Snell's law: $n_{medium} \times \sin(\theta_i) = n_{SU-8} \times \sin(\theta_r)$, θ_i and θ_r are the incident and refractive angles in the medium and SU-8, respectively. To achieve a 45º refractive angle in SU-8, de-ionized (D.I.) water (refractive index of 1.34 at 365nm) was selected as the input media. The tilted exposure setup is shown in Figure 3.2. When the UV light (mercury lamp) is vertically shined onto the D.I. water, the tilted angle for the substrate in water is 58.7º to make a 45º refraction angle within SU-8.

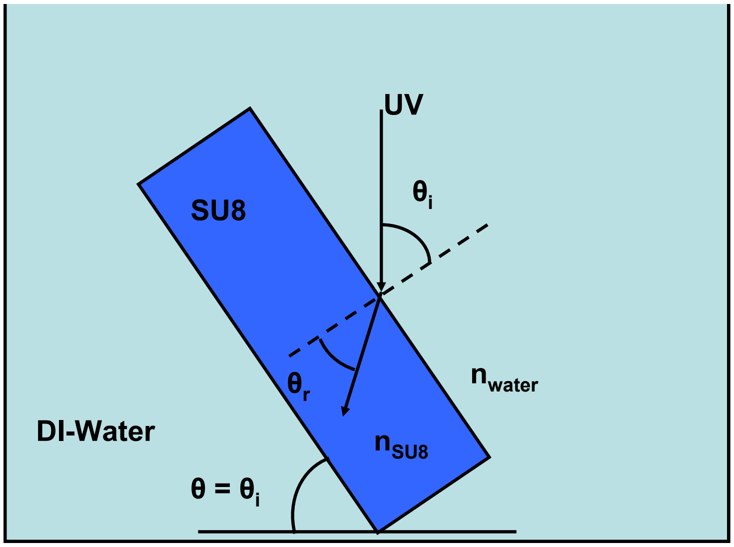

Figure 3.2: Schematic view of the tilted exposure on SU-8 in DI-water (θ_i and θ_r are the incident and refractive angles, respectively)

These are the few steps in SU-8 pre-mold preparation process, as shown in Figure 3.3:

(1) E-beam evaporate-coating 10nm/100nm of Ti/Au electroplating seed layer on the Si substrate.

(2) Spin-coating a thin layer of Omnicoat and 50um thick of SU-8 2025, prebake on a hotplate at 65ºC for 2-3min then ramp to 95ºC, stay at 95ºC for 6min, and cooling down to room temperature. Omnicoat was used as a sacrificial layer in order to completely remove cross-linked SU-8 in remover PG after electroplating.

(3) A straight waveguide photomask (50um in width, 250um in period, and 65mm in length) was used to do the vertical exposure. A UV filter was added to cut off the light wavelength below 350nm.

(4) A small window mask was utilized for the 1st and 2nd tilted exposures under D.I. water. A aluminum metal stage was used at a 58.7º angle to hold the sample and the photomask. These two exposures were identical except that the small window was moved from one end of the waveguide patterns to the other end. During the exposure process, the air bubbles need to be removed completely to avoid unexpected diffractions. Index matching material, such as silicone oil, was filled between the photomask and the SU-8 film. After exposure, silicone oil can be easily rinsed away by DI-water.

(5) Post-exposure-bake(PEB) was carried out on a well-controlled hotplate by ramping from 50ºC to 95ºC, staying at 95ºC for 6min, and cooling down to room temperature on the hotplate itself. Lastly, the sample was developed. Before performing Ni electroplating, SU-8 residue inside the waveguide trenches were removed completely

by O_2 plasma ashing for a few minutes. No damage on the SU-8 pre-mold was observed after the O_2 plasma ash.

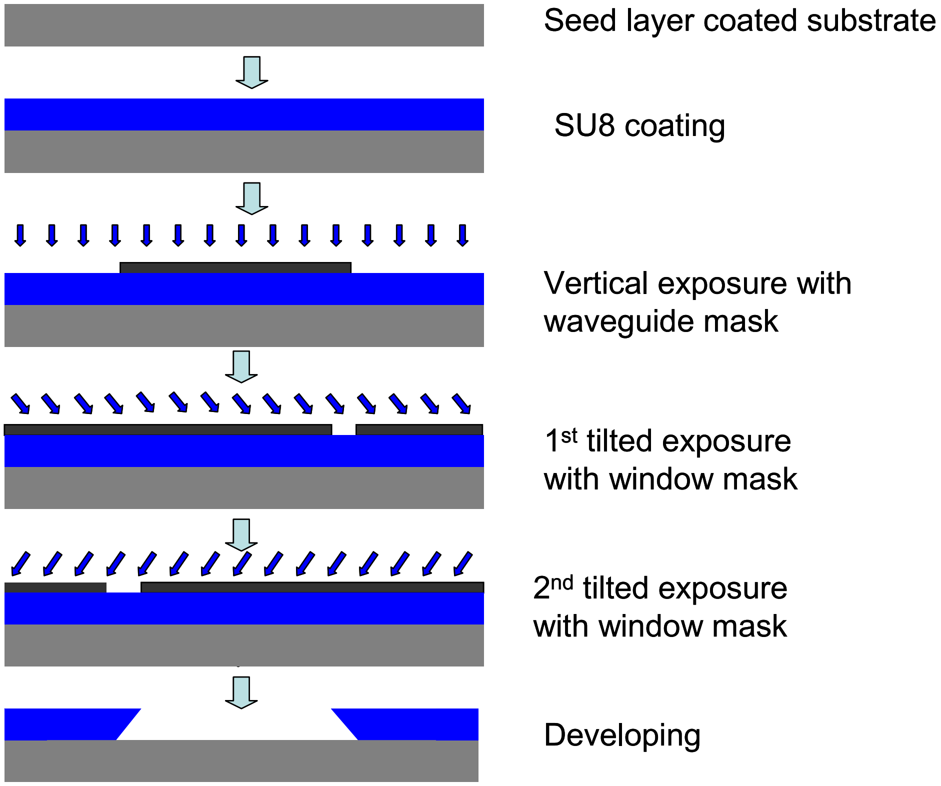

Figure 3.3: Schematic process of SU-8 pre-mold with 45° surfaces fabrication

Figure 3.4 shows optical pictures of the SU-8 pre-mold waveguide trenches in (a) small and (b) large magnification. The black squares at the end of waveguide array correspond to the reverse 45° surfaces. They are shown black because the light was not reflected back into the microscope but into the waveguide trench direction.

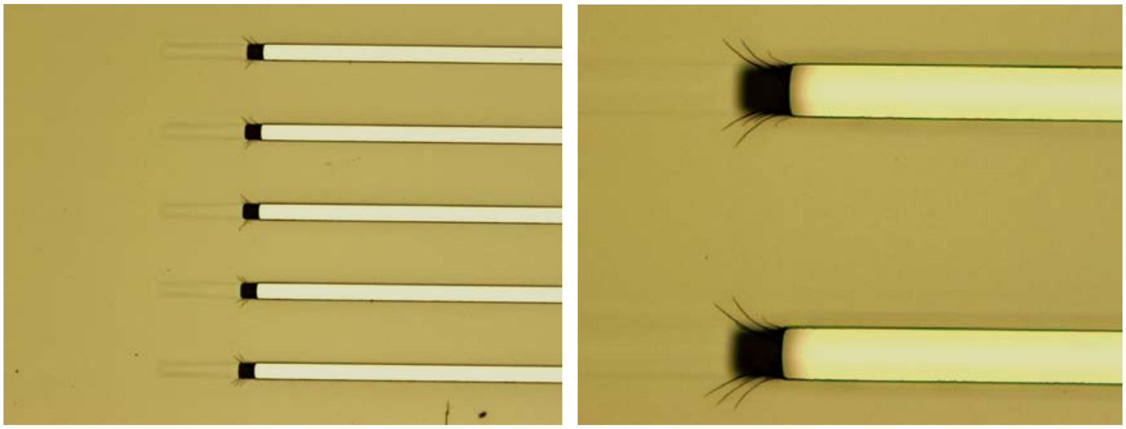

(a) (b)

Figure 3.4: Top view of SU-8 pre-mold in (a) small magnification and (b) large magnification

In order to inspect the quality of the waveguide and 45° surfaces on both ends of the waveguide trenches, the fabricated SU-8 pre-mold samples were cleaved in the perpendicular and parallel direction of the waveguide trench, respectively. The cleaved samples were sputtered with Au and viewed under a Scanning Electron Microscope (SEM). Figure 3.5 shows the typical SEM pictures of the SU-8 pre-mold. Figure 3.5(a) shows the cross section view in the perpendicular direction of the waveguide trench. Figure 3.5(b) shows a perfect vertical shape of the waveguide trench. Figure 3.5(c) shows the cross section view in the parallel direction of the waveguide trench. The cleaving line must be exactly in the middle of the trench in order to view the 45° surfaces directly. The 45° surfaces angle was measured in Figure 3.5(d) to be 45.5°, only deviating 1% from the designed value. Based on several rounds of fabrication, this result is repeatable. It also confirms our theoretical calculation on the tilted exposure in water.

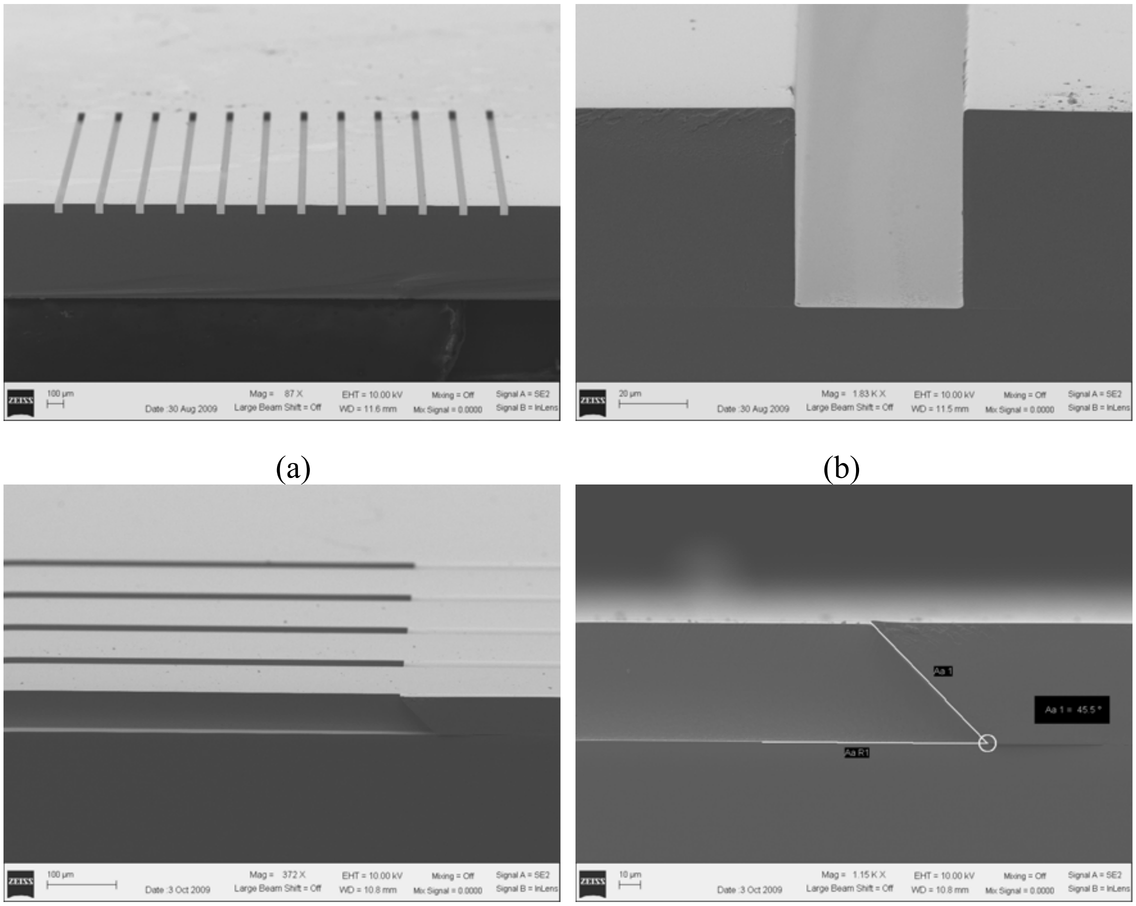

(a) (b)

(c) (d)

Figure 3.5: SEM pictures of SU-8 pre-mold cross section with 45º surfaces at the end of the waveguide in the direction (a) perpendicular and (c) parallel to the waveguide trench

3.3 ELECTROPLATING NI METAL HARD MOLD

After successfully achieving SU-8 pre-mold with reverse 45º surfaces on both ends, metal Ni was electroplated into the waveguide trenches. The Ni electroplating kit was purchased from Caswell Inc. The schematic of the electroplating setup is shown in Figure 3.6. The components of the Ni plating solutions are given in Table 3.1. A Ni plate was placed on the anode and the SU-8 based pre-mold was placed on the cathode. On the anode, Ni metal was oxidized to Ni^{2+} ions into the solution and on the cathode, and Ni^{2+} ions were reduced to Ni metal and deposited into the SU-8 defined trenches. In this way, Ni metal grows inside the waveguide to form the metal hard mold. In order to achieve a strong adhesion between the Ni mold and the seed layer, a very small plating current density (1-2mA/cm^2) was first used followed by transiting into a large current density (10mA/cm^2). At the end of plating process, small current density (1-2mA/cm^2) was used again to achieve a good terminating surface. Plating speed is around 120nm/min at 10mA/cm^2. To achieve 50um of thickness, the typical plating time is around 6-7hrs. After finishing the Ni plating process, the SU-8 pre-mold was removed from the substrate with heated Remover PG, and its residue was removed by an O_2 plasma in the Oxford RIE (reactive ion etching) system.

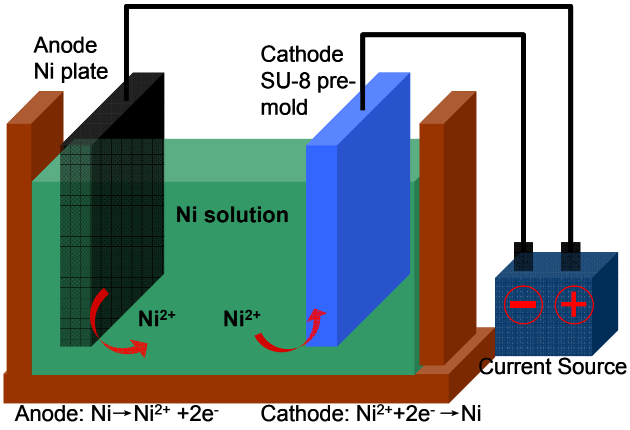

Figure 3.6: Schematic view of the Ni electroplating system

Ni solution composition	Percentage
$Ni(NH_3SO_3)_2 \cdot 4H_2O$	350-450g/L
$NiCl_2 \cdot 7H_2O$	5-30g/L
H_3BO_3	35-40g/L

Table 3.1: Ni plating composition

Figure 3.7 exhibits the SEM pictures of plated waveguide metal Ni metal hard mold on Si substrate. Figure 3.7(a) gives a top view of the Ni hard mold with 12 channels. The width of the waveguide was measured to be 49.1um. To measure the actual slant angle of 45º surfaces at the mold waveguide ends, the sample was cleaved between two waveguide lines. Figure 3.7(b) gives a side view of the waveguide mold. We measured the actual slant angle of the 45º surfaces to be 44.5º (Figure 3.7(c)), which is highly consistent with the SU-8 pre-mold reverse angle measurement. This result is also repeatable based on our experiment results. Figure 3.7(d) gives the surface profile image of the waveguide metal mold, which was scanned at the center area by a Dektak 150 Surface Profiler. The height at the end of waveguide is a little larger than that in the middle because the electric field in the electroplating process is stronger at the end than the middle. More Ni ions are attracted and Ni grows faster at the end region. This small difference proved to have no negative effect on the device's performance.

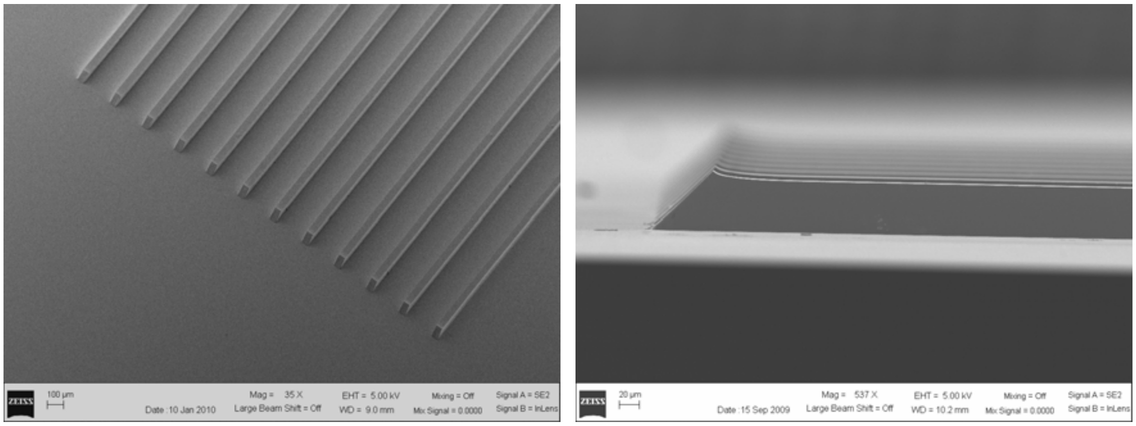

(a) (b)

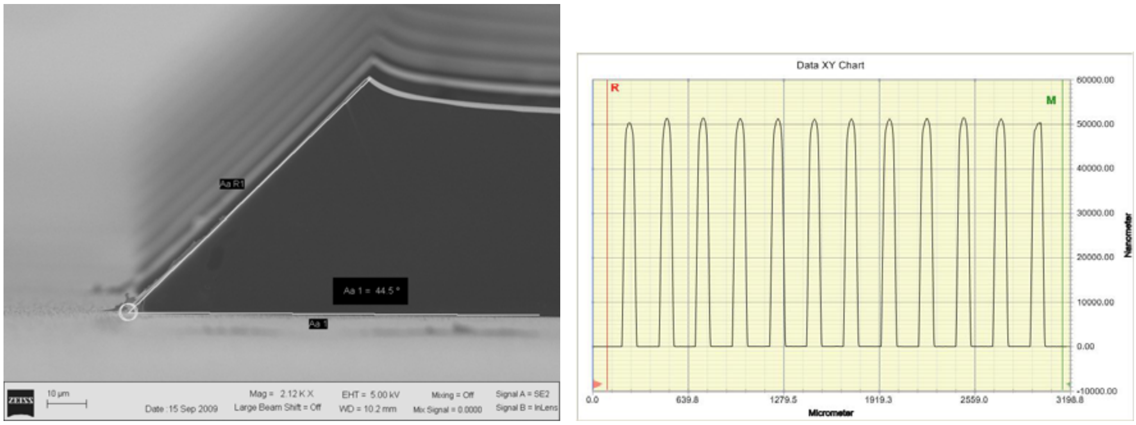

(c) (d)

Figure 3.7: (a) Top view SEM picture of the Ni hard mold with 12 channels on Si substrate. (b) Side view SEM picture of Ni hard mold on Si substrate. (c) Large magnification of the side view of 45 surfaces. The angle shown is 44.5º. (d) Surface profile image of the waveguide metal mold

3.4 POLYMERIC WAVEGUIDE DEVICE FABRICATION

Using the electroplated Ni waveguide hard mold, we successfully fabricated the waveguide devices by UV imprint technique. The UV curable polymers were the WIR30 series (from ChemOptics). WIR30-450(index at 850nm: 1.45) and WIR30-470(index at 850nm: 1.47) are for the bottom/top cladding and the waveguide core, respectively TEONEX thin film (from Dupont Teijin Films Inc.) with a thickness of 200um was used as the TOPAS substrate.

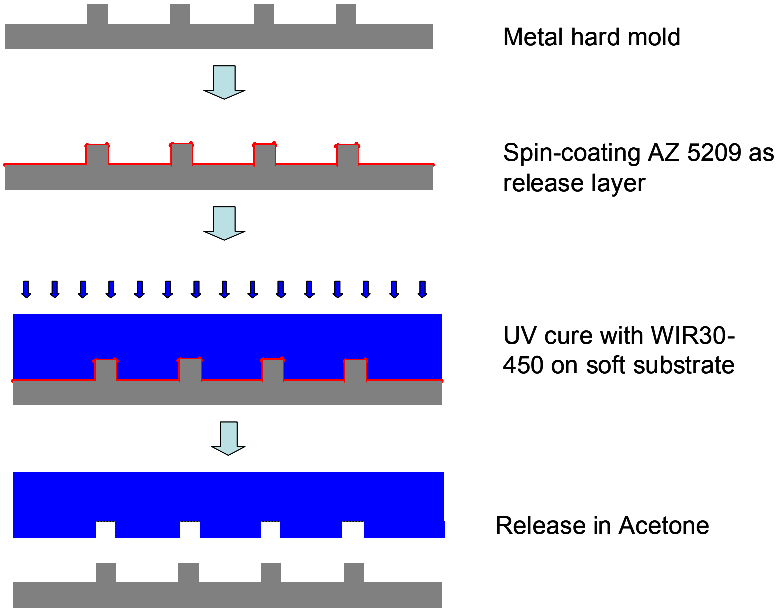

Figure 3.8: Schematic of waveguide device fabrication using UV imprint technique

The process for UV imprint is shown in Figure 3.8:

(1) Spin-coating and baking ZAP-1020 as the adhesion promoter onto the TOPAS film substrate, then baking at 110ºC for 5min.

(2) Spin-coating WIR30-450 for the bottom cladding, then UV curing in N_2 for 8min.

(3) Spin-coating AZ5209 on Ni hard mold as the release layer.

(4)Dispense a small amount of WIR30-450 on the Ni mold. Put the film on top with pressure to remove the air bubbles, then UV cure to make the core trenches.

(5)Peel off the film substrate from the Ni waveguide mold in acetone. The SEM pictures of the imprinted waveguide trenches on soft film substrate are shown in Figure 3.9.

(6) Evaporate-coating 200nm Au at the 45° surfaces on the waveguide trench ends.

(7) Filling with WIR30-470 core material and then UV curing in N_2. In the filling process, excess WIR30-470 is scraped off carefully using a PDMS pad, and there is no residue outside of the trenches.

(8) Spin-coating WIR30-450 as a top cladding and UV curing. Hence, the polymeric waveguide with fully embedded 45º total internal reflection (TIR) micro-mirrors was successfully fabricated. The core filling and Au mirror coating process is schematically shown in Figure 3.10.

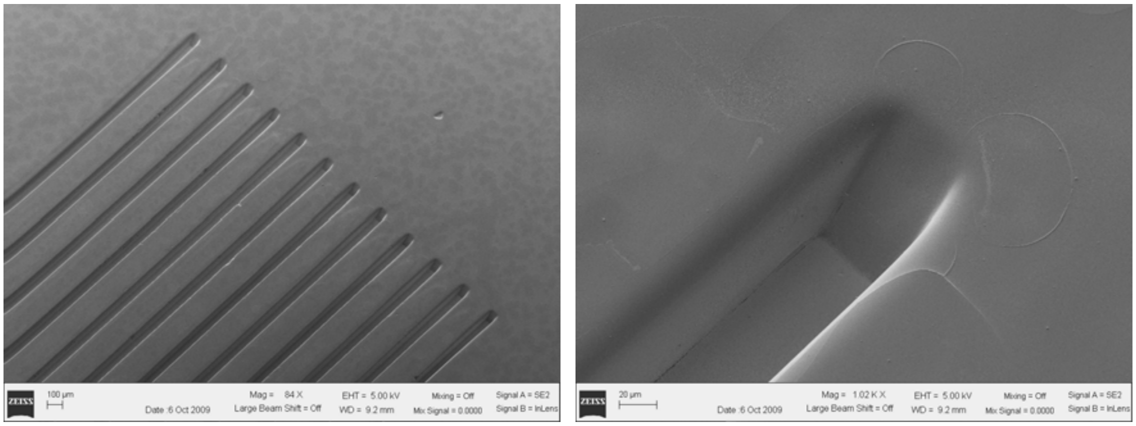

(a) (b)

Figure 3.9: (a) SEM image of the imprinted device before core material filling, (b)in larger magnification

In the experiments, we found the Au mirror can be achieved by lift-off or wet etching methods. Both methods give high quality micro-mirrors. Cr or Ti was used before Au coating in order to increase the adhesion strength with the WIR polymers.

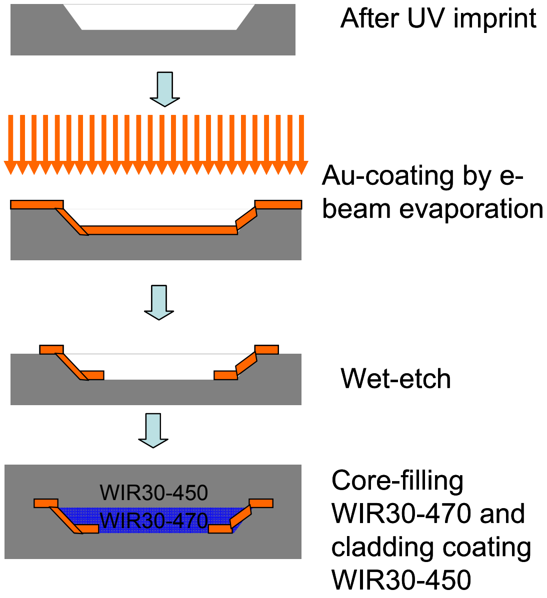

Figure 3.10: Schematic of the mirror coating, core filling and cladding coating process

The fabricated polymeric waveguide array device is shown in Figure 3.11. On the left hand side, Figure 3.11(a) is the whole device with input and out Au mirrors shown. The right hand side of Figure 3.11(b) is the closer view of the Au mirror, which is taken under the optical microscope.

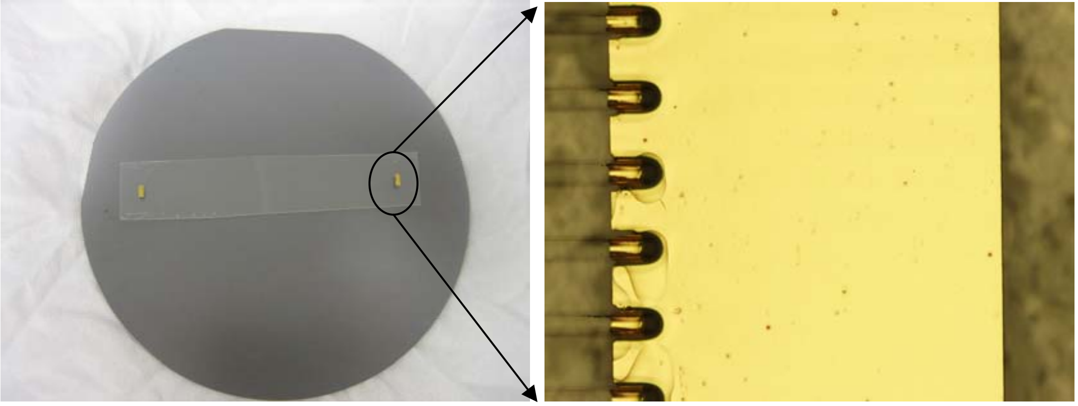

(a) (b)

Figure 3.11: (a) Optical picture of the fabricated waveguide array and (b) Au mirror near the 45° surfaces

3.5 OPTICAL TEST ON THE DEVICE

To observe the output pattern of the imprinted waveguide, a 635nm laser source was connected to a standard 9/125um SMF with a numerical aperture of 0.12. The other end of the fiber was fixed above the 45º micro-mirror region of the waveguide device. The channel length is 6.5cm. A CCD camera was connected through the microscope to export the output patterns onto the monitor. The input laser beam was shifted from 1st channel to the 12th channel in order to capture all the 12 output beam spots, which is shown in Figure 3.12(a). Optical tests based on the 850nm wavelength laser source were also carried out using an 850nm VCSEL diode with a 9/125um SMF pigtail (Figure 3.12(b)), which was surface normally coupled into the waveguide through the 45º micro-mirror. The output light intensity was measured by an 850nm photodetector which was fixed just above the output end of the waveguide array. The light propagation path is given in Figure 3.12(b).

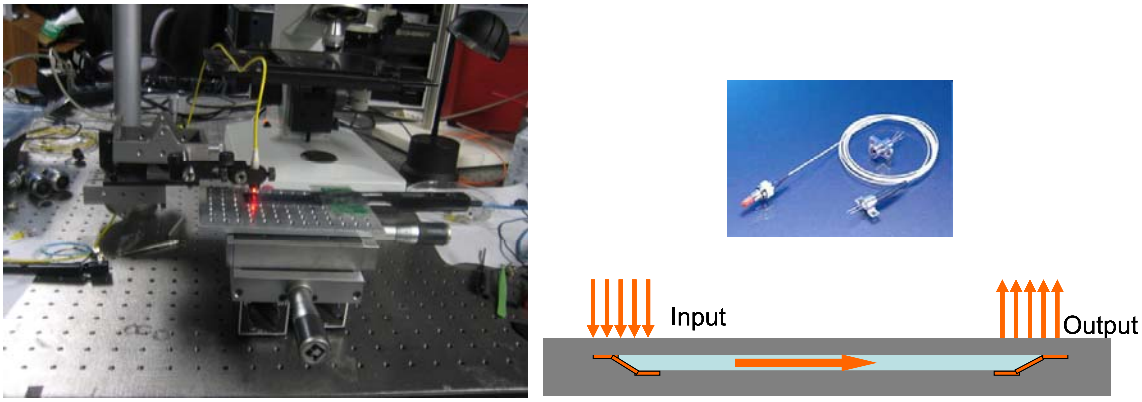

(a) (b)

Figure 3.12: (a) Actual setup of the optical test on the waveguide array devices (b) Pigtailed laser diode at 850nm and schematic of light propagation path

We measured the total insertion loss of each individual waveguide, calculated by the ratio of the total output power of each waveguide and the total input power of VCSEL diode at the SMF output end. The total insertion loss is around 4dB, with a deviation of 3dB for all channels. The loss difference between the channels was estimated to be due to some random factors in the imprinting process. The propagation loss of each channel was measured by a conventional cut-back method. First the waveguide was cleaved to be 4.0cm long. After polishing the output surface, the output power for each channel was measured. The waveguide was then cleaved to be 2.0cm long and polishing and measurements were carried out again. By comparing with the two groups of measurement results, we can calculate the propagation loss for each channel. The results are shown in Figure 3.13. Most channels have a propagation loss from 0.1 to 0.25dB/cm. The average value is 0.18dB/cm. Assuming the input and output micro-mirrors have the same coupling efficiency, the coupling losses are calculated to be between 1.3dB and 3.0dB (Figure 3.13(d)), which means the 45º TIR micro mirrors have a coupling efficiency of 75%. Compared with some reported values [4-5,11-12], further optimization of mold and device fabrication is need to achieve higher coupling efficiency, which will be discussed in the following chapters.

Channel Power(uW)	1	2	3	4	5	6	7	8	9	10	11	12
4cm long	650	510	940	840	330	840	330	320	520	860	450	330
2cm long	720	560	990	890	350	880	370	340	560	900	480	390
Propagation_loss (dB/cm)	0.22	0.20	0.11	0.13	0.13	0.15	0.25	0.13	0.16	0.15	0.14	0.36
Coupling_Loss (eB)	2.25	1.54	1.71	2.97	1.54	1.86	1.64	1.54	1.31	1.54	1.40	2.03

Table 3.2: Propagation loss and coupling loss measurements on the waveguide array

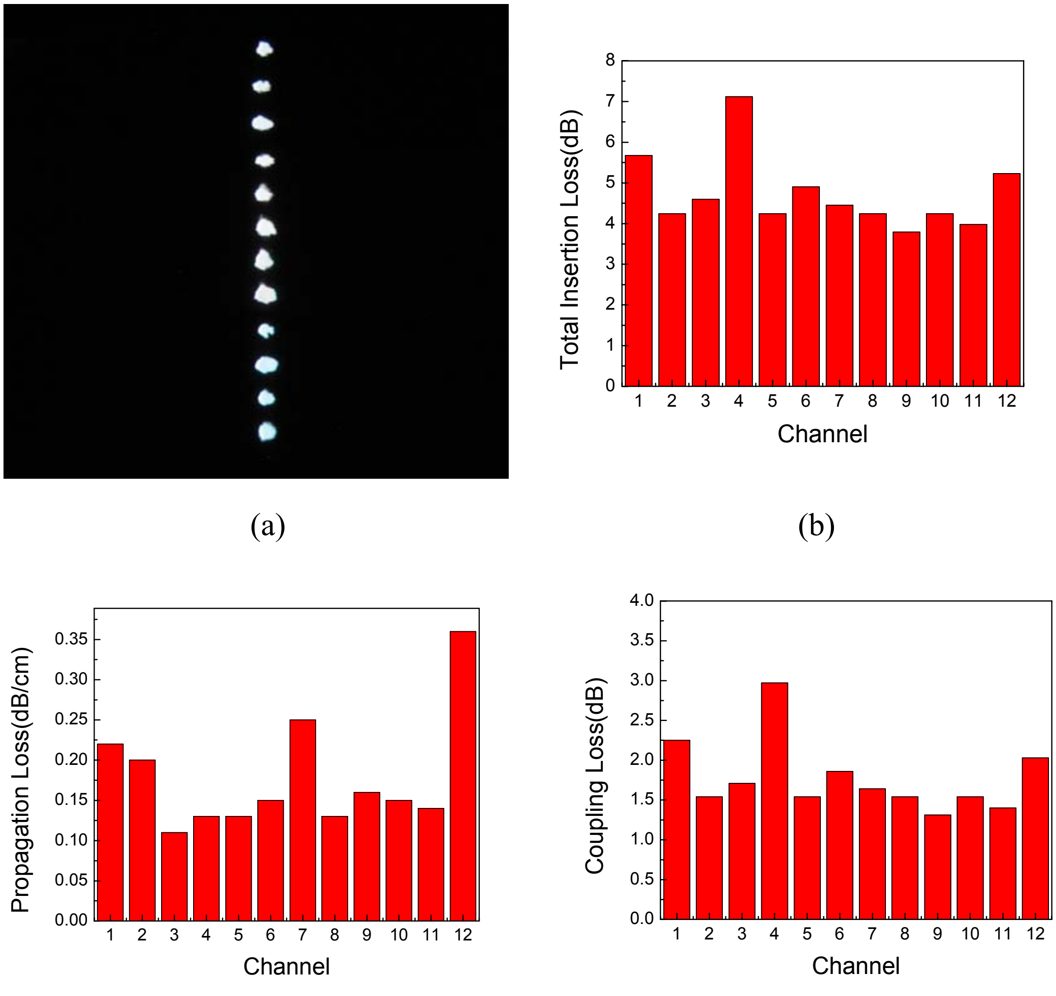

(a) (b)

(c) (d)

Figure 3.13: (a) Output image from screen (b) total insertion loss (c) measured propagation loss and (d) calculated coupling loss for 45º TIR micro-mirrors

3.6 CONCLUSION

In summary, we have successfully fabricated a SU-8 pre-mold for waveguide arrays with reversed 45º surfaces on both ends by tilted exposure under D.I. water. Waveguide metal molds with 45º surfaces were achieved by electroplating Ni into the SU-8 pre-mold trenches. SU-8 layer was removed after the electroplating process. The actual slant angle of the mold 45º surfaces is 44.5º. After obtaining the metal hard mold, a polymeric waveguide device based on the WIR30 series of UV curable photopolymers was obtained by a UV imprint technique. The total insertion loss at 850nm of an individual polymeric waveguide was around 4dB, and the average propagation loss is around 0.18dB/cm. The embedded 45º micro-mirrors have a coupling efficiency of 75%.

3.7 REFERENCES

[1] R. T. Chen, L. Lin, C. Choi, Y. Liu, B. Bihari, L. Wu, S. Tang, R. Wickman,B. Picor, M. K. Hibbs-Brenner, J. Bristow, and Y. S. Liu, "Fully Embedded Board level Guided-wave Optoelctronic Interconnects," Proc. IEEE, 88, 780-793 (2000).

[2] A. V. Krishnamoorthy, and D. A. B. Miller, "Scaling optoelectronic-VLSI circuits into the 21st century: A technology roadmap," IEEE J. Sel. Top. Quantum Electron. 2(1), 55–76 (2006).

[3] E. Mohanmmed, A. Alduino, T. Thomas, H. Braunisch, D. Lu, J. Heck, A. Liu, I. Young, B. Barnett, G. Vandentop, and R. Mooney, "Optical interconnect system integration for ultra-short-reach applications," J. Intel. Technol. 8(2), 115–127 (2004).

[4] L. Wang, X. Wang, W. Jiang, J. Choi, H. Bi, and R. T. Chen, "45° polymer-based total internal reflection coupling mirrors for fully embedded intraboard guided wave optical interconnects," Appl. Phys. Lett. 87(14), 141110 (2005).

[5] X. Wang, W. Jiang, L. Wang, H. Bi, and R. T. Chen, "Fully Embedded Board-Level Optical Interconnects From Waveguide Fabrication to Device Integration," J. Lightwave Technol. 26(2), 243–250 (2008).

[6] M. Hikita, R. Yoshimura, M. Usui, S. Tomaru, and S. Imamura, “Polymeric optical waveguides for optical interconnections,” Thin Solid Films, 331(1), 303–308 (1998).

[7] S. H. Hwang, W.-J. Lee, J. W. Lim, K. Y. Jung, K. S. Cha, and B. S. Rho, “Chip- and board-level optical interconnections using rigid flexible optical electrical printed circuit boards,” Opt. Express, 16(11), 8077–8083 (2008).

[8] C. Choi, L. Lin, Y. Liu, J. Choi, L. Wang, D. Haas, J. Magera, and R. T. Chen, “Flexible optical waveguide film fabrications and optoelectronic devices integration for fully embedded board-level optical interconnects,” J. Lightw. Technol., 22(9), 2168–2176 (2004).

[9] F. Wang, F. Liu, and A. Adibi, “45 Degree Polymer Micromirror Integration for Board-Level Three-Dimensional Optical Interconnects,” Opt. Express, 17(13), 10514-10521 (2009).

[10] W.J. Lee, S. H. Hwang, J. W. Lim, and B. S. Rho, “Polymeric Waveguide Film With Embedded Mirror for Multilayer Optical Circuits,” IEEE Photon. Technol. Lett. 21(1), 12-14 (2009).

[11] J. Van Erps, N.Hendrickx, C. Debaes, P. Van Daele, H. Thienpont, “Discrete Out-of-Plane Coupling Components for Printed Circuit Board-Level Optical Interconnections” IEEE Photon. Technol. Lett. 19(21), 1753-1755 (2007).

[12] N. Hendrickx,; J. Van Erps, E. Bosman, C. Debaes, H. Thienpont, P. Van Daele, “Embedded Micromirror Inserts for Optical Printed Circuit Boards,” IEEE Photon. Technol. Lett. 20(20), 1727-1729 (2008).

Chapter 4 *High speed test on the polymeric point-to-point waveguide*

4.1 INTRODUCTION

The demand for increasing bandwidth, driven by high-definition video sharing, network communications, and many other applications, draws significant research effort devoted to the development of high speed data communication for carrier networks and enterprise applications [1]. Challenges on electrical copper interconnects at high frequency make optical interconnect technologies a promising alternative to conventional electrical interconnects at different levels, such as rack-to-rack, board-to-board, and board level chip-to-chip interconnects [2-11]. Recent reported board level optical interconnects between two optomodules achieved an aggregated 160 Gb/s bidirectional data rate through 32 polymer waveguides operating at 10Gb/s [3]. Highly flexible polymeric waveguides for optical interconnects also have advantages in the application of next generation technology mobile devices, such as personal laptops, digital cameras, and foldable mobile phones [12]. These foldable mobile devices require not only high speed and error free data transmission but also highly flexible interconnects near the hinge area, where the waveguide frequently faces out-of-plane bending. The performance of polymeric waveguide under out-of-plane bending needs to be investigated in order to meet the high requirements of future mobile devices, such as smaller hinge structures and higher data transmission speeds.

In Chapter 3, we described in detail the fabrication of optical waveguide arrays with embedded 45° micro-mirrors on a flexible substrate using a metallic Ni hard mold, which was prepared by Ni electroplating method [4]. In this chapter, we investigated the out-of-plane bending effect on the waveguide array performance at different bending radii. The insertion losses of a 12-channel waveguide array were measured using a single-mode fiber (SMF) or multimode fiber (MMF) as the input. High speed optical tests at 10Gbps were carried out on the waveguide under out-of-plane bending conditions. By studying the insertion loss and high speed tests, the critical bending condition was found, and beyond this condition, the device performance will be degraded significantly. This is useful in future applications in terms of avoiding performance degradation caused by the out-of-plane bending effect.

4.2 SURFACE ROUGHNESS STUDY ON THE FABRICATED NI MOLD 45° SURFACES

The Ni waveguide hard mold was fabricated using a metal electroplating method. The fabrication details were described in chapter 3. First, a waveguide pre-mold was prepared using SU-8 2025, which was exposed under DI-water to create the 45° angles at the waveguide ends. Ni mold Electroplating was carried out with SU-8 pre-mold on the cathode. After electroplating, the SU-8 layer was removed by remover PG. In this way, the Ni hard mold with 45° surfaces was successfully achieved. A polymeric waveguide device was achieved by a UV imprint method using the fabricated Ni mold. In order to study the surface roughness, we used atomic force microscopy (AFM) to study the 45° surface at the waveguide end. Since the 45° surface is not parallel to the substrate surface, the mold was first cleaved using a Dicing Saw near the mold end region and was then placed on a right angle prism, making the 45° surfaces horizontal. Figure 4.1(a) is the SEM image of the 45° surface on the Ni mold. Figure 4.1(b) shows the setup for AFM scanning. The Ni mold was stuck on one side of a right angle prism, which made the 45° surfaces exactly horizontal. Figure 4.1(c) shows the AFM image of the Ni mold, which gives a surface roughness of approximately 70nm. During the UV imprinting process, a thin layer of AZ 5209 was coated on top of the waveguide mold as the release layer. This layer of photoresist reduces the surface roughness to 2nm (Figure 4.1(d)).

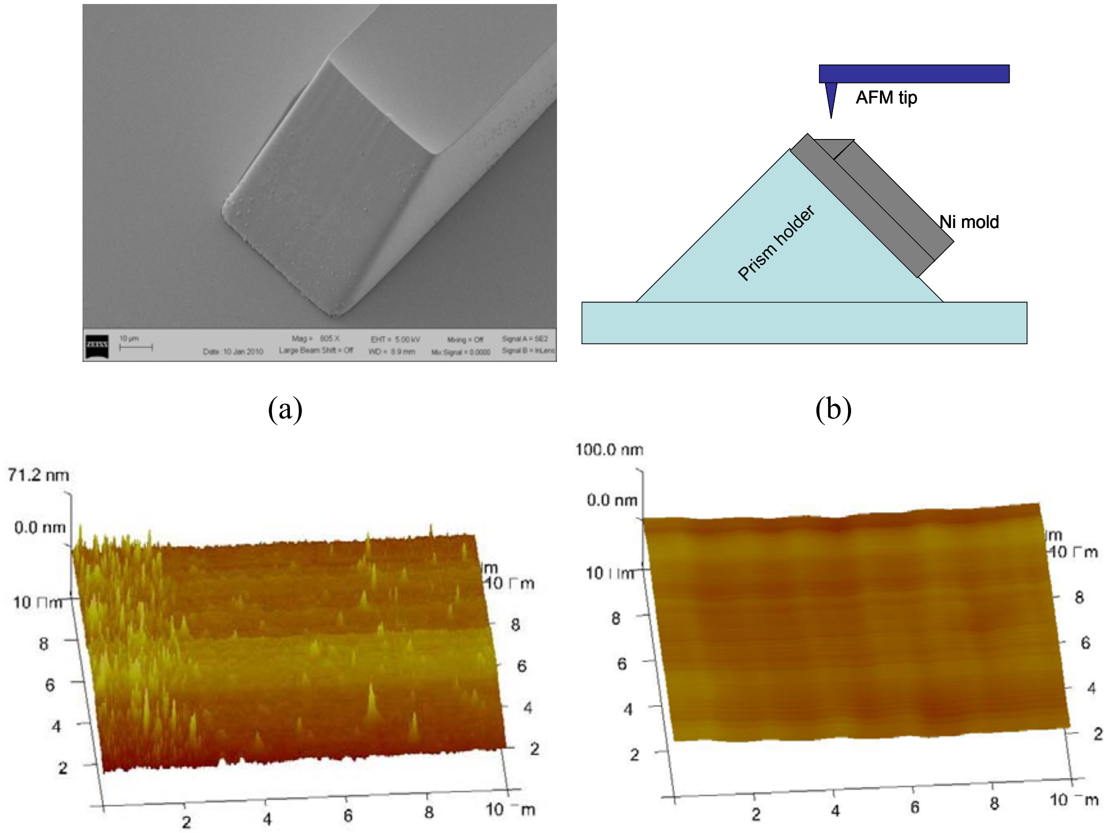

(a) (b)

(c) (d)

Figure 4.1: (a) Schematic setup for AFM scanning, inset is SEM image of Ni mold. (b) AFM image of the Ni hard mold without AZ5209 coating and (c) with AZ5209 coating

4.3 OPTIMIZATION OF CORE FILLING PROCESS

In the fabrication of a polymeric waveguide device based on UV imprint, the cladding and core materials are WIR30-450 and WIR30-470, respectively (purchased from ChemOptics Inc). It turns out that in the core filling step, the residue layer is very critical for the high optical test results, including insertion loss, crosstalk, and Q factors. In chapter 3, the core material was directly scratched away before UV curing, which may leave some residue outside the waveguide. Here we optimized the fabrication process for the core filling to guarantee the residue layer was completely removed. Figure 4.2 shows the optimized procedure for the core filling. First, WIR30-450 cladding was UV imprinted using the Ni hard mold followed by 200nm Au film coating by e-beam evaporation as TIR micro-mirrors. Core material WIR30-470 was then filled in the waveguide trenches. A clean, flat PDMS with a constant pressure was applied on top of the waveguide during the UV cure. This created a thin residue layer of WIR30-470 with a thickness of 2-4um. After UV cure, a 10um thick layer of AZ P4620 was patterned on the top of waveguide, followed by O_2 plasma etch for about 20min. After etching, the residue layer was completely removed, while the waveguide region was protected by the thick AZ film. The remaining AZ film was removed after plasma etch. Top cladding was spin-coated and UV cured to finish the device fabrication. Figure 4.3 shows the near field image of the fabricated waveguide at 635nm. We can see the residue layer was removed after O_2 plasma ashing. After core filling optimization, the crosstalk between the neighbor waveguides was measured to be around -38dB and -36dB by SMF and MMF as the input fiber, respectively.

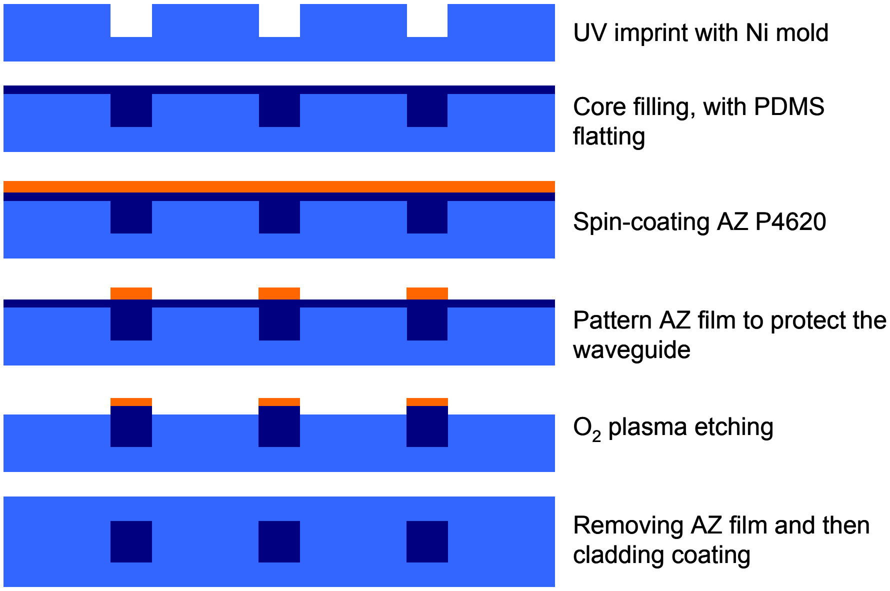

Figure 4.2: Schematic of the core filling optimization process

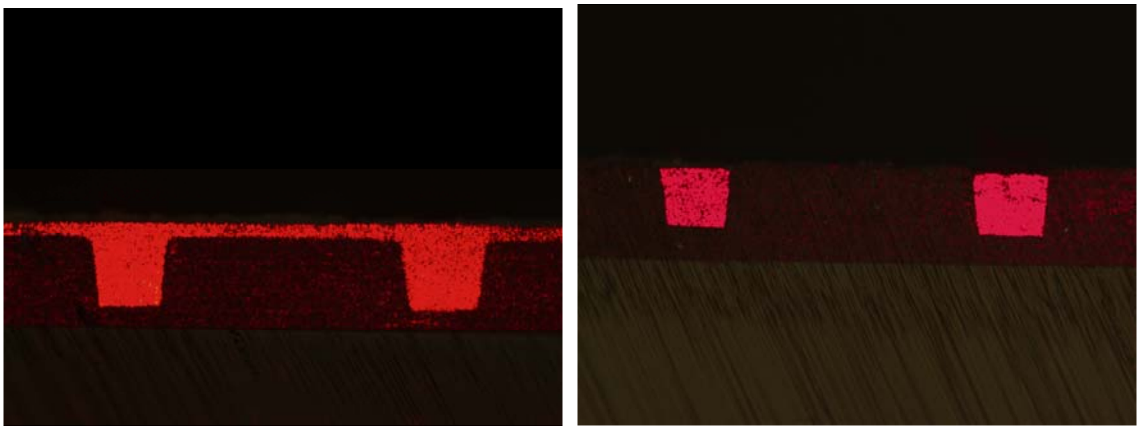

(a) (b)

Figure 4.3: Near field image of the fabricated waveguide at 635nm (a) with residual layer (b) without residual layer

4.4 INSERTION LOSS MEASUREMENT ON THE BENT WAVEGUIDE

A polymeric waveguide array device was achieved by a UV imprint method using the electroplated Ni mold. The fabrication details were described in reference [4]. The waveguide cladding and core materials are WIR30-450 and WIR30-470, respectively, purchased from ChemOptics Inc. The corresponding refractive indices of the waveguide cladding and core are 1.45 and 1.47 at 850nm, respectively. The flexible TOPAS substrate is TEONEX film from Dupont Teijin Films Inc. The fabricated waveguide has a 50μm×50μm core, 15μm thick top and bottom claddings, and 4.8cm length. One of the advantages of our waveguide array is that the whole device can be bent out-of-plane due to its flexible substrate. The performance degradation caused by the bending merits further study. Here we carried out a series of insertion loss measurements on the bent waveguide at different bending radii at 850nm wavelength. Figure 4.4 shows the schematic setup for the bending test. The device was fixed onto the curved surface with bending radii of 61.1mm, 30.6mm, 20.4mm, 15.3mm, 12.2mm, 10.2mm, 9.2mm, 7.6mm and 5.0mm, respectively. The corresponding bending angles are 45°, 90° and 135° for 61.1mm, 30.6mm and 20.4mm, respectively, limited by the waveguide length. The bending angles for the radii at 15.3mm or less are all 180°. The performance without any bending was also measured for comparison. A 1 meter long 9/125μm single-mode fiber (SMF) and a 50/125μm multi-mode fiber (MMF) were used to couple the light into the waveguide. A photodetector was placed at the output end to measure the output light intensity.

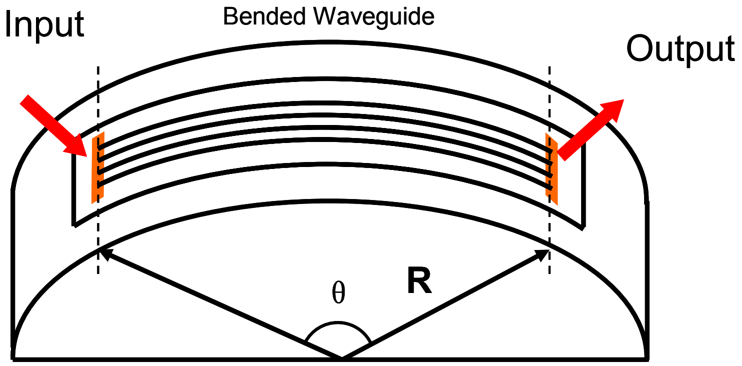

Figure 4.4: Schematic view of the bent waveguide array on a semi-column surface

The insertion loss measurement results of the waveguide array at the flat condition and at selected bending radii of 61.1mm, 20.4mm, 10.2mm, 9.0mm, and 5.0mm were shown in Figure 4.5(a)-(f). In these figures, red and green bars correspond to the losses measured by SMF and MMF, respectively. SMF has a much smaller core diameter and higher coupling efficiency than MMF. Thusly, the loss measured by SMF is smaller than that measured by MMF. From these figures we see that as the bending radius decreases from flat condition to 5.0mm, the insertion loss increases due to the bending of the whole device. In order to wipe off the random errors in the measurement and find out the bending effect, we calculated the average insertion loss of 12 channels at each bending radius. Figure 4.6(a) gives the calculation results for all 9 different bending radii. The points on the right hand most side correspond to the flat condition. From the flat condition to a 5mm bending radius, the average insertion loss increases from 3.4dB to 7.7dB and from 5.5dB to 7.9dB for SMF and MMF, respectively. The total degradation caused by bending is around 4.3dB and 2.4dB for SMF and MMF, respectively. From Figure 4.6(a), we can see the insertion loss increases significantly only when the bending radius is below 9.0mm. The measured bending loss is a little higher than the simulation results of similar curved waveguide [13]. The other phenomena of note is that as the bending radius decreases, the average insertion loss difference measured between SMF and MMF decreases from 2.0dB to 0.2dB(Figure 4.6(b)). We believe that as the bending radius decreases, the loss due to bending becomes dominant over the coupling loss or propagation loss, and bending loss is independent of SMF or MMF.

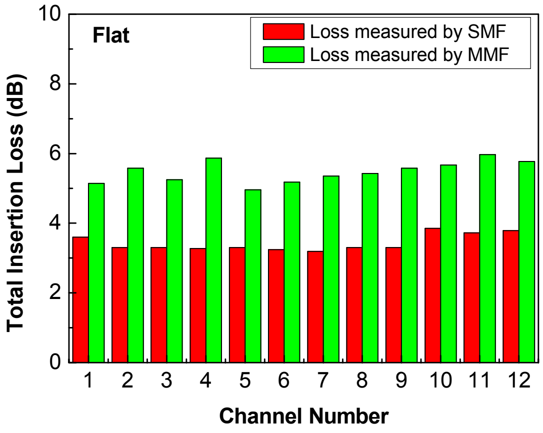

(a)

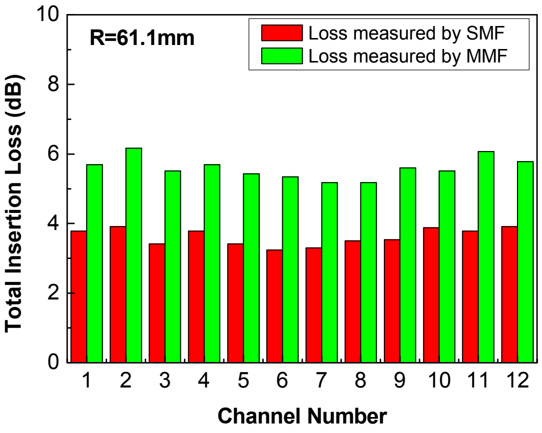

(b)

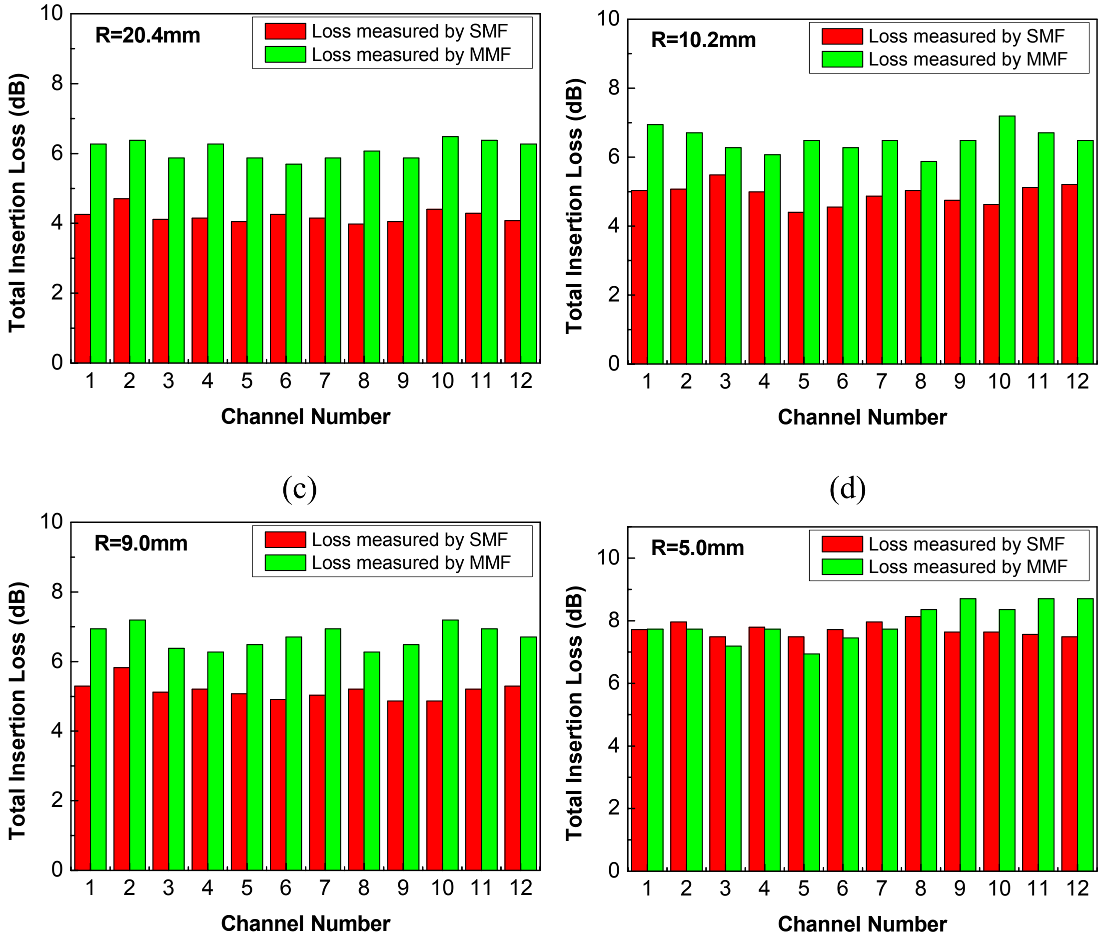

(c)

(d)

(e)

(f)

Figure 4.5: Insertion loss measurements for 12 channels at different bending radius (a)flat condition, (b)61.1mm, (c)20.4mm, (d)10.2mm, (e)9.2mm and (f)5.0mm. Red and green bars are for SMF and MMF coupling, respectively

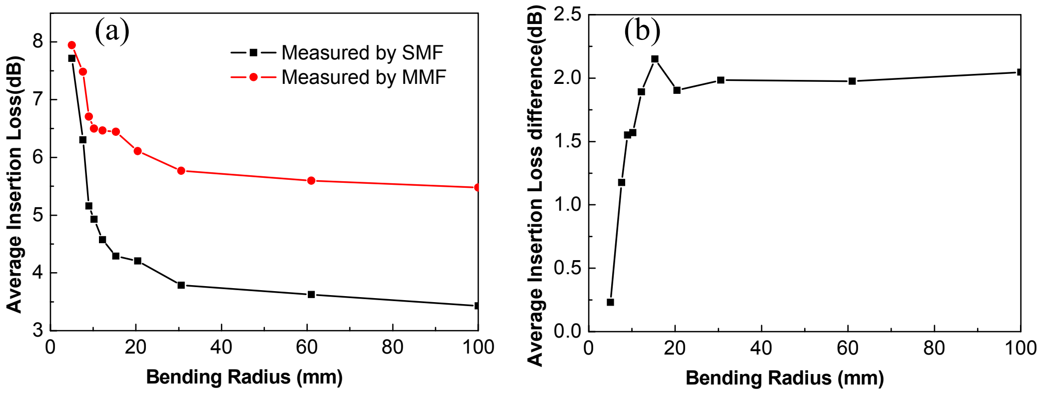

(a) (b)

Figure 4.6: Bending radius dependence of (a) average insertion loss measured by SMF coupling (black) and MMF coupling (red) (b) average insertion loss difference measured between SMF and MMF

4.5 HIGH SPEED OPTICAL TEST ON THE WAVEGUIDE UNDER BENDING

In order to study the performance degradation of the waveguide array under bending, optical test at 850nm was carried out on the fabricated device. VCSELs and photodiodes (PD) operating at 850nm were purchased from Finisar Co., which meet the performance requirements for 10Gbps data communication over multimode optical fibers. The optical assembly was designed to interface either 50µm or 62.5µm multimode fiber. The schematic setup (Figure 4.7(a)) and actual setup (Figure 4.7(b)) of the high speed optical test are shown. The differential pulse signal and the DC bias were connected to an evaluation board by two high frequency bias tees, on which the 10Gbps VCSEL was mounted, shown in Figure 4.7(c). The combined bias was used to drive the VCSEL to emit modulated light intensity. A multi-meter was connected to monitor the drive current for the VCSELs. The modulated optical signal from the VCSEL was coupled into the waveguide by 45° TIR micro-mirrors through a 50/125µm multimode fiber. After propagation through the waveguide, the light was coupled out by the surface-normal 45° TIR micro-mirrors into the 62.5/125 μm multimode fiber. Typical DC bias for the VCSEL was about 1.90V with a current 5.8mA, which produces an emitting power of 920μW at 850nm. The random signal level is ±0.3V. The other end of the MMF was connected to the high speed photodiode operating at 850nm, which was mounted on another evaluation board, as shown in Figure 4.7(d). The signal response from the photodiode was connected to the oscilloscope for eye diagram observation. The DC bias applied to the photodiode for efficient conversion is 3.3V. The modulation speed of the VCSEL signal can be controlled by a signal generator through PC software, which has a range from 1Gps to 10Gps.

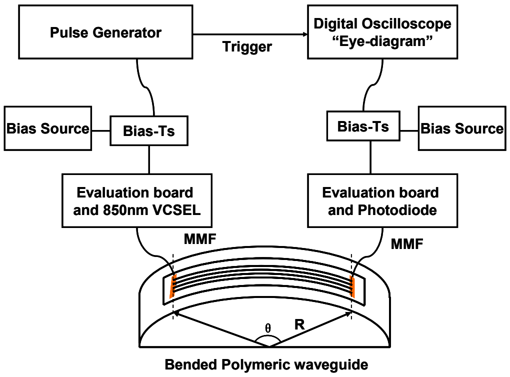

(a)

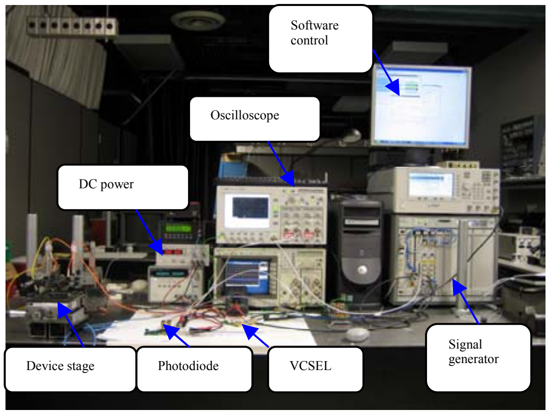

(b)

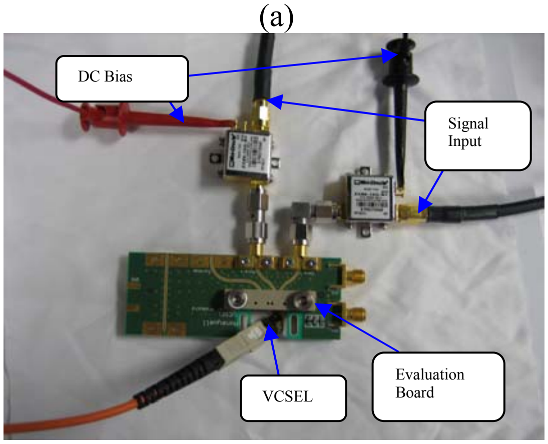

(a)

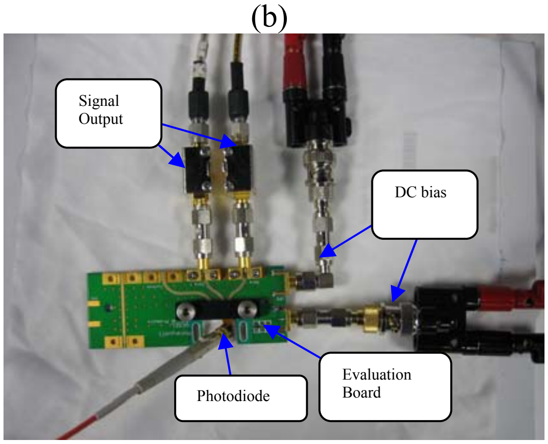

(b)

Figure 4.7: (a) Schematic and (b) actual view of the high speed test setup for the bent waveguide. (c) VCSEL mounted on an evaluation board, with DC bias and signal input connections. (d) Photodiode mounted on an evaluation board, with DC bias and signal output connections

At the flat (0°) condition, we measured the eye-diagrams with frequencies from 1Gbps to 10Gbps. All eye-diagrams are wide open from 1Gbps to 10Gbps. The eye-diagrams at different bending curvatures were also successfully obtained. Figures 4.8(a)-(f) show the selected eye-diagrams as the bending radius decreases from the flat condition to 5.0mm. The signal-to-noise ratio or Q factor was also measured at each bending radius. After achieving the Q factors, we calculated the bit error rate (BER). The relation between the Q-factor and BER is given by: $BER = (1/2)\times erfc(Q/\sqrt{2})$ [6], if one assumes the presence of Gaussian distributed noises.

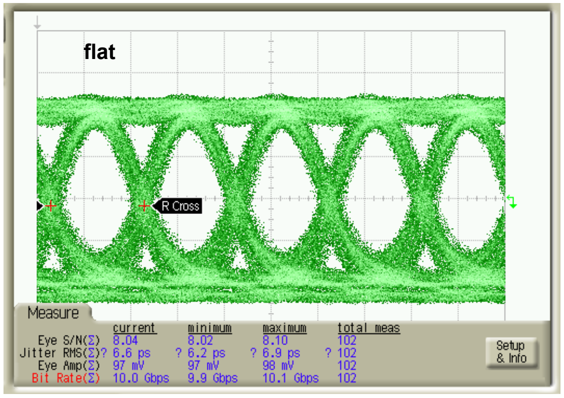

```
                   current     minimum     maximum     total meas
      Eye S/N(Σ)   8.04        8.02        8.10        102
  Jitter RMS(Σ)?   6.6 ps    ? 6.2 ps    ? 6.9 ps    ? 102
      Eye Amp(Σ)   97 mV       97 mV       98 mV       102
     Bit Rate(Σ)   10.0 Gbps   9.9 Gbps    10.1 Gbps   102
```

(a)

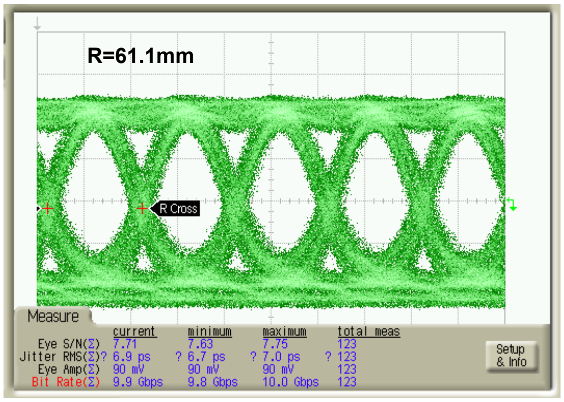

```
                   current     minimum     maximum     total meas
      Eye S/N(Σ)   7.71        7.63        7.75        123
  Jitter RMS(Σ)?   6.9 ps    ? 6.7 ps    ? 7.0 ps    ? 123
      Eye Amp(Σ)   90 mV       90 mV       90 mV       123
     Bit Rate(Σ)   9.9 Gbps    9.8 Gbps    10.0 Gbps   123
```

(b)

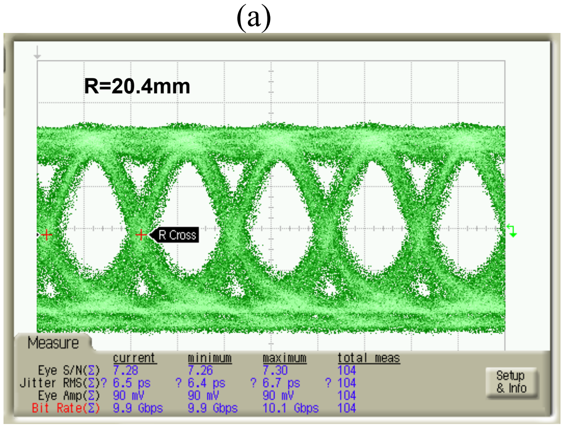

```
                   current     minimum     maximum     total meas
      Eye S/N(Σ)   7.28        7.26        7.30        104
  Jitter RMS(Σ)?   6.5 ps    ? 6.4 ps    ? 6.7 ps    ? 104
      Eye Amp(Σ)   90 mV       90 mV       90 mV       104
     Bit Rate(Σ)   9.9 Gbps    9.9 Gbps    10.1 Gbps   104
```

(c)

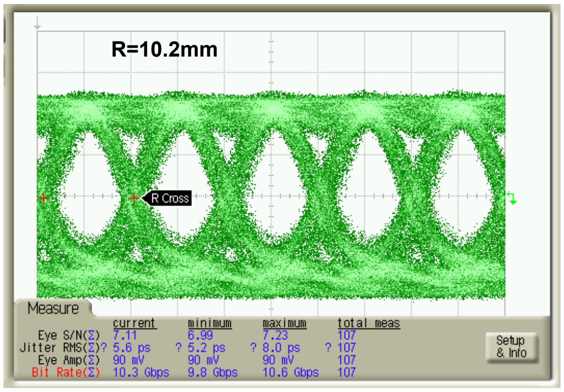

```
                   current     minimum     maximum     total meas
      Eye S/N(Σ)   7.11        6.99        7.23        107
  Jitter RMS(Σ)?   5.6 ps    ? 5.2 ps    ? 8.0 ps    ? 107
      Eye Amp(Σ)   90 mV       90 mV       90 mV       107
     Bit Rate(Σ)   10.3 Gbps   9.8 Gbps    10.6 Gbps   107
```

(d)

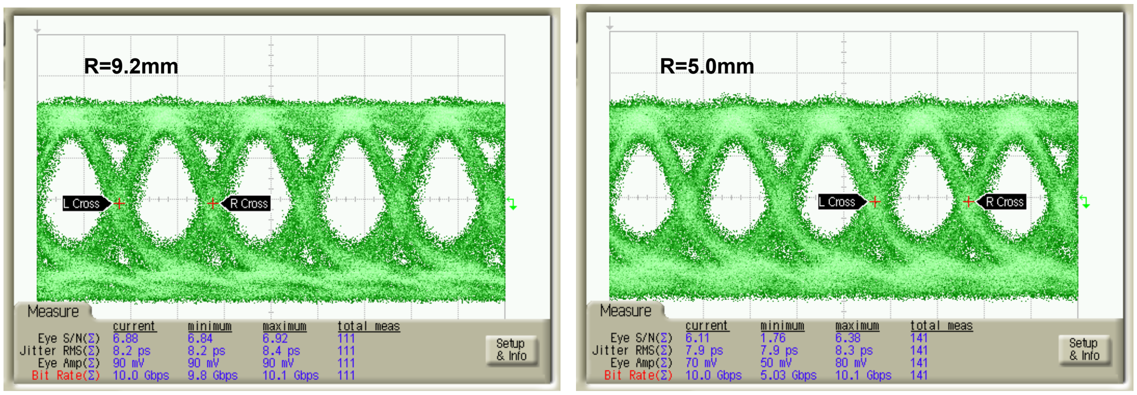

	current	minimum	maximum	total meas
Eye S/N(Σ)	6.88	6.84	6.92	111
Jitter RMS(Σ)	8.2 ps	8.2 ps	8.4 ps	111
Eye Amp(Σ)	90 mV	90 mV	90 mV	111
Bit Rate(Σ)	10.0 Gbps	9.8 Gbps	10.1 Gbps	111

	current	minimum	maximum	total meas
Eye S/N(Σ)	6.11	1.76	6.38	141
Jitter RMS(Σ)	7.9 ps	7.9 ps	8.3 ps	141
Eye Amp(Σ)	70 mV	50 mV	80 mV	141
Bit Rate(Σ)	10.0 Gbps	5.03 Gbps	10.1 Gbps	141

(e) (f)

Figure 4.8: Selected eye-diagrams at 10Gbps with bending radii at (a)flat condition, (b)61.1mm, (c)20.4mm, (d)10.2mm and (e)9.2mm, (f)5.0mm

The frequency dependence of Q factors and calculated bit error rate (BER) from 1Gbps to 10Gbps at the 0° bending condition are shown in Figure 4.9(a). As the bit rate increases from 1Gbps to 10Gbps, the Q factor decreases from 14.4 to 8.0. Q factors at 7Gbps and 8Gpbs increase slightly due to the photodiode response properties. The calculated BER increases from around 10^{-45} at 1Gbps to 10^{-16} at 10Gbps. Figure 4.9(b) shows the Q factor's dependence on bending radius and the calculated BER at 10Gbps. From the flat condition to a 5mm bending radius, the Q factor decreases from 8.0 to 6.1 and the BER increases from 10^{-16} to around 10^{-10}. The degradations of Q factor and BER are expected due to the increasing insertion loss of the bending waveguide. From the calculation, in order to maintain a BER less than 10^{-12}, the bending radius should be above 9.0mm. This is consistent with our insertion loss measurement results under bending conditions. From the application point of view, 9.0mm bending radius is small enough for some large devices, such as personal laptops. For smaller devices, such as personal mobile phones, further work is needed to reduce the critical bending radius to less than 5.0mm with a BER of 10^{-12} or less at 10Gbps, such as using lower propagation loss, higher core and cladding index contrast polymer materials, more flexible substrate, higher efficient coupling techniques, and optimizing the fabrication process.

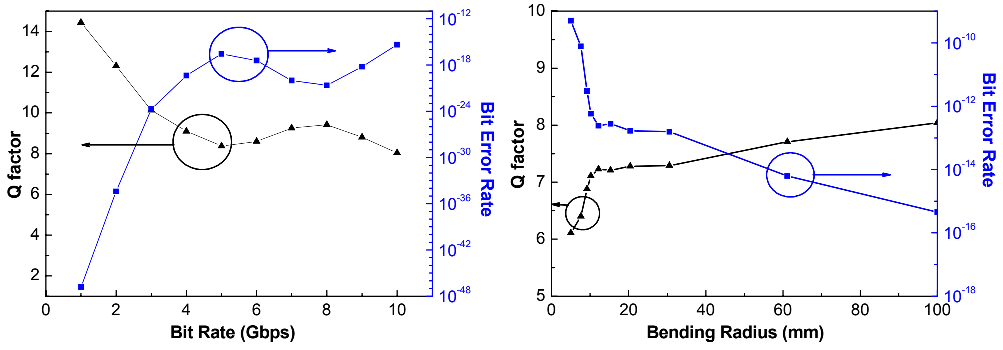

(a) (b)

Figure 4.9: Q factor and Bit Error Rate(BER) dependence on (a) the bit rate without bending and (b) the bending radius

4.6 CONCLUSION

We have successfully optimized the core filling process for the waveguide array fabrication and measured the bending effect on the insertion losses and the high speed performance of the waveguide array, which was fabricated using a metallic hard mold. As bending radius decreases, the average insertion loss at 850nm of the 12 channels increases both for SMF and MMF. Eye diagrams with 10Gbps random signals at different bending radius were also successfully achieved. The signal-to-noise ratios and Q factors were obtained at each bending condition. The bit-error-rate (BER) was calculated by assuming the presence of Gaussian distributed noise at each frequency.

4.7 REFERENCES

[1] O. Ishida, and T. Wang, “100 gigabit Ethernet transport,” IEEE Commun. Mag. 48, S4 - S4, (2010).

[2] R. T. Chen, L. Lin, C. Choi, Y. Liu, B. Bihari, L. Wu, S. Tang, R. Wickman, B. Picor, M. K. Hibbs-Brenner, J. Bristow, and Y. S. Liu, “Fully Embedded Board level Guided-wave Optoelctronic Interconnects,” Proc. IEEE, 88, 780-793 (2000).

[3] F. E. Doany, C. L. Schow, C. W. Baks, D. M. Kuchta, P. Pepeljugoski, L. Schares, R. Budd, F. Libsch, R. Dangel, F. Horst, B. J. Offrein, and J. A. Kash, “160 Gb/s Bidirectional Polymer-Waveguide Board-Level Optical Interconnects Using CMOS-Based Transceivers,” Advanced Packaging, IEEE Transactions on, 32(2),345-359 (2009).

[4] X. Y. Dou, X. L Wang, H. Y. Huang, X. H. Lin, D. Ding, D. Z. Pan, and R. T. Chen, “Polymeric waveguides with embedded micro-mirrors formed by Metallic Hard Mold,” Opt. Express 18, 378-385 (2010).

[5] L. Wang, X. Wang, W. Jiang, J. Choi, H. Bi, and R. T. Chen, “45° polymer-based total internal reflection coupling mirrors for fully embedded intraboard guided wave optical interconnects,” Appl. Phys. Lett. 87(14), 141110 (2005).

[6] X. Wang, W. Jiang, L. Wang, H. Bi, and R. T. Chen, “Fully Embedded Board-Level Optical Interconnects From Waveguide Fabrication to Device Integration,” J. Lightwave Technol. 26(2), 243-250 (2008).

[7] M. Hikita, R. Yoshimura, M. Usui, S. Tomaru, and S. Imamura, “Polymeric optical waveguides for optical interconnections,” Thin Solid Films, 331(1), 303-308 (1998).

[8] F. Wang, F. Liu, and A. Adibi, “45 Degree Polymer Micromirror Integration for Board-Level Three-Dimensional Optical Interconnects,” Opt. Express, 17(13), 10514-10521 (2009).

[9] W. J. Lee, S. H. Hwang, J. W. Lim, and B. S. Rho, “Polymeric Waveguide Film

With Embedded Mirror for Multilayer Optical Circuits," IEEE Photon. Technol. Lett. 21(1), 12-14 (2009).

[10] J. Van Erps, N.Hendrickx, C. Debaes, P. Van Daele, and H. Thienpont, "Discrete Out-of-Plane Coupling Components for Printed Circuit Board-Level Optical Interconnections" IEEE Photon. Technol. Lett. 19(21), 1753-1755 (2007).

[11] N. Hendrickx, J. Van Erps, E. Bosman, C. Debaes, H. Thienpont, and P. Van Daele, "Embedded Micromirror Inserts for Optical Printed Circuit Boards," IEEE Photon. Technol. Lett. 20(20), 1727-1729 (2008).

[12] B. S. Rho, W. J. Lee, J. W. Lim, G. W. Kim, C. H. Cho, and S. H. Hwang, "High-reliability flexible optical printed circuit board for opto-electric interconnections," Opt. Eng. 48(1), 015401 (2009).

[13] B. Howley, X. L. Wang, Y. H. Chen, and Ray T. Chen, "Experimental evaluation of curved polymer waveguides with air trenches and offsets," J. Appl. Phys. 100, 023114 (2006).

Chapter 5 *Polymeric optical bus waveguide with embedded 45° micro-mirrors*

5.1 INTRODUCTION

In electrical interconnects, the point-to-point topology replaced the shared-bus topology because of its bandwidth. However, wiring congestion is the adverse consequence of this transition, because in order to route all memory modules to the central switch, the boards in a high performance computing system currently tend to use more than 50 wiring layers, and more than 700 signal pins are required for one board edge connector, which needs as much as 100 pounds of insertion force to seat [1]. Optical bus architecture greatly mitigates wiring congestion while still allowing for multiple daughter boards to share a common data channel to transfer information at a high speed simultaneously [2-3]. There is no loading effect of optics analogous to driving capacitance in an electronic circuit, which means the signal propagation speed is a constant value of 0.6c of polymer waveguide regardless of the presence of the receiver boards. Conversely, for an electrical bus, an unloaded PC board trace has a typical signal propagation speed of 0.6c to a fully loaded bus line of 0.2c. Higher speed as well as a much more stable signal round-trip time can be obtained by replacing the electrical bus with the proposed optical bus. Compared with point to point interconnect, bus based interconnects represent the most complicated interconnect structure with full interconnectivity and broadcasting nature [4-5]. Fiber based optical interconnects, which is intrinsically for point-to-point interconnection, fails to provide the desired optical bus architecture. Here we designed the optical bus based interconnected system with 3-to-3, 4-to-4, or 8-to-8 nodes, which have the advantages of enhancing the bandwidth, increasing the reliability, providing package compatibility, and reducing fabrication cost.

5.2 DESIGN AND SIMULATION OF THE 3-TO-3 OPTICAL BUS PRE-MOLD

A planar view of the 3-to-3 optical bus architecture is shown in Figure 5.1. It consists of two parallel optical buses with 50um width, which can transmit optical signals toward two opposite directions. Optical signals, either from laser diodes (LD) of the master unit or the slave units, will be transmitted bi-directionally through two connected unidirectional couplers. The detectors (D) of either the master unit or the slave units are also capable of receiving optical signals from both directions, benefited from the two unidirectional couplers connected to them. The two parallel optical buses in conjunction with unidirectional couplers ensure the completely non-blocking interconnection among any existing units, without any wiring congestion. The laser diodes and the photodetectors are located either on the associated cardboards or the backplane itself. The intra-plane interconnection, i.e., from the laser diodes and photodectors to the waveguides, are established through surface normal micro-mirrors. The optical waves can be either coupled into and out of the optical bus by two opposite-placed 45° micro-mirrors, or by one micro-mirror equally split by a Y-branch coupler.

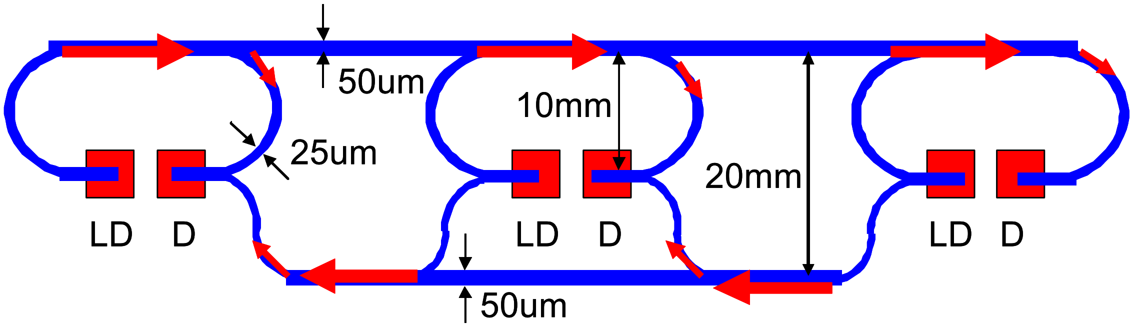

Figure 5.1: Schematic view of the 3x3 optical bus architecture

In the 3x3 optical bus waveguide architecture, there are 2 Y-splitters/combiners with a 1:1 power ratio, 2 Y-splitters/combiners with a 1:2 power ratio, 4 bus-branch splitters/combiners with a 1:2 power ratio, 2 bus-branch splitters/combiners with a 1:1 power ratio. The power ratio distribution in the design is shown in Figure 5.2. The red and black numbers are for the out-going splitter and the incoming combiner, respectively.

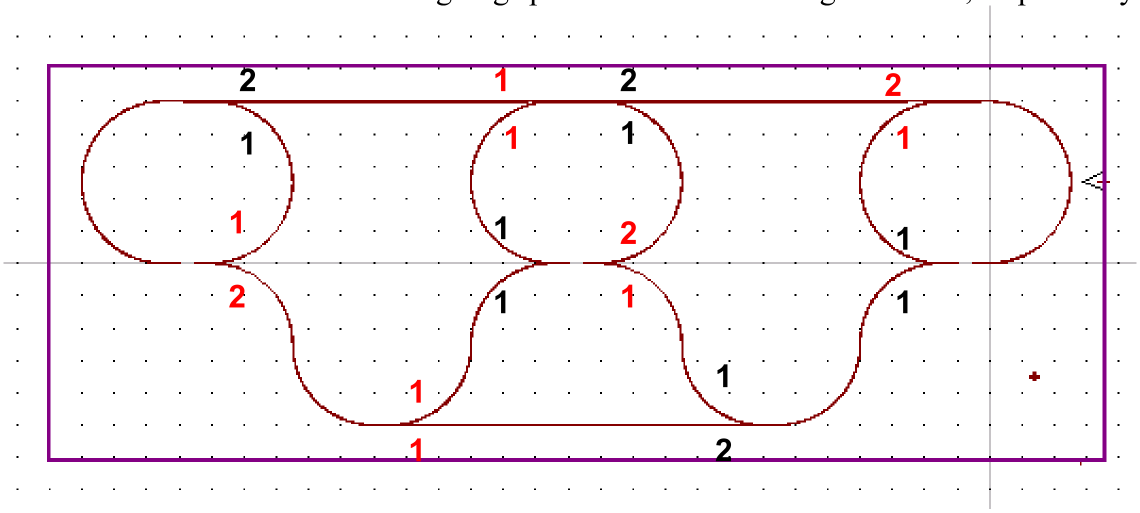

Figure 5.2: Power ratios at the splitters/combiners. Red and black numbers are for outgoing and incoming beams, respectively

We use commercially available software, Rsoft, to simulate the optical beam power distribution within the Y-splitters and bus-branch splitters. The layout is shown in Figure 5.3. All of the Y-splitters have a width of 50µm. The Y-splitter branches with a 1:1 ratio have a width of 25µm with a splitting angle of 11.5°. The Y-splitter branch with a 1:2 ratio has branch widths of 28µm and 50µm with a splitting angle of 8.7°. The bus-branch splitter with a 1:1 ratio has branch widths of 50µm and 32µm with a splitting angle of 7.3°. The bus-branch splitter with a 1:2 ratio has branch widths of 48µm and 50µm with a splitting angle of 8.2°. The power ratios, widths, and splitting angles of Y-splitters and bus-branch splitters are listed in Table 5.1.

	Power ratio	Widths	Splitting angle

Y-splitter	1:1	25µm/25µm	11.5°
Y-splitter	1:2	28µm/50µm	8.7°
Bus-branch splitter	1:1	50µm/32µm	7.3°
Bus-branch splitter	1:2	48µm/50µm	8.2°

Table 5.1: Power ratios, widths and splitting angles of Y-splitters and bus-branch splitters

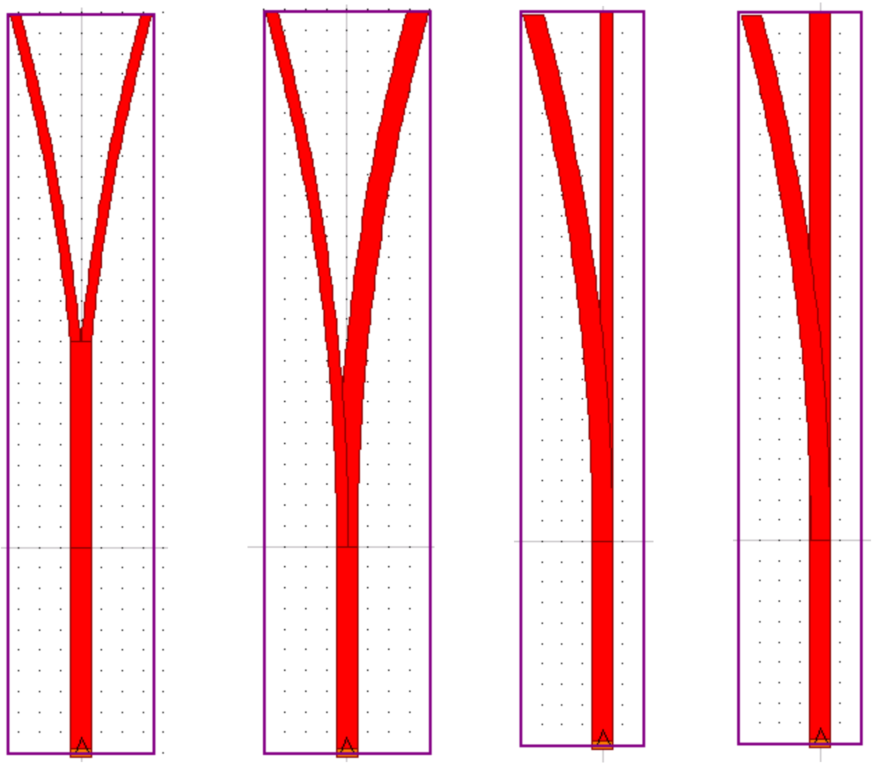

(a) (b) (c) (d)

Figure 5.3: Rsoft layout of (a) 1:1 ratio Y-splitter (b) 1:2 ratio Y-splitter (c) 1:1 bus-branch splitter (d) 1:2 bus-branch splitter

In order to simulate the power distribution, we used the BeamPROP, a Rsoft software package, to calculate the beam propagation properties within the Y-splitters and bus-branch splitters. The wavelength we used in the simulation is 850nm, corresponding to the VCSEL wavelength we used in optical tests. The BeamPROP simulation results are shown in Figure 5.4. A power monitor was placed in each branch, and the power percentage in each branch is shown on the right hand side in each simulation figure. Figure 5.4(a) gives the simulation result of the Y-splitter with a 25um branch width. This Y-splitter functions as incoming waveguides which connected to the photodetectors. Figure 5.4(b) shows the simulation result of the Y-splitter with a 1:2 power splitting ratio. The power percentages in the two branches are 31% and 62%, respectively. Total power of the two branches is 93% of the incoming beam power. The simulation results of bus-branch splitter with a 1:1 power splitting ratio is shown in Figure 5.4(c). The power percentages are 47% and 48%, respectively, which has a total 5% power loss. As for the bus-branch splitter with a 1:2 power splitting ratio, the power percentages are 32% and 66%, which has a total power of 98% of the incoming beam. A summary of the simulation results is given in Table 5.2.

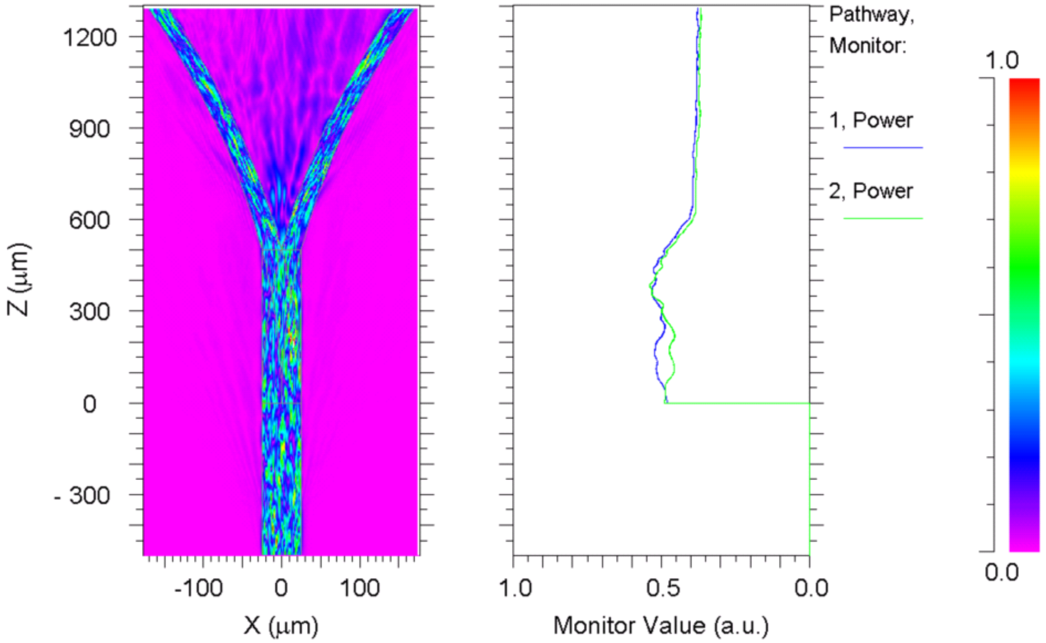

(a)

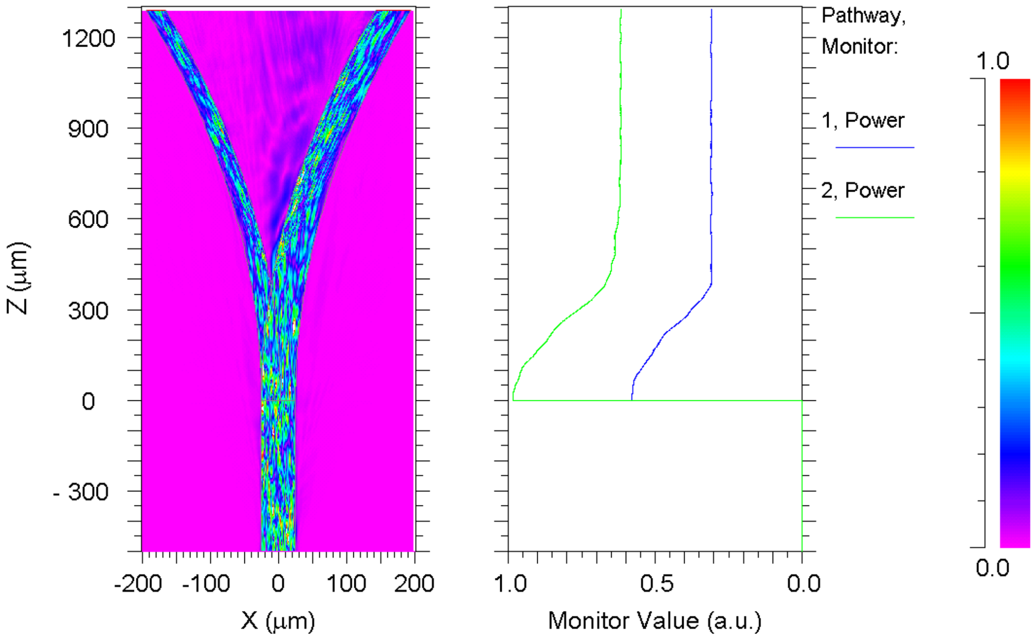
1200
900
600
300
0
- 300
Z (μm)
-200
-100
0
100
200
X (μm)
1.0
0.5
0.0
Monitor Value (a.u.)
Pathway,
Monitor:
1, Power
2, Power
1.0
0.0

(b)

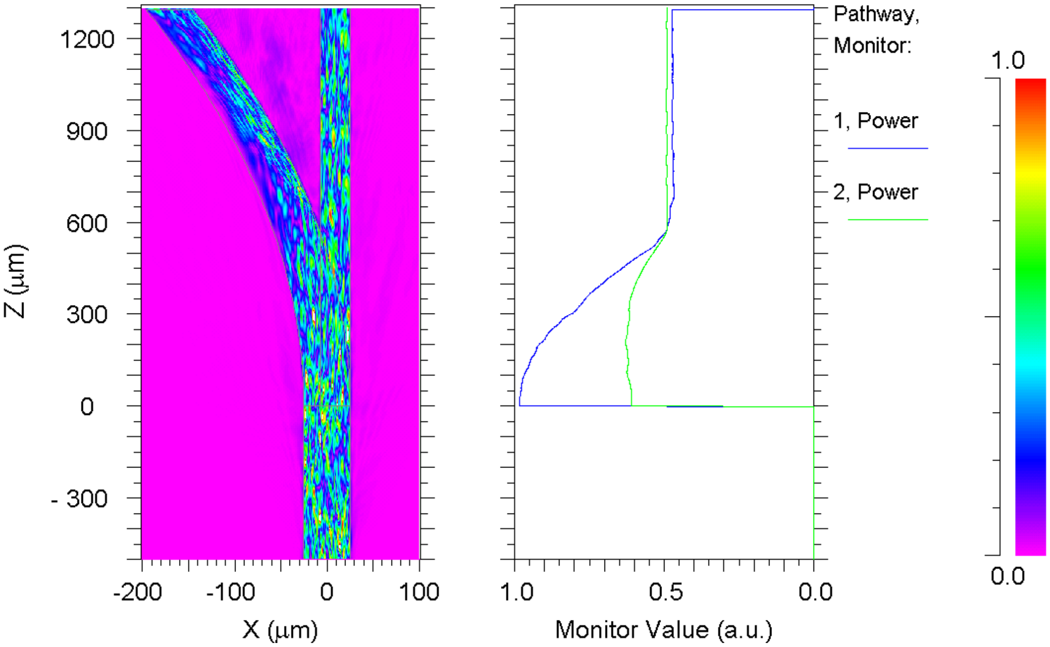
1200
900
600
300
0
- 300
Z (μm)
-200
-100
0
100
X (μm)
1.0
0.5
0.0
Monitor Value (a.u.)
Pathway,
Monitor:
1, Power
2, Power
1.0
0.0

(c)

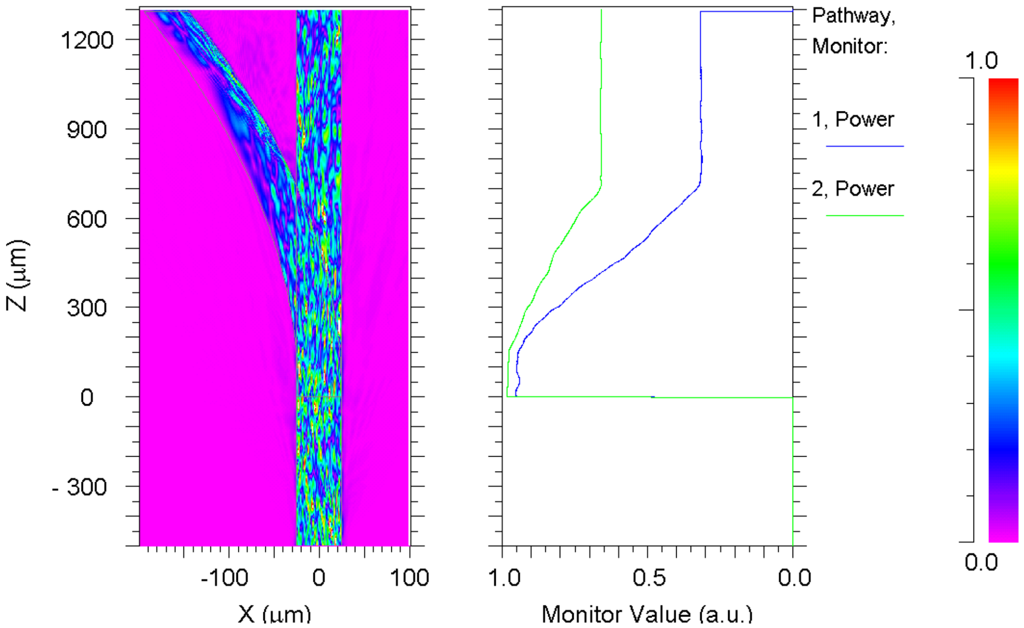

(d)

Figure 5.4: BeamPROP simulation of the beam propagation within the Y-splitter and bus-branch splitters at 850nm. (a) Y-splitter with 1:1 ratio, (b) Y-splitter with 1:2 ratio,(c) Bus-branch splitter with 1:1 ratio,(d) Bus-branch splitter with 1:2 ratio

	Power ratio	Simulated power splitting percentage (%)	Loss at the splitters
Y-splitter	1:1	45/45	10%
Y-splitter	1:2	31/62	7%
Bus-branch splitter	1:1	47/48	5%
Bus-branch splitter	1:2	32/66	2%

Table 5.2: Simulation results of power splitting percentage at Y-splitters and bus-branch splitters

5.3 PREPARATION OF OPTICAL BUS WAVEGUIDE PRE-MOLD FOR ELECTROPLATING

The fabrication process for the bidirectional bus structure is completely compatible with parallel point-to-point optical interconnects [6]. First, photopolymer SU-8 based bus pre-mold with 45° surfaces was achieved by tilted exposure under DI-water method, then certain thickness metal Ni was electroplated into the SU-8 defined trenches. After that, SU-8 layer was removed and a metal bus mold was achieved. Using the metal bus mold, a polymeric optical bus device was formed by UV imprint method using UV curable polymer WIR-30 series.

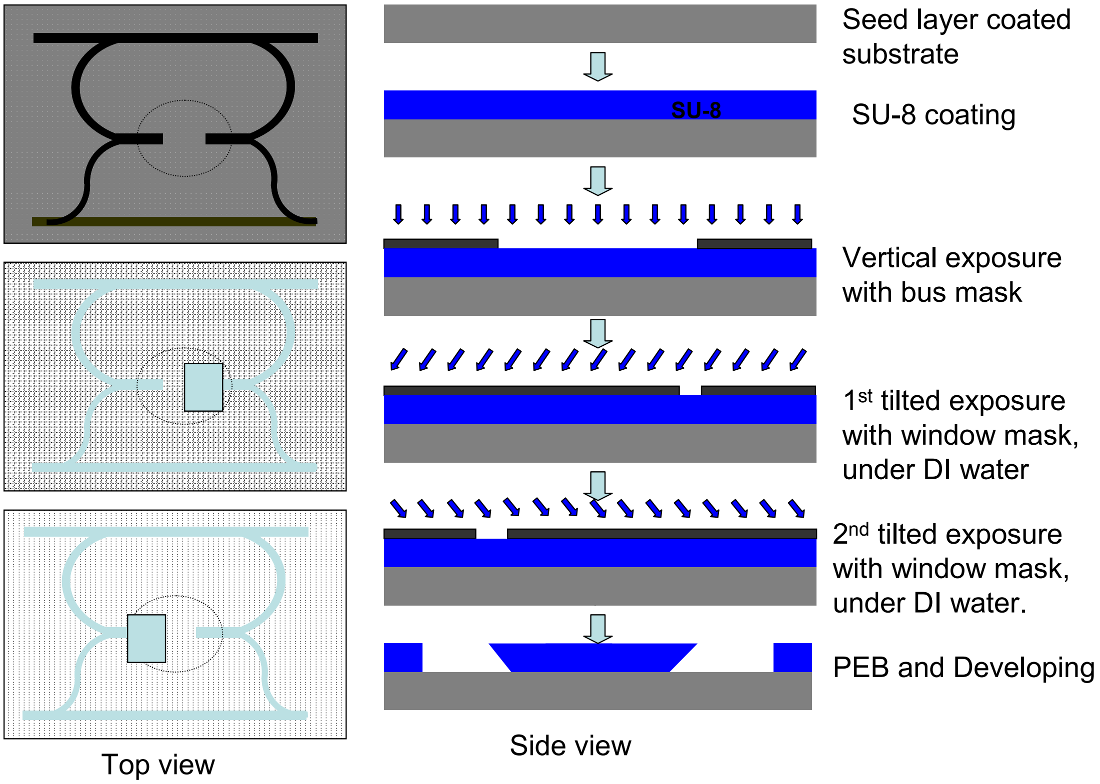

Figure 5.5: Schematic view of the optical bus pre-mold with 45° tilted surfaces preparation using SU-8 layer

The schematic process to prepare the optical bus pre-mold is shown in Figure 5.5. A layer of 50um thick SU-8(from MicroChem) was first spin-coated onto a Ti/Au seed layer coated Si substrate. Three exposures were carried out in order to achieve the waveguide pattern as well as the opposite-placed 45º surfaces. The first exposure was carried out through vertical exposure to create the bus structure using the optical bus mask. The second and third exposures were carried out tilted under DI-Water to achieve 45º surfaces at the input and output node ends of the bus structure. The exposure setup under DI-water and the titled angle was calculated else where [6]. After the three exposures, post-exposure bake and developing were carried out to achieve a SU-8 based optical bus waveguide pre-mold.

The detailed recipe for SU-8 premold preparation before Ni electroplating is listed below:

1. Seed layer deposition 10nm/100nm of Cr/Au on pre-cleaned and dried Si substrate by e-beam evaporation.
2. Omnicoat coating at 3000rpm for 30sec, baking at 200°C for 2min, as sacrificial layer.
3. SU-8 coating at 700rpm for 30sec then ramping to1450rpm for 60sec.
4. Prebake of SU-8 at 65°C for 3min then ramping to 95°C for 6min, then cooling down to room temperature.
5. Vertical exposure using the bus waveguide photomask for 180sec with UV34 filter inserted.
6. Baking at 50°C for 10sec, bus waveguide pattern will appear.
7. Tilted exposure twice under DI-water using the small window photomask, which covers the input or output nodes region, for 600sec each time using UV filter.
8. Post exposure bake at 65°C for 3min, then ramping to 95°C for 6min, slowly cooling

down to room temperature.

9. Developing for 6min in SU-8 developer with agitation and rinse by DI-water.
10. O_2 plasma etching of SU-8 residue inside the waveguide trenches for 10min, with gas flow of 20sccm, 80W forward power, and 10mtorr pressure.
11. AZ-5209 coating in the area where Ni is not intended to be plated.

The developed SU-8 based bus waveguide pre-mold was observed under scanning electron spectroscopy (SEM) as shown in Figure 5.6. Figures 5.6(a) and (b) show one Y-branch splitter and one bus branch splitter, respectively. In order to check the pattern transfer, we measured the branch width under SEM. Figure 5.6(c) and (d) give the SEM images of Y-splitter with a 1:2 power ratio and a 1:1 power ratio. The branch widths measured are consistent with the designed values. Figure 5.6(e) and (f) show the bus-branch splitter with a 1:2 and a 1:1 power ratio, with a consistent value of branch widths as designed. Figure 5.6(g) is the coupler or combiner to the bus waveguide, which has a width of 25um. The actual slant angle of the 45º surface was measured, as shown in Figure 5.6(h), which is 45.5º, having a 0.5º deviation from the designed angle.

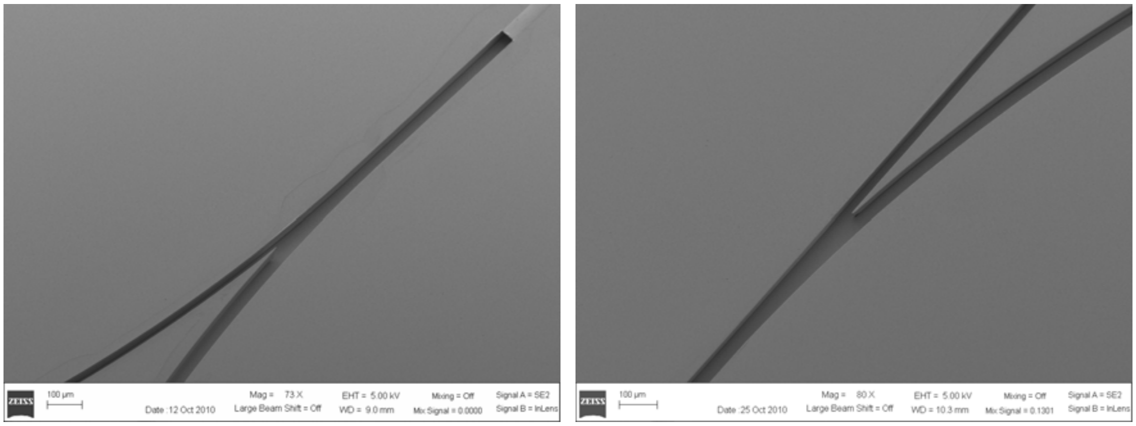

(a) (b)

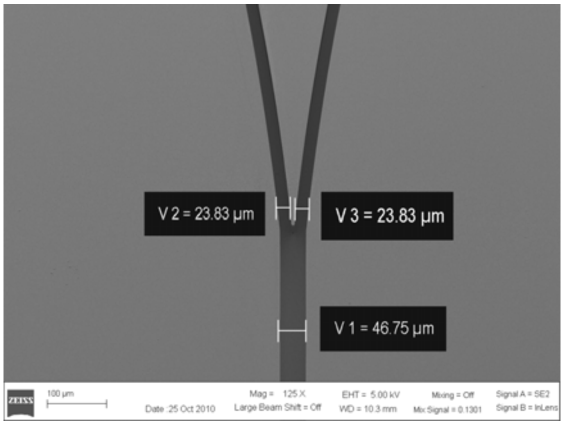
V 2 = 23.83 µm
V 3 = 23.83 µm
V 1 = 46.75 µm
100 µm
Mag = 125 X
EHT = 5.00 kV
Date :25 Oct 2010

(c)

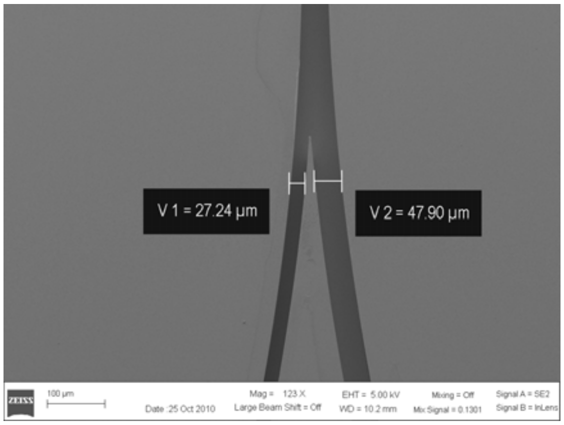
V 1 = 27.24 µm
V 2 = 47.90 µm
100 µm
Mag = 123 X
EHT = 5.00 kV
Date :25 Oct 2010

(d)

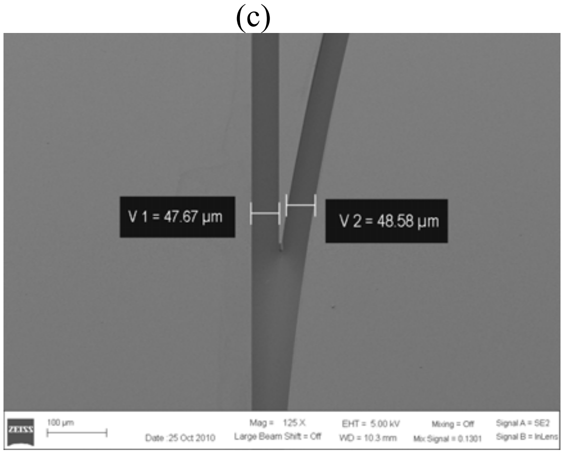
V 1 = 47.67 µm
V 2 = 48.58 µm
100 µm
Mag = 125 X
EHT = 5.00 kV
Date :25 Oct 2010

(e)

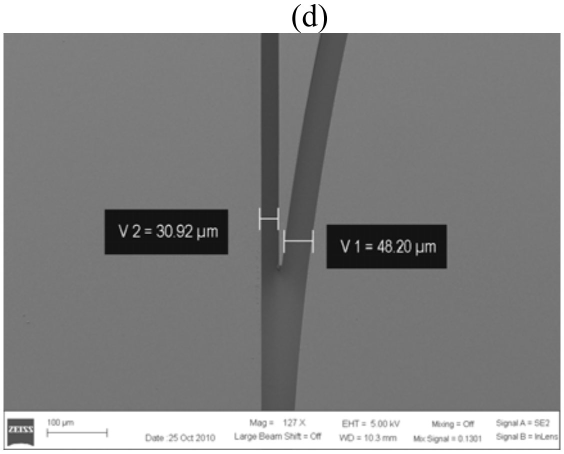
V 2 = 30.92 µm
V 1 = 48.20 µm
100 µm
Mag = 127 X
EHT = 5.00 kV
Date :25 Oct 2010

(f)

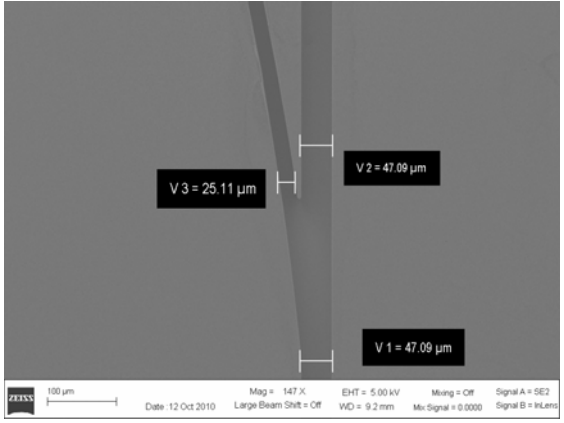
V 2 = 47.09 µm
V 3 = 25.11 µm
V 1 = 47.09 µm
100 µm
Mag = 147 X
EHT = 5.00 kV
Date :12 Oct 2010

(g)

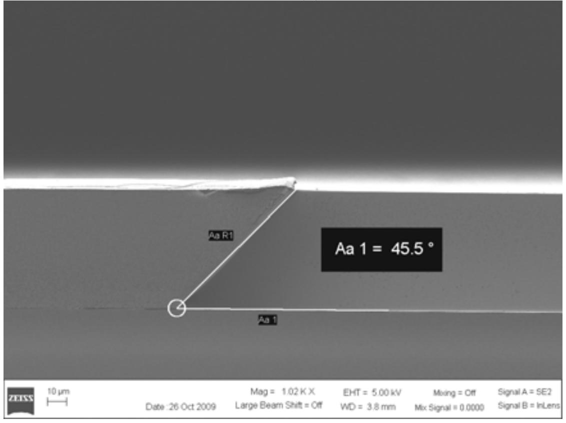
Aa R1
Aa 1 = 45.5 °
Aa 1
10 µm
Mag = 1.02 K X
EHT = 5.00 kV
Date :26 Oct 2009

(h)

Figure 5.6: Top view SEM images of SU-8 pre-mold of (a) input node with Y-branch coupler, (b) waveguide bus and branches coupler, (c)1:1 power ratio Y-splitter, (d) 1:2 power ratio Y-splitter, (e)1:1 power ratio bus-branch splitter, (f) 1:2 power ratio bus-branch splitter, (g)incoming coupler (h) slant angle measurement

5.4 ELECTROPLATING FABRICATION OF NI BUS WAVEGUIDE HARD MOLD

After successfully achieving the SU-8 based optical bus pre-mold, Ni metal was electroplated into the SU-8 defined bus structure trenches. Figure 5.7 shows the whole electroplating process. Ni metal was grown on the seed layer where SU-8 was not covered. The detailed plating parameters were described else-where [6]. Normal plating current density is around 10mA/cm^2. To obtain a 50um thickness of plated metal, total plating time is around 6-7hours. Small current density (<2mA/cm^2) was used at the beginning and the end of electroplating to achieve stronger adhesion and a better polished finish surface. After successfully plating Ni metal, the SU-8 pre-mold layer was removed by remover PG. SU-8 residue was removed by O_2 plasma ashing.

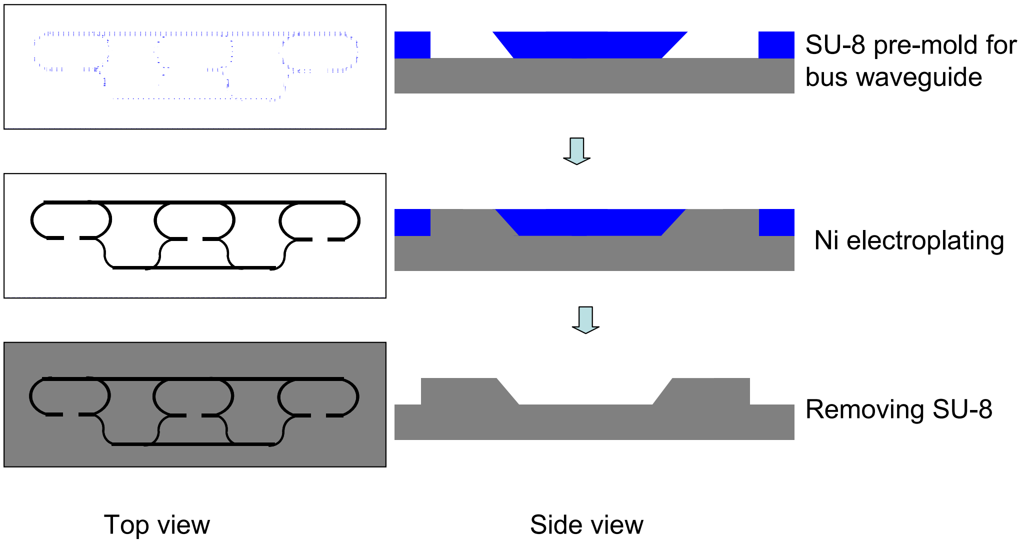

Figure 5.7: Schematic process of Ni hard mold electroplating. Top view and side view are shown on left hand side and right hand side, respectively

The fabricated Ni hard mold was studied under SEM, shown in Figure 5.8. Figure 5.8(a), (b) and (c) show the three groups of input and output nodes with two opposite 45º surfaces on the ends after removing the photopolymer SU-8. Figure 5.8(d) and (e) show a larger magnification of the 45º surface and Y-branch coupler, respectively. Almost all SU-8 residue inside the Y-branch coupler slot was removed. The 45º surface actual slant angle was measured to be 45.2º under SEM, which is shown in Figure 5.8(f). The heights of the metal mold at different locations were scanned by a contact profilometer Dektak150 as shown in Figure 5.9. The height ranges from 48µm to 51µm, which are consistent with the SEM measurement in Figure 5.8(f). It is also consistent well with our design.

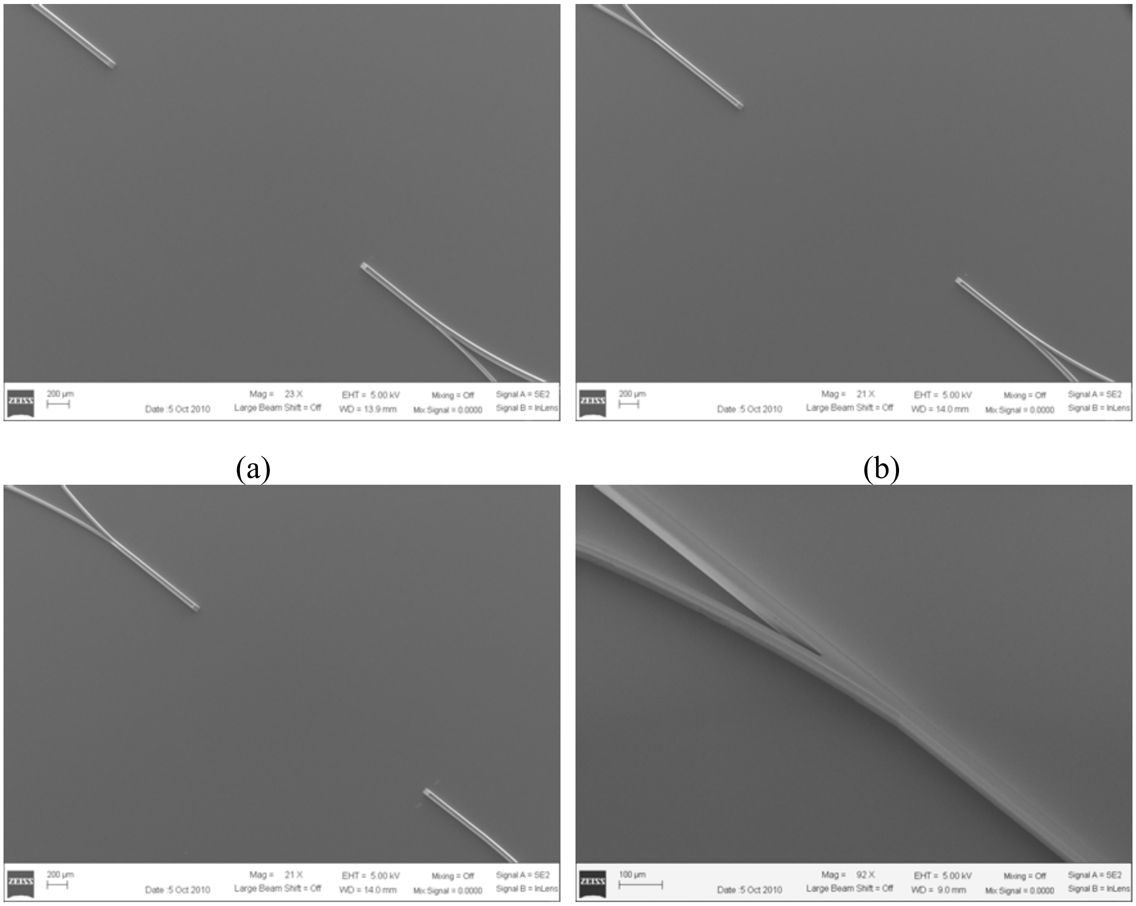

(a)

(b)

(c) (d)

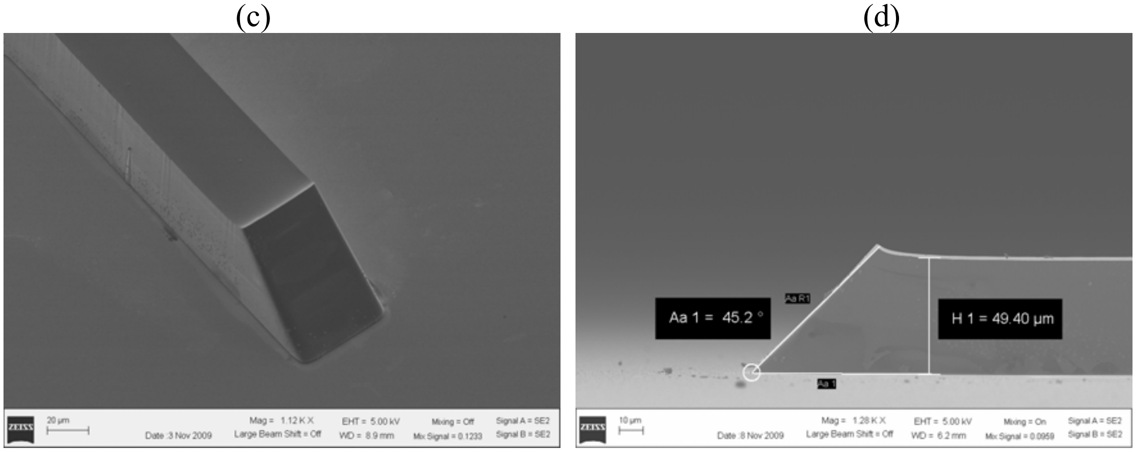

(e) (f)

Figure 5.8: (a) (b) and (c) SEM images of the input and output nodes of the Ni metal bus mold. (d) Closer view of the bus-branch coupler, (e) the 45º surface (f) Measurement of Ni mold slant angles

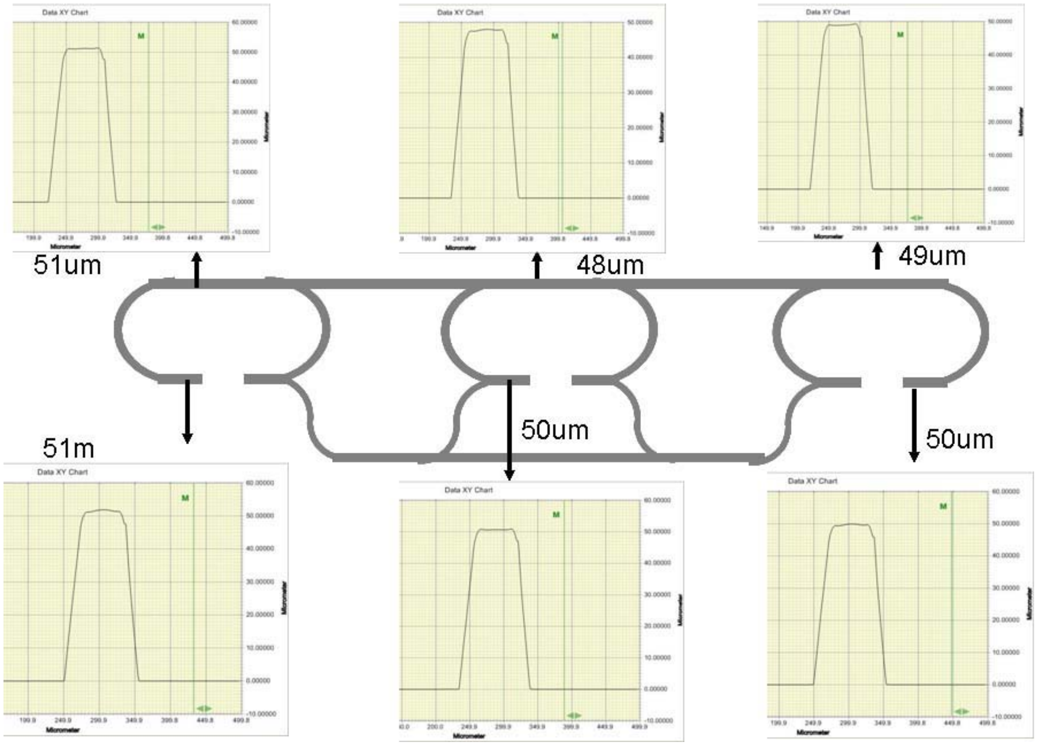

Figure 5.9: Height measurements of Ni bus mold at different locations

In order to verify the repeatability of our tilted exposure and electroplating method, we carried out a series of SU-8 pre-mold fabrication and Ni electroplating experiments. 45º surface slant angles of 10 samples for SU-8 pre-mold and Ni metal mold were measured, as listed in Figure 5.10. For SU-8 pre-mold, the average value of the 45º surface slant angles was 45.3º with a standard deviation of 0.15º. For Ni metal mold, the average value of 45º surface slant angles was 44.8º with a standard deviation of 0.27º. Thus, the measurement results are very consistent. These statistics also prove this procedure of this immersion exposure followed by Ni electroplating is highly repeatable and reliable.

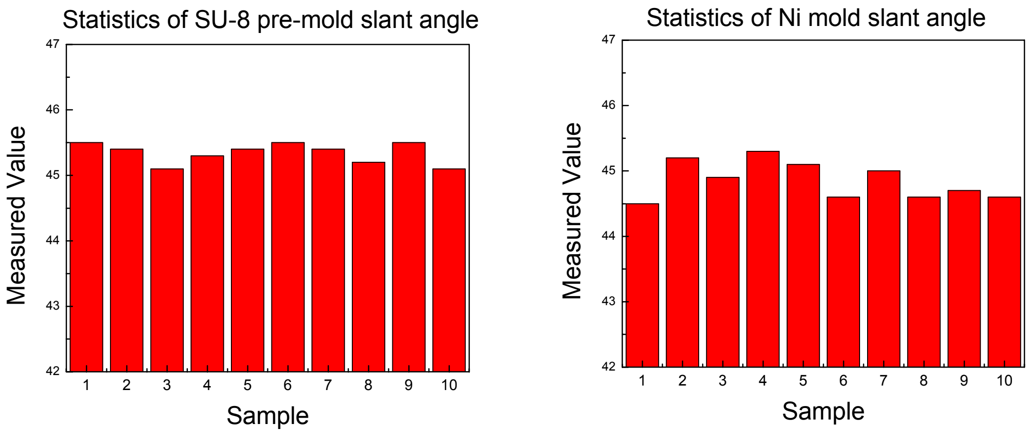

(a) (b)

Figure 5.10: (a) Statistics of SU-8 pre-mold slant angle, (b) Statistics of Ni bus mold slant angle

5.5 IMPRINT FABRICATION OF POLYMERIC OPTICAL BUS WAVEGUIDE

A polymeric optical bus waveguide was successfully fabricated using the electroplated Ni metal bus waveguide mold through a UV emboss method. UV curable polymers WIR30 series (from ChemOptics), WIR30-450 (n=1.45@850nm), WIR30-470 (n=1.47@850nm) were used for the waveguide cladding and core, respectively [7].

200um thick TEONEX thin film (from Dupont Teijin Films Inc.) was used as the TOPAS substrate. The imprint process to prepare the bus waveguide device is shown in Figure 5.11. Firstly, a thin bottom cladding layer of WIR-30-450 was coated on the TOPAS film followed by UV curing for 8min. A layer of 1.0um thick AZ5209 photoresist was spin-coated on the Ni bus hard mold as the release layer. Then a drop of WIR30-450 is applied on the patterned Ni mold and excess WIR30-450 is scraped off. The TOPAS film was then put on the Ni metal mold with WIR-30-450 in between. A PDMS pad was put on the top of TOPAS film, followed by UV cure for 12min to solidify the polymer. After UV curing, the device was released from the hard mold in acetone. In this process, bus waveguide trenches were achieved. After being detached from the Ni mold, 200nm of Au mirrors were deposited at the 45º surface region.

Before core filling, the imprinted optical bus waveguides were studied under scanning electron microscopy (SEM). The results are shown Figure 5.11. Y-branch couplers with power splitting ratios of 1:1 and 1:2 are shown in Figure 5.11(a) and (b), respectively. This shows 45º micro-mirrors on the top region, which couples the light from the surface normal to horizontal. Figure 5.11(c) is a closer view of the 45º micro-mirror section, where the waveguide width is measured around 50um. Figure 5.11 (d) is the bus-branch splitter or combiner.

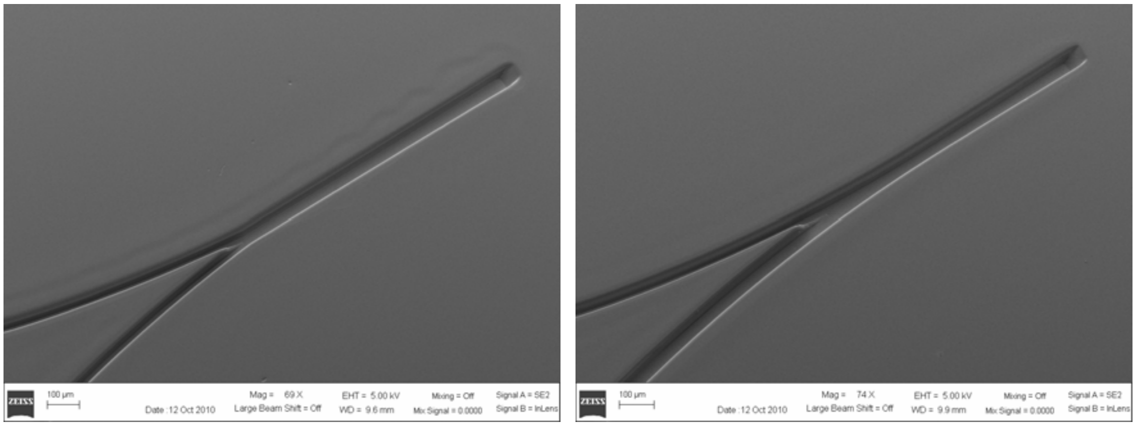

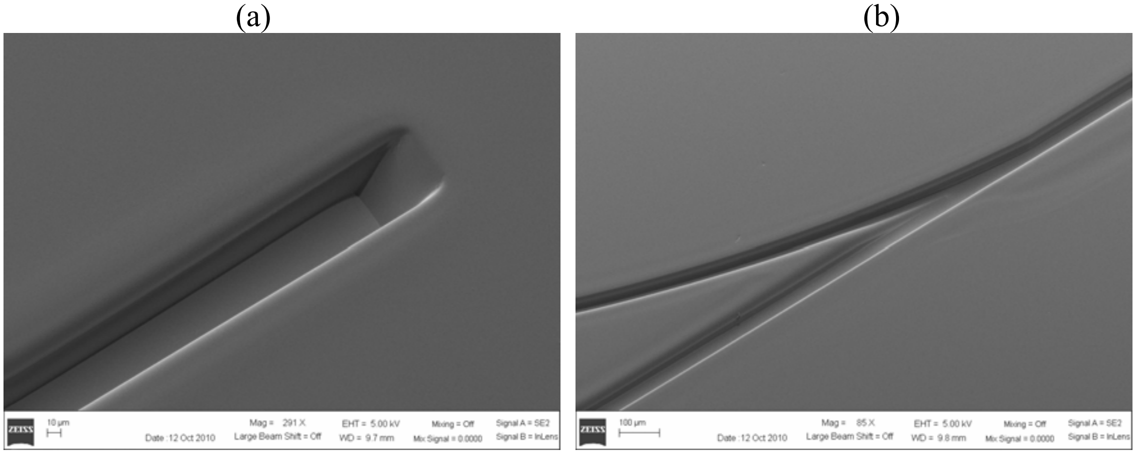

(a) (b)

(c) (d)

Figure 5.11: SEM images of the optical bus waveguide after UV imprint. (a) 1:1 power ratio Y-branch splitter, (b) 1:2 power ratio Y-branch splitter, (c) Closer view of 45 surface, (d) bus branch splitter and combiner

After 200nm of Au mirror was deposited on the 45º surfaces, we applied the core filling process. The schematic process of Au mirror coating and core filling is shown in Figure 5.12. A drop of WIR30-470(n=1.47 at 850nm) was applied on the bus waveguide trench region, and excess WIR30-470 was scraped off using a PDMS pad, followed by a UV cure for 12min to crosslink the core polymer material. After the core filling process, a top cladding was spin-coated and UV cured for 12min.

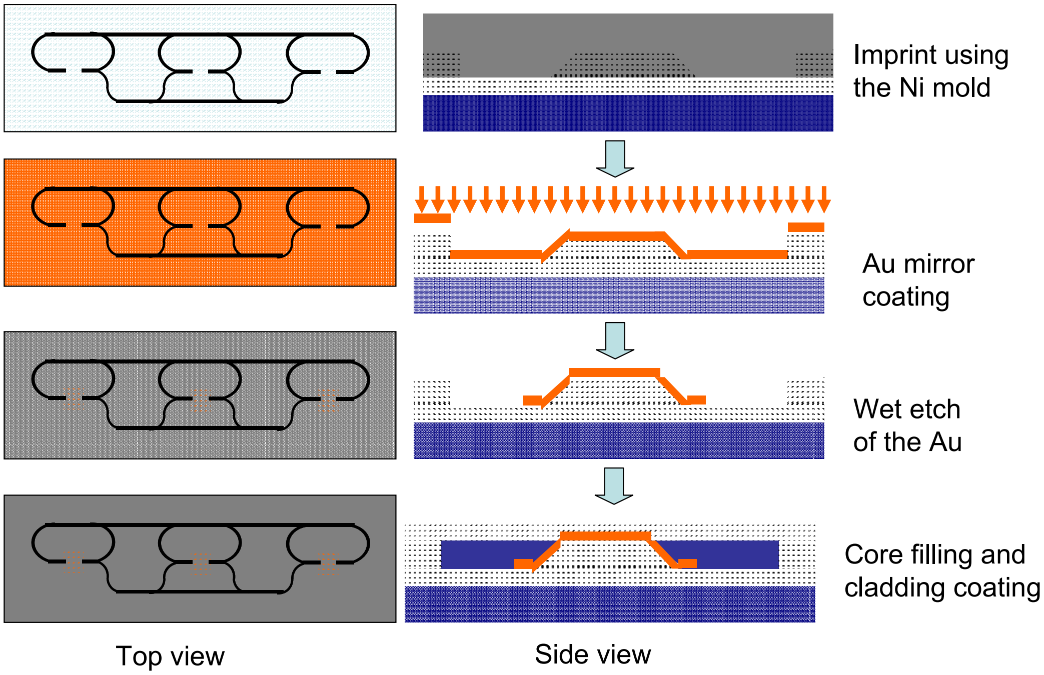

Figure 5.12: UV imprint process to fabricate the polymeric optical bus waveguide devices using a Ni bus hard mold

5.6 OPTICAL TEST ON THE POLYMERIC BUS WAVEGUIDE

A 635nm laser source was used to observe the output of the optical bus waveguide. The experiment setup is shown in Figure 5.13(a). A single mode fiber was fixed above the 45º micro-mirror region of the input node. A photodetector working at 850nm was put on the top of the output nodes. Figure 5.13(b) shows the optical test image with 1 input and 2 outputs. The third output is not shown clearly because it is very close to the input node. Optical test based on the 850nm wavelength laser source was also carried out using an 850nm laser diode with a 9/125um pigtailed SMF, which was surface normally coupled into the waveguide through the 45º micro-mirror. Figure 5.13(c) gives the image of the device after mirror coating, core filling, and cladding coating. A, B and C are denoted as the input and output node positions. The output light intensity was measured by a photodetector operating at 850nm, which was fixed just above the output nodes of the bus waveguide.

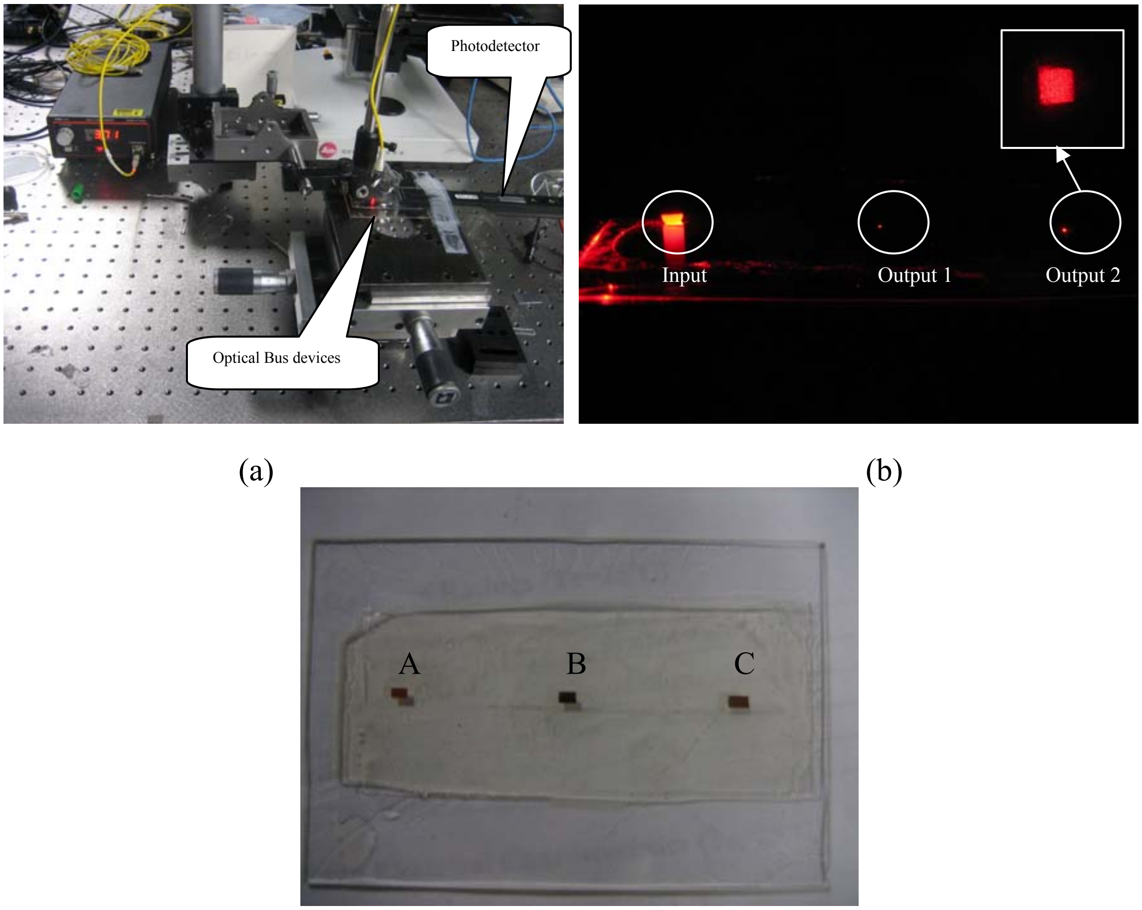

(a) (b)

(c)

Figure 5.13: (a) Optical test setup on the bus waveguide, (b) Output pattern of the device, inset is the pattern through microscope, (c) the image of the bus waveguide device

The input power we used at 850nm is 1.7mW. The nodes A, B, and C all can be used as the input nodes. For instance, we measured the output powers at B and C when A was the input node, measured the output power at A and C when B was the input node, and measured the output power at A and B when C was the input node. Table 5.1 listed the measured results. The minimum loss we achieved is about 15dB. Currently work continues on optimizing the device fabrication to reduce the loss and improve the device performance. There are several aspects that can be considered. One is the embedded mirror qualities. Better control on the tilted exposure could improve the surface quality. Another promising method is using FIB to polish the mold 45 surfaces, which is high cost but could improve the quality significantly. The second aspect is the SU-8 residue and the AZ 5209 release layer after spin-coating inside the Y-splitter narrow gap region, which made the Y-splitter not as sharp as designed. The light may escape from the narrow region of the Y-splitters.

Input **Output**	A		B		C	
A			7.0 uW	23.8dB	8.2 uW	23.2dB
B	10.0 uW	22.3dB			2.2 uW	28.8dB
C	43.0 uW	15.8dB	23.0 uW	18.6dB		

Table 5.3: Input and output power at 850nm

5.8 CONCLUSION

In summary, we have successfully fabricated polymeric optical bus waveguides with 3 input and 3 output nodes embedded with two-opposite 45º micro-mirrors using a Ni metal bus waveguide mold by UV imprint technique. The Ni metal bus waveguide mold was prepared through electroplating metal Ni into a SU-8 defined bus pre-mold which formed opposite 45º surfaces at the input and output node ends by tilted exposure under DI-Water. This work is supported by the National Science Foundation. Helpful discussion on Ni electroplating with Dr. Domesh is gratefully acknowledged.

5.9 REFERENCES

[1]. D. Huang, T. Sze, A. Landin, R. Lytel, and H. L. Davidson, “Optical interconnects: out of the box forever?” IEEE Journal of Selected Topics in Quantum Electronics 9, 614-624 (2003).

[2]. X. Han, G. Kim, G. J. Lipovski, and R. T. Chen, “An optical centralized shared-bus architecture demonstrator for microprocessor-to-memory interconnects,” IEEE J. Sel. Topics Quantum Electron. 9, 512–512 (2003).

[3]. H. Bi, X. Han, X. Chen, W. Jiang, J. Choi, and R. T. Chen, “15Gbps Bit-Interleaved Optical Backplane Bus using Volume Photo-polymer Holograms,” IEEE Photonics Technology Letters 18, 2165-2167 (2006).

[4]. R. T. Chen, L. Lin, C. Choi, Y. Liu, B. Bihari, L. Wu, S. Tang, R. Wickman, B. Picor, M. K. Hibbs-brenner, J. Bristow, and Y. S. Liu, “Fully Embedded Board-Level Guided Wave Optoelectronic Interconnects,” Proc. Of the IEEE 8, 780-794 (2000).

[5]. R. T. Chen, “VME Optical Backplane Bus for High Performance Computer,” Optoelectronics-Devices and Technologies 9, 81-94 (1994).

[6]. X. Y. Dou, A. X. Wang, H. Y. Huang, X. H. Lin, D. Ding, D. Z. Pan and R. T. Chen, “Polymeric waveguides with embedded micro-mirrors formed by Metallic Hard Mold,” Optics Express 18, 378–385 (2010).

[7]. A. X. Wang, W. Jiang, L. Wang and R. T. Chen, “Fully Embedded Board Level Optical Interconnects-From Waveguide Fabrication to Device Integration,” IEEE J. Lightwave Technol. 26, 243-250 (2008).

Chapter 6 *Summary*

This doctoral dissertation described polymer based nano- and micro-photonic devices for three-dimensional optical interconnects. The photonic devices are focusing on two areas, (1) polymer based two-dimensional (2D) and three-dimensional (3D) photonic crystal fabrication and simulation for laser beam steering applications, (2) polymer based high speed optical waveguide array and shared bus waveguides with embedded 45° micro-mirrors for board level optical interconnects.

A three-dimensional (3D) face-centered cubic (FCC) type polymer based photonic crystal using SU-8 as the photo-sensitive material was successfully fabricated using a polygonal prism based holographic fabrication method. We are able to achieve different kinds of triclinic or orthorhombic photonic crystals on demand by changing the top-cut prism structure, the polarization of the laser beam, and the exposure and development conditions. Scanning electron microscopy (SEM) and diffraction results proved the good uniformity of the fabricated structures. 3D photonic crystal in V-groove structures was also successfully fabricated using this holographic interference method. The theoretical study of polymer based photonic crystals was carried out for laser beam steering which is based on the superprism effect. Horizontally stacked two dimensional (2D) photonic crystal was fabricated by a double exposure holographic interference method. K-vector superprism effect, the principle for beam steering, was separately studied in detail through an EFC (Equifrequency Contour) analysis. The experiment results showed a beam steering angle of 10 degrees for a 30nm wavelength variation.

Polymer based optical waveguide array with embedded 45° micro-mirrors for board level optical interconnects were prepared using a Ni metal hard mold by UV imprint. A nickel based metal mold with 45º tilted surfaces on both ends of the channel waveguide was prepared through an electroplating process. To obtain a precise 45º tilted angle, a 50µm thick SU-8 2025 layer was UV exposed under de-ionized water. The 45º slant angle standard deviations of the SU-8 pre-mold and the Ni metal hard mold were 0.15º and 0.27º, respectively. The polymeric waveguide array made of WIR series polymers shows total insertion losses around 4dB, a propagation loss around 0.18dB/cm, and a 75% coupling efficiency.

We also carried out high speed optical tests (10Gb/s) on polymeric optical waveguide arrays with embedded 45º micro-mirrors on a flexible substrate for out-of-plane optical interconnects. The waveguide array was bent with curvatures ranging from 61mm to 5mm. As the bending radius decreases, the average insertion loss increases from 3.4dB to 7.7dB for single-mode fiber (SMF) coupling and from 5.5dB to 7.9dB for multi-mode fiber (MMF) coupling, respectively. Eye-diagrams under such bending conditions show that the Q factor decreases from 8.0 to 6.1, and the calculated bit error rate (BER) increases from 10^{-16} to 10^{-10} at 10Gbps.

A polymer based 3-to-3 shared optical bus waveguide with opposite 45º micro-mirrors was designed using Rsoft and fabricated using a metallic hard mold method. The Ni metal hard mold was successfully prepared using a Ni electroplating method. The optical bus waveguide pre-mold with 45º surfaces before electroplating was prepared using photopolymer SU-8 2025 through tilted exposure process under de-ionized water. Metal nickel was electroplated into SU-8 defined bus waveguide trenches. This metallic hard mold provides a convenient way to fabricate the polymeric optical bus waveguide devices through an imprint technique.

Appendix

Publications

1. **Xinyuan Dou**, Xiaolong Wang, Xiaohui Lin, Duo Ding, David Z. Pan and Ray T. Chen, "Highly Flexible Polymeric Optical Waveguide for Out-of-Plane Optical Interconnects," Optics Express,18, 16227-16233, 2010.
2. **Xinyuan Dou**, Xiaolong Wang, Haiyu Huang, Xiaohui Lin, Duo Ding, David Z. Pan and Ray T. Chen, "Polymeric waveguides with embedded micro-mirrors formed by Metallic Hard Mold," Optics Express 18, 378-385, 2010.
3. **Xinyuan Dou**, Xiaonan Chen, Yihong Chen, Xiaolong. Wang, Wei Jiang and Ray T. Chen, "Ultra-compact Laser beam Steering device using holographically formed two dimensional photonic crystals," J. Nanosci. Nanotechnol. 10, 1650-1655, 2010.
4. **Xinyuan Dou**, Xiaolong Wang, Haiyu Huang, Xiaohui Lin and Ray T. Chen, "Optical bus waveguide metallic hard mold fabrication with opposite 45° micro-mirrors," SPIE Photonic West 2010, 25-29 Jan. 2010, San Jose, CA
5. **Xinyuan Dou**, Xiaolong Wang, Haiyu Huang, Xiaohui Lin and Ray T. Chen, "Fabrication of metallic hard mold for polymeric waveguides with embedded micro-mirrors," IEEE LEOS Winter Topical 2010, pp 101-102, 11-13 Jan. 2010, Majorca, Spain
6. **Xinyuan Dou**, Xiaonan Chen, Yihong Chen, Xiaolong. Wang, Wei Jiang and Ray T. Chen, "Packaging consideration of two dimensional polymer-based photonic crystals for laser beam steering," SPIE Photonic West 2009, 24-29 Jan. 2009, San

Jose, CA

7. **Xinyuan Dou**, Xiaonan Chen, Yihong Chen, Xiaolong. Wang, Wei Jiang and Ray T. Chen, "Vertically stacked square lattice photonic crystals for Large Angle Optical Beam Steering," IEEE LEOS Winter Topical 2009, 12-14 Jan. 2009, Innsbruck, Austria.

8. **Xinyuan Dou**, Zhenping Zhou, Pingheng Tan, Jianjun Zhou, Li Song, Lifeng Liu, et al, Growth of aligned single-walled carbon nanotubes under ac electric fields through floating catalyst chemical vapor deposition; Chinese Physics,14(10), 2068-2076, 2005.

9. **Xinyuan Dou**, Zhenping Zhou, Pingheng Tan, Li Song, S.S. Xie, et al, Surface-enhanced resonant Raman scattering of single-walled carbon nanotubes on the Ag-coated anodic aluminum oxide; Physica E, 27(4), 469-473, 2005.

10. **Xinyuan Dou**, Zhenping Zhou, Li Song, Lifeng Liu, Xiaowei Zhao, Shudong Luo, Xiaoqin Yan, Dongfang Liu, Jianxiong Wang, Yan Gao, Zengxing Zhang, Huajun Yuan, Weiya Zhou, Sishen Xie, Direct ring formation on carbon nanotubes through floating catalyst chemical vapor deposition; The 1st China-U.S. Symposium on Nanoscale Science and Technology. 217, May17-19, 2004.

11. Zhenping Zhou, **Xinyuan Dou**, Lijie Ci, Li Song, Dongfang Liu, Yan Gao, Jianxiong Wang, Lifeng Liu, Weiya Zhou, Sishen Xie, Dongyun Wan, Temperature dependence of the Raman spectra of individual carbon nanotubes, Journal of Physical Chemistry B, 110 (3): 1206-1209, 2006.

12. Zhenping Zhou, Dongyun Wan, **Xinyuan Dou**, Li Song, Xiaoqin Yan, Dongfang Liu, Huajun Yuan, Yan Gao, Jianxiong Wang, Lifeng Liu, Weiya Zhou, Sishen Xie, Surface-enhanced Raman scattering from the individual metallic single-

walled carbon nanotubes, Physica-E, 28, 360-364, 2005.

13. Zhenping Zhou, Dongyun Wan, **Xinyuan Dou**, Li Song, Weiya Zhou, Sishen Xie, Postgrowth alignment of SWNTs by an electric field, Carbon, 44(1), 170-173, 2006.

14. Zhenping Zhou, Dongyun Wan, Ying Bai, **Xinyuan Dou**, Li Song, Weiya Zhou, Yujun Mo, Sishen Xie, Ring formation from the direct floating catalytic chemical vapor deposition, Physica-E, 33(1), 24-27, 2006.

15. Sishen Xie, Li Song, Lijie Ci, Zhenping Zhou, **Xinyuan Dou**, Weiya Zhou, Gang Wang, Lianfeng Sun, Controllable preparation and properties of single-/double-walled carbon nanotubes, Science and Technology of Advanced Materials, 6(7), 25-735, 2005.

16. Li Song, Jie Meng, Jun Zhong, Lifeng Liu, **Xinyuan Dou**, Dongfang Liu, Xiaowei Zhao, Shudong Luo, Zengxing Zhang, Yanjuan Xiang, HY Xu, Weiya Zhou, ZY Wu, Sishen Xie, Human fibrinogen adsorption onto single-walled carbon nanotube films , Colloids and Surfaces B-Biointerfaces, 49(1), 66-70, 2006.

17. Li Song, Lijie Ci, Li Lv, Zhenping Zhou, Xiaoqin Yan, Dongfang Liu, Huajun Yuan, Yan Gao, Jianxiong Wang, Lifeng Liu, Xiaowei Zhao, Zengxing Zhang, **Xinyuan Dou**, Weiya Zhou, Gang Wang, Chaoying Wang, Sishen Xie, Direct synthesis of a macroscale single-walled carbon nanotube non-woven material, Advanced Materials, 16(17),1529-1534, 2004.

18. Yan Gao, Peng Jiang, Li Song, Jianxiong Wang, Lifeng Liu, Dongfang Liu, Yanjuan Xiang, Zengxing Zhang, Xiaowei Zhao, **Xinyuan Dou**, Shudong Luo, Weiya Zhou, Sishen Xie, Studies on silver nanodecahedrons synthesized by PVP-

assisted N,N-dimethylformamide (DMF) reduction, Journal of Crystal Growth, 289(1), 376-380, 2006.

19. Yan Gao, Peng Jiang, Li Song, Lifeng Liu, Xiaoqin Yan, ZQ Zhou, Dongfang Liu, Jianxiong Wang, Huajun Yuan, Zengxing Zhang, Xiaowei Zhao, **Xinyuan Dou**, Weiya Zhou, Gang Wang, Sishen Xie, Growth mechanism of silver nanowires synthesized by polyvinylpyrrolidone-assisted polyol reduction, Journal of Physics D-Applied Physics, 38(7), 1061-1067, 2005.

20. Yan Gao, Li Song, Peng Jiang, Lifeng Liu, Xiaoqin Yan, Dongfang Liu, Jianxiong Wang, Huajun Yuan, Zengxing Zhang, Xiaowei Zhao, **Xinyuan Dou**, Weiya Zhou, Gang Wang, Sishen Xie, HY Chen, Jianqi Li, Silver nanowires with five-fold symmetric cross-section, Journal of Crystal Growth, 276, 606-612, 2005.

21. Shudong Luo, Weiya Zhou, Zengxing Zhang, Lifeng Liu, **Xinyuan Dou**, Jianxiong Wang, Xiaowei Zhao, Dongfang Liu, Yan Gao, Li Song, Yanjuan Xiang, Jianjun Zhou, Sishen Xie, Synthesis of long indium nitride nanowires with uniform diameters in large quantities, Small, 1(10), 1004-1009, 2005.

22. Shudong Luo, Weiya Zhou, Zengxing Zhang, **Xinyuan Dou**, Lifeng Liu, Xiaowei Zhao, Dongfang Liu, Li Song, Yanjuan Xiang, Jianjun Zhou, Sishen Xie, Bulk-quantity synthesis of single-crystalline indium nitride nanobelts, Chemical Physical Letters, 411(4-6), 361-365, 2005.

23. Shudong Luo, Weiya Zhou, WX Wang, Zengxing Zhang, Lifeng Liu, **Xinyuan Dou**, Jianxiong Wang, Xiaowei Zhao, Dongfang Liu, Yan Gao, Li Song, Yanjuan Xiang, Jianjun Zhou, Sishen Xie, Template-free synthesis of helical hexagonal microtubes of indium nitride, Applied Physics Letters, 87(6), 063109, 2005.

24. Xiaowei Zhao, Peng Jiang, Sishen Xie, Jiafeng Feng, Yan Gao, Jianxiong Wang,

Dongfang Liu, Li Song, Lifeng Liu, **Xinyuan Dou**, Shudong Luo, Zengxing Zhang, Yanjuan Xiang, Weiya Zhou and Gang Wang, Patterned anodic aluminium oxide fabricated with a Ta mask, Nanotechnology, 17(1), 35-39, 2006.

25. Xiaowei Zhao, Peng Jiang, Sishen Xie, Lifeng Liu, Weiya Zhou, Yan Gao, Li Song, Jianxiong Wang, Dongfang Liu, **Xinyuan Dou**, Shudong Luo, Zengxing Zhang, Yanjuan Xiang, Gang Wang, Anodizing behavior of aluminum foil patterned with SiO2 mask, Journal of the Electrochemical Society, 152(10), B411-B414, 2005.

26. Lifeng Liu, Sishen Xie, Li Song, Yan Gao, Dongfang Liu, **Xinyuan Dou**, Shudong Luo, Jianxiong Wang, Xiaowei Zhao, Zengxing Zhang, Yanjuan Xiang, Weiya Zhou, Chaoying Wang and Gang Wang, Electrochemical fabrication and structure of NixZn1-x alloy nanowires, Nanotechnology, 17(1), 19-24, 2006.

27. Dongfang Liu, Yanjuan Xiang, Zengxing Zhang, Jianxiong Wang, Yan Gao, Li Song, Lifeng Liu, **Xinyuan Dou**, Xiaowei Zhao, Shudong Luo, Chaoying Wang, Weiya Zhou, Gang Wang, Sishen Xie, Growth of ZnO hexagonal nanoprisms, Nanotechnology, 16(11),2665-2669, 2005.

28. Zengxing Zhang, Jianxiong Wang, Huajun Yuan, Yan Gao, Dongfang Liu, Li Song, Yanjuan Xiang, Xiaowei Zhao, Lifeng Liu, Shudong Luo, **Xinyuan Dou**, Shicheng Mou, Weiya Zhou, and Sishen Xie, Low-temperature growth and photoluminescence property of ZnS nanoribbons, Journal of Physical Chemistry B, 109(39), 18352-18355, 2005.

29. Jianxiong Wang, HY Chen, Yan Gao, Dongfang Liu, Li Song, Zengxing Zhang, Xiaowei Zhao, **Xinyuan Dou**, Shudong Luo, Weiya Zhou, Gang Wang, Sishen Xie, Synthesis and characterization of In2O3/SnO2 hetero-junction beaded

nanowires, Journal of Crystal Growth, 284(1-2), 73-79, 2005.

30. Jianxiong Wang, Sishen Xie, Huajun Yuan, Xiaoqin Yan, Dongfang Liu, Yan Gao, Zhenping Zhou, Li Song, Lifeng Liu, Xiaowei Zhao, **Xinyuan Dou**, Weiya Zhou, Gang Wang, Synthesis, structure, and photoluminescence of Zn2SnO4 single-crystal nanobelts and nanorings, Solid State Communications, 131(7), 435-440, 2004.

31. Huajun Yuan, Xiaoqin Yan, Zengxing Zhang, Dongfang Liu, Zhenping Zhou, L Cao, Jianxiong Wang, Yan Gao, Li Song, Lifeng Liu, Xiaowei Zhao, **Xinyuan Dou**, Weiya Zhou, Sishen Xie, Synthesis, optical, and magnetic properties of Zn1-xMnxS nanowires grown by thermal evaporation, Journal of Crystal Growth, 271(3-4), 403-408, 2004.

Bibliography

Chapter 1

[1] E.Yablonovitch, “Inhibited Spontaneous Emission in Solid-State Physics and Electronics”, Phys. Rev. Lett., 58, 2059 (1987).

[2] S. John, “Strong localization of photons in certain disordered dielectric superlattices”, Phys. Rev. Lett. 58, 2486 (1987).

[3] K. M. Ho, C. T. Chan, and C. M. Soukoulis, “Existence of a photonic gap in periodic dielectric structures”, Phys. Rev. Lett. 65, 3152 (1990).

[4] C. T. Chan, K. M. Ho and C. M. Soukoulis, “Photonic band gaps in experimentally realizable periodic dielectric structures”, Europhys. Lett. 16, 563 (1991).

[5] S. G. Johnson, J. D. Joannopoulos, Photonic crystals: road from theory to practice, Kluwer Academic Publishers, (2002).

[6] L. Wang, “Polymer-based Micro- and Nano-imprint Structures for Manipulation of Laser Beam Propagation,” Dissertation, University of Texas at Austin, 2007.

[7] R. B. Wehrspohn, “Applications of silicon-based photonic crystals”, 2nd IEEE International Conference on Group IV Photonics, 39 (2005).

[8] H. Benisty, J. M. Lourtioz, A. Chelnokov, S. Combrie, X. Checoury, “Recent advances toward optical devices in semiconductor-based photonic crystals”, Proceedings of the IEEE, 94, 5, 997 (2006).

[9] H. Kosaka, T. Kawashima, A. Tomita, M. Notomi, T. Tamamura, T. Sato, and S. Kawakami, “Superprism phenomena in photonic crystals:”, Phys. Rev. B 58, 16, R10096 (1998).

[10] J. D. Joannopoulos, R.D. Meade, J.N. Winn, Photonic Crystals, Princeton University Press, (1995).

[11] S. G. Johnson, J. D. Joannopoulos, Photonic crystals: road from theory to practice, Kluwer Academic Publishers, (2002).

[12] H. Masuda, M. Ohya, H. Ahoh, M. Nakano, M, Nakano and T. Tamamura, Jpn, J. Appl. Phys. 38,L1403, (1999).

[13] J. Schilling, F.Muller, S.Matthias, R.B.Wehrspohn, U.Gosele, Appl.Phys.Lett. 78, 1180, (2001).

[14] M. Campbell, D. N. Sharp, M. T. Harrison, R. G. Denning and A. J. Turberfield, Nature (London) 404, 53 (2000).

[15] L. Z. Cai, X. L. Yang and Y. R. Wang. Opt. Lett. 27, 900, (2002).

[16] D. A. B. Miller, H. M. Ozaktas, "Limit to the bit-rate capacity of electrical interconnects from aspect ratio of system architecture," J. Parallel Distri Computing, 41, 42, (1997).

[17] T. N. Theis, "The future of interconnection technology," IBM J. Res.Develop. 44, 3, 379-389, (2000).

[18] M. Gruber, S. Sinzinger, and J. Jahns, "Optoelectronic multichip module based on planar-integrated free-space optics," Proc. SPIE, Optics in Computing2000, 4089, (2000).

[19] Elmar Griese, "Parallel Optical Interconnects for High Performance Printed Circuit Board," Proc. The 6th Int. Conf., 173, (1999).

[20] Yuzo Ishii, Shinji Koike, Yoshimitsu aria, and Yasuhiro Ando, "SMT-Compatible Optical I/O Chip Packaging for Chip-Level Optical Interconnects," Elec. Components and Technology Conf. 2001.

[21] R. T. Chen, L. Lin, C. Choi, Y. Liu, B. Bihari, L. Wu, S. Tang, R. Wickman, B. Picor, M. K. Hibbs-Brenner, J. Bristow, and Y. S. Liu, "Fully Embedded Board-level Guided-Wave Optoelectronic Interconnects", Proceddings of the IEEE, 88, 6, 780

(2000).

[22] M. Gruber, S. Sinzinger, and J. Jahns, “Optoelectronic multichip module based on planar-integrated free-space optics,” Proc. SPIE, Optics in Computing, 4089, (2000).

[23] Alan Wang, “Highly Integrated Polymer Photonic Switching and Interconnects,” Dissertation, University of Texas at Austin, 2007, Dissertation, (2006).

[24] D. Huang, T. Sze, A. Landin, R. Lytel, and H. L. Davidson, “Optical interconnects: out of the box forever?” IEEE Journal of Selected Topics in Quantum Electronics 9, 614-624 (2003).

[25] X. Han, G. Kim, G. J. Lipovski, and R. T. Chen, “An optical centralized shared-bus architecture demonstrator for microprocessor-to-memory interconnects,” IEEE J. Sel. Topics Quantum Electron. 9, 512–512 (2003).

[26] H. Bi, X. Han, X. Chen, W. iang, J. Choi, and R. T. Chen, “15Gbps Bit-Interleaved Optical Backplane Bus using Volume Photo-polymer Holograms,” IEEE Photonics Technology Letters 18, 2165-2167 (2006).

[27] R. T. Chen, L. Lin, C. Choi, Y. Liu, B. Bihari, L. Wu, S. Tang, R. Wickman, B. Picor, M. K. Hibbs-brenner, J. Bristow, and Y. S. Liu, “Fully Embedded Board-Level Guided Wave Optoelectronic Interconnects,” Proc. Of the IEEE 8, 780-794 (2000).

[28] R. T. Chen, “VME Optical Backplane Bus for High Performance Computer,” Optoelectronics-Devices and Technologies 9, 81-94 (1994).

[29] A. X. Wang, W. Jiang, L. Wang and R. T. Chen, “Fully Embedded Board Level Optical Interconnects-From Waveguide Fabrication to Device Integration,” IEEE J. Lightwave Technol. 26, 243-250 (2008).

Chapter 2

[1] E. Yablonovitch, "Inhibited spontaneous emission in solid-state physics and electronics," Phys. Rev. Lett. 58, 2059-2062, (1987).

[2] S. John, "Strong localization of photons in certain disordered dielectric superlattices," Phys. Rev. Lett. 58, 2486-2489 (1987).

[3] H. Kosaka, T. Kawashima, A. Tomita, M. Notomi, T. Tamamura, T. Sato and S. Kawakami, "Superprism phenomena in photonic crystals," Phys. Rev. B 58, R10096 (1998).

[4] H. Kosaka, T. Kawashima, A. Tomita, M. Notomi, T. Tamamura, T. Sato, S. Kawakami, "Superprism phenomena in photonic crystals: toward microscale lightwave circuits," J. Lightwave Technol. Vol. 17, 2032 (1999).

[5] M. S. Li, S. T. Wu and Andy Ying-Guey Fuh, "Superprism phenomenon based on holographic polymer dispersed liquid crystal films", Appl. Phys. Lett. 88, 091109 (2006).

[6] H. Kosaka, T. Kawashima, A. Tomita, M. Notomi, T. Tamamura, T. Sato and S. Kawakami, "Photonic crystals for micro lightwave circuits using wavelength-dependent angular beam steering," Appl. Phys. Lett. 74, 1370, (1999).

[7] S.Y. Lin, V. M. Hietala, Li Wang, and E. D. Jones, "Highly dispersive photonic band-gap prism," Opt. Lett. 21, 1771, (1996).

[8] J. Chen, W. Jiang, X. Chen, L. Wang, S. Zhang, and R. T. Chen, "Holographic three-dimensional polymeric photonic crystals operating in the 1550 nm window," Appl. Phys. Lett. vol. 90, 093102 (2007).

[9] T. Kondo, S. Juodkazis, and H. Misawa, "Reduction of capillary force for high aspect-ratio nanofabrication," Appl. Phys. A 81, 1583–1586 (2005).

[10] S. Noda, T. Baba, "Roadmap on photonic crystals", Springer (2003).

[11] W. Jiang, R. T. Chen, and X. Lu, "Theory of light refraction at the surface of a

photonic crystal," Phys. Rev. B 71, 245115 (2005).

[12] W. Jiang and R. T. Chen, "Symmetry-induced singularities of the dispersion surface curvature and high sensitivities of a photonic crystal," Phys. Rev. B 77, 075104 (2008).

[13] T. Kondo, S. Juodkazis, V. Mizeikis and H. Misawa, "Holographic lithography of periodic two- and three-dimensional microstructures in photoresist SU-8," Optics Express, 14, 7943 (2006).

Chapter 3

[1] R. T. Chen, L. Lin, C. Choi, Y. Liu, B. Bihari, L. Wu, S. Tang, R. Wickman,B. Picor, M. K. Hibbs-Brenner, J. Bristow, and Y. S. Liu, "Fully Embedded Board level Guided-wave Optoelctronic Interconnects," Proc. IEEE, 88, 780-793 (2000).

[2] A. V. Krishnamoorthy, and D. A. B. Miller, "Scaling optoelectronic-VLSI circuits into the 21st century: A technology roadmap," IEEE J. Sel. Top. Quantum Electron. 2(1), 55–76 (2006).

[3] E. Mohanmmed, A. Alduino, T. Thomas, H. Braunisch, D. Lu, J. Heck, A. Liu, I. Young, B. Barnett, G. Vandentop, and R. Mooney, "Optical interconnect system integration for ultra-short-reach applications," J. Intel. Technol. 8(2), 115–127 (2004).

[4] L. Wang, X. Wang, W. Jiang, J. Choi, H. Bi, and R. T. Chen, "45° polymer-based total internal reflection coupling mirrors for fully embedded intraboard guided wave optical interconnects," Appl. Phys. Lett. 87(14), 141110 (2005).

[5] X. Wang, W. Jiang, L. Wang, H. Bi, and R. T. Chen, "Fully Embedded Board-Level Optical Interconnects From Waveguide Fabrication to Device Integration," J. Lightwave Technol. 26(2), 243–250 (2008).

[6] M. Hikita, R. Yoshimura, M. Usui, S. Tomaru, and S. Imamura, “Polymeric optical waveguides for optical interconnections,” Thin Solid Films, 331(1), 303–308 (1998).

[7] S. H. Hwang, W.-J. Lee, J. W. Lim, K. Y. Jung, K. S. Cha, and B. S. Rho, “Chip- and board-level optical interconnections using rigid flexible optical electrical printed circuit boards,” Opt. Express, 16(11), 8077–8083 (2008).

[8] C. Choi, L. Lin, Y. Liu, J. Choi, L. Wang, D. Haas, J. Magera, and R. T. Chen, “Flexible optical waveguide film fabrications and optoelectronic devices integration for fully embedded board-level optical interconnects,” J. Lightw. Technol., 22(9), 2168–2176 (2004).

[9] F. Wang, F. Liu, and A. Adibi, “45 Degree Polymer Micromirror Integration for Board-Level Three-Dimensional Optical Interconnects,” Opt. Express, 17(13), 10514-10521 (2009).

[10] W.J. Lee, S. H. Hwang, J. W. Lim, and B. S. Rho, “Polymeric Waveguide Film With Embedded Mirror for Multilayer Optical Circuits,” IEEE Photon. Technol. Lett. 21(1), 12-14 (2009).

[11] J. Van Erps, N.Hendrickx, C. Debaes, P. Van Daele, H. Thienpont, “Discrete Out-of-Plane Coupling Components for Printed Circuit Board-Level Optical Interconnections” IEEE Photon. Technol. Lett. 19(21), 1753-1755 (2007).

[12] N. Hendrickx,; J. Van Erps, E. Bosman, C. Debaes, H. Thienpont, P. Van Daele, “Embedded Micromirror Inserts for Optical Printed Circuit Boards,” IEEE Photon. Technol. Lett. 20(20), 1727-1729 (2008).

Chapter 4

[1] O. Ishida, and T. Wang, “100 gigabit Ethernet transport,” IEEE Commun. Mag. 48, S4 - S4, (2010).

[2] R. T. Chen, L. Lin, C. Choi, Y. Liu, B. Bihari, L. Wu, S. Tang, R. Wickman, B. Picor, M. K. Hibbs-Brenner, J. Bristow, and Y. S. Liu, “Fully Embedded Board level Guided-wave Optoelctronic Interconnects,” Proc. IEEE, 88, 780-793 (2000).

[3] F. E. Doany, C. L. Schow, C. W. Baks, D. M. Kuchta, P. Pepeljugoski, L. Schares, R. Budd, F. Libsch, R. Dangel, F. Horst, B. J. Offrein, and J. A. Kash, “160 Gb/s Bidirectional Polymer-Waveguide Board-Level Optical Interconnects Using CMOS-Based Transceivers,” Advanced Packaging, IEEE Transactions on, 32(2),345-359 (2009).

[4] X. Y. Dou, X. L Wang, H. Y. Huang, X. H. Lin, D. Ding, D. Z. Pan, and R. T. Chen, “Polymeric waveguides with embedded micro-mirrors formed by Metallic Hard Mold,” Opt. Express 18, 378-385 (2010).

[5] L. Wang, X. Wang, W. Jiang, J. Choi, H. Bi, and R. T. Chen, “45° polymer-based total internal reflection coupling mirrors for fully embedded intraboard guided wave optical interconnects,” Appl. Phys. Lett. 87(14), 141110 (2005).

[6] X. Wang, W. Jiang, L. Wang, H. Bi, and R. T. Chen, “Fully Embedded Board-Level Optical Interconnects From Waveguide Fabrication to Device Integration,” J. Lightwave Technol. 26(2), 243-250 (2008).

[7] M. Hikita, R. Yoshimura, M. Usui, S. Tomaru, and S. Imamura, “Polymeric optical waveguides for optical interconnections,” Thin Solid Films, 331(1), 303-308 (1998).

[8] F. Wang, F. Liu, and A. Adibi, “45 Degree Polymer Micromirror Integration for Board-Level Three-Dimensional Optical Interconnects,” Opt. Express, 17(13), 10514-10521 (2009).

[9] W. J. Lee, S. H. Hwang, J. W. Lim, and B. S. Rho, “Polymeric Waveguide Film

With Embedded Mirror for Multilayer Optical Circuits," IEEE Photon. Technol. Lett. 21(1), 12-14 (2009).

[10] J. Van Erps, N.Hendrickx, C. Debaes, P. Van Daele, and H. Thienpont, "Discrete Out-of-Plane Coupling Components for Printed Circuit Board-Level Optical Interconnections" IEEE Photon. Technol. Lett. 19(21), 1753-1755 (2007).

[11] N. Hendrickx, J. Van Erps, E. Bosman, C. Debaes, H. Thienpont, and P. Van Daele, "Embedded Micromirror Inserts for Optical Printed Circuit Boards," IEEE Photon. Technol. Lett. 20(20), 1727-1729 (2008).

[12] B. S. Rho, W. J. Lee, J. W. Lim, G. W. Kim, C. H. Cho, and S. H. Hwang, "High-reliability flexible optical printed circuit board for opto-electric interconnections," Opt. Eng. 48(1), 015401 (2009).

[13] B. Howley, X. L. Wang, Y. H. Chen, and Ray T. Chen, "Experimental evaluation of curved polymer waveguides with air trenches and offsets," J. Appl. Phys. 100, 023114 (2006).

Chapter 5

[1] D. Huang, T. Sze, A. Landin, R. Lytel, and H. L. Davidson, "Optical interconnects: out of the box forever?" IEEE Journal of Selected Topics in Quantum Electronics 9, 614-624 (2003).

[2] X. Han, G. Kim, G. J. Lipovski, and R. T. Chen, "An optical centralized shared-bus architecture demonstrator for microprocessor-to-memory interconnects," IEEE J. Sel. Topics Quantum Electron. 9, 512–512 (2003).

[3] H. Bi, X. Han, X. Chen, W. Jiang, J. Choi, and R. T. Chen, "15Gbps Bit-Interleaved

Optical Backplane Bus using Volume Photo-polymer Holograms," IEEE Photonics Technology Letters 18, 2165-2167 (2006).

[4] R. T. Chen, L. Lin, C. Choi, Y. Liu, B. Bihari, L. Wu, S. Tang, R. Wickman, B. Picor, M. K. Hibbs-brenner, J. Bristow, and Y. S. Liu, "Fully Embedded Board-Level Guided Wave Optoelectronic Interconnects," Proc. Of the IEEE 8, 780-794 (2000).

[5] R. T. Chen, "VME Optical Backplane Bus for High Performance Computer," Optoelectronics-Devices and Technologies 9, 81-94 (1994).

[6] X. Y. Dou, A. X. Wang, H. Y. Huang, X. H. Lin, D. Ding, D. Z. Pan and R. T. Chen, "Polymeric waveguides with embedded micro-mirrors formed by Metallic Hard Mold," Optics Express 18, 378–385 (2010).

[7] A. X. Wang, W. Jiang, L. Wang and R. T. Chen, "Fully Embedded Board Level Optical Interconnects-From Waveguide Fabrication to Device Integration," IEEE J. Lightwave Technol. 26, 243-250 (2008).

VITA

Xinyuan Dou was born in Shandong Jinan, China, on Apr. 22nd, 1980, as the second son of Chengkang Wang and Jianrong Dou. After completing his study at Shanghe NO.2 High School in 1998, he entered Shandong University majoring in physics. He received the Bachelor's degree of Science from the Department of Physics in July 2002. He attended the graduate school of the Chinese Academy of Sciences (CAS), Beijing, China in September 2002 with the entrance exam waived. He obtained the Master's degree of Science in Condensed Matter Physics from Institute of Physics of the Chinese Academy of Sciences, China in 2005. After one year study at Penn State University, he joined the University of Texas at Austin in August 2006 for his PhD study. His current research topics cover the polymer based photonic crystals, board level optical interconnects and electroplating preparation of waveguide metal molds.

Permanent Address: 3373B Lake Austin Blvd,
Austin, TX, 78703.

This dissertation was typed by the author.